РОССИЙСКИЙ ГОСУДАРСТВЕННЫЙ ПЕДАГОГИЧЕСКИЙ УНИВЕРСИТЕТ им. А. И. ГЕРЦЕНА
HERZEN STATE PEDAGOGICAL UNIVERSITY of RUSSIA

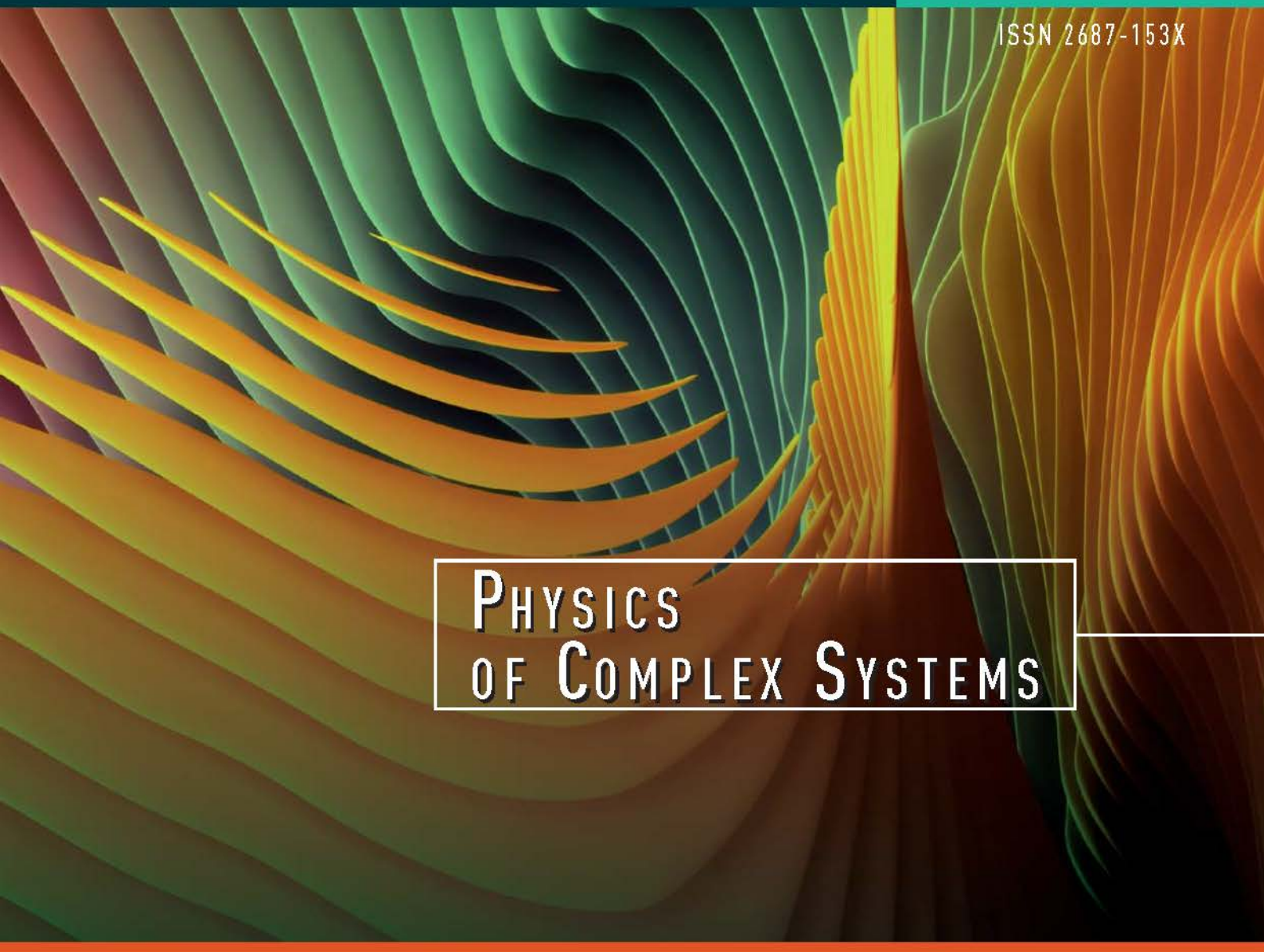

ISSN 2687-153X

Physics of Complex Systems

Т. 5 № 4 2024

Vol. 5 No. 4 2024

Herzen State Pedagogical University of Russia

ISSN 2687-153X (online)
physcomsys.ru
https://www.doi.org/10.33910/2687-153X-2024-5-4
2024. Vol. 5, no. 4

PHYSICS OF COMPLEX SYSTEMS

Mass Media Registration Certificate El No. FS77-77889, issued by Roskomnadzor on 10 February 2020
Peer-reviewed journal
Open Access
Published since 2020
4 issues per year

Editorial Board
Editor-in-chief Alexander V. Kolobov (Saint Petersburg, Russia)
Deputy Editor-in-chief Andrey K. Belyaev (Saint Petersburg, Russia)
Deputy Editor-in-chief Dmitry E. Temnov (Saint Petersburg, Russia)
Executive Secretary Alexey A. Kononov (Saint Petersburg, Russia)
Vachagan T. Avanesyan (Saint Petersburg, Russia)
Alexander P. Baraban (Saint Petersburg, Russia)
Sergey P. Gavrilov (Saint Petersburg, Russia)
Dmitry M. Gitman (São Paulo, Brazil)
Vladimir M. Grabov (Saint Petersburg, Russia)
Andrey A. Grib (Saint Petersburg, Russia)
Elisabeth Dalimier (Paris, France)
Alexander Z. Devdariani (Saint Petersburg, Russia)
Vadim K. Ivanov (Saint Petersburg, Russia)
Rene A. Castro Arata (Saint Petersburg, Russia)
Miloš Krbal (Pardubice, the Czech Republic)
Sergey A. Nemov (Saint Petersburg, Russia)
Oleg Yu. Prikhodko (Almaty, Kazakhstan)
Igor P. Pronin (Saint Petersburg, Russia)
Mikhail Yu. Puchkov (Saint Petersburg, Russia)
Alexey E. Romanov (Saint Petersburg, Russia)
Pavel P. Seregin (Saint Petersburg, Russia)
Koichi Shimakawa (Gifu, Japan)

Advisory Board
Gennady A. Bordovsky (Saint Petersburg, Russia)
Alexander V. Ivanchik (Saint Petersburg, Russia)
Vladimir V. Laptev (Saint Petersburg, Russia)
Alexander S. Sigov (Moscow, Russia)

Publishing house of Herzen State Pedagogical University of Russia
48 Moika Emb., Saint Petersburg 191186, Russia
E-mail: izdat@herzen.spb.ru
Phone: +7 (812) 312-17-41

Data size 13,2 Mbyte
Published at 20.12.2024

The contents of this journal may not be used in any way without a reference to the journal "Physics of Complex Systems" and the author(s) of the material in question.

Editors of the English text *I. A. Nagovitsyna, K. Yu. Rybachuk*
Corrector *M. S. Ogurenkova*
Cover design by *O. V. Rudneva*
Layout by *D. V. Romanova*

Saint Petersburg, 2024
© Herzen State Pedagogical University of Russia, 2024

CONTENTS

Check for updates

Condensed Matter Physics.
Phase equilibria and phase transitions

UDC 538.9

EDN JFGSTK
https://www.doi.org/10.33910/2687-153X-2024-5-4-172-176

Melting and sublimation of graphene and silicene

Yu. D. Fomin ✉[1], E. N. Tsiok [1], V. N. Ryzhov [1]

[1] Vereshchagin Institute of High Pressure Physics, Russian Academy of Sciences,
14 Kaluzhskoe Highway, Troitsk, Moscow 108840, Russia

Authors

Yury D. Fomin, ORCID: 0000-0002-8344-4533, e-mail: fomin314@mail.ru

Elena N. Tsiok, ORCID: 0000-0001-5398-5630, e-mail: ena314@mail.ru

Valentin N. Ryzhov, ORCID: 0000-0002-1331-3984, e-mail: ryzhov@hppi.troitsk.ru

For citation: Fomin, Yu. D., Tsiok, E. N., Ryzhov, V. N. (2024) Melting and sublimation of graphene and silicene. *Physics of Complex Systems*, 5 (4), 172–176. https://www.doi.org/10.33910/2687-153X-2024-5-4-172-176 EDN JFGSTK

Received 9 September 2024; reviewed 26 September 2024; accepted 26 September 2024.

Funding: The study did not receive any external funding.

Copyright: © Yu. D. Fomin, E. N. Tsiok, V. N. Ryzhov (2024) Published by Herzen State Pedagogical University of Russia. Open access under CC BY-NC License 4.0.

Abstract. This study involves molecular dynamics simulations aimed at investigating the crystal structure collapse of graphene, graphite and silicene. It shows that in the case of graphene and graphite, crystal structure collapse is related to the sublimation of the sample. At the same time, when a silicene sample is heated at constant volume, it comes into the liquid–gas two-phase region of the phase diagram. The difference in the crystal structure collapse of graphene and silicene is caused by the differences in the pressure of the liquid–gas–crystal triple point.

Keywords: molecular dynamics simulations, graphene, silicene, sublimation, liquid–gas–crystal triple point

Introduction

It is believed that the ground state of all systems should be some kind of a crystal structure. However, when this crystal is heated, the ordered structure collapses, and the system becomes disordered. Importantly, the collapse of the crystal structure proceeds via either melting or sublimation phase transition depending on the pressure in the system: if the pressure is above the one in the liquid–gas–crystal triple point, the crystal melts. Otherwise, it sublimates. Therefore, depending on the triple point location, different processes can govern the collapse of the crystalline structure.

Nowadays there is a strong interest in two-dimensional materials such as graphene and silicene. These materials are expected to give numerous advantages for different technological applications. Therefore, the issue of their thermal stability is also of great importance.

Melting of graphene was studied in a number of papers. A Monte Carlo study of graphene melting was reported in Ref. (Zakharchenko et al. 2011). It was observed that at very high temperatures (about 4,900 K) carbon atoms start to form linear chains that can decompose from the graphene sheet. The authors made a conclusion that at T_m = 4,900 K graphene melts in a kind of polymer gel.

The same group of authors improved these findings in Ref. (Los et al. 2015), extrapolating them to lower temperatures using classical nucleation theory. As a result, they concluded that the melting temperature of graphene is T_m = 4,500 K.

Another attempt to address this issue was undertaken by Orekhov and Stegailov in Ref. (Orekhov, Stegailov 2015). Based on molecular dynamics simulations with the well-recognized AIREBO model

(Stuart et al. 2000), they concluded that the melting temperature of graphene is T_m = 4,900 K, which is consistent with Ref. (Zakharchenko et al. 2011). They did not employ the extrapolation procedure like the one used in Ref. (Los et al. 2015); therefore, one might expect that T_m = 4,500 K is a more reliable result. Since the melting point of graphene is extremely high, we are not aware of any experimental work on the topic. All available results are based on molecular simulation methods.

The melting temperature of silicene was also evaluated in a number of computational works.

Ref. (Bocchetti et al. 2014) reported on the Monte Carlo simulation of the melting of a silicene sheet. The Tersoff potential (Tersoff 1989) with two sets of parameters was implemented: the original ones (Tersoff 1989) and the ones from Ref. (Agrawal et al. 2005). The melting temperature of silicene was estimated to be 3,600 K in the former case and 1,750 K in the latter.

Non-equilibrium molecular dynamics simulation of the melting of silicene with the Tersoff potential was performed in Ref. (Das, Sarkar 2018). The melting temperature was estimated to be 1,201 K.

Non-equilibrium molecular dynamics simulation of the melting of silicene in the framework of the Stillinger–Weber potential (Stillinger, Weber 1985) was carried out in Refs. (Min et al. 2018) and (On 2020). The melting temperature was reported to be 1,500 K in the former publication and 2,500 K in the latter.

It is seen from the discussion above that the estimation of the melting point of silicene ranges from 1,200 K up to 3,600 K, which is definitely unsatisfactory.

In the present paper, we perform a molecular dynamics simulation of the crystal structure collapse of graphene and silicene, showing that they experience different phase transitions: sublimation in the case of graphene and transition into the two-phase region in the case of silicene.

Systems and methods

We performed molecular dynamics simulations of graphene, graphite and silicene.

In the case of graphene and graphite, the AIREBO potential (Stuart et al. 2000) was utilized. The graphene sample consisted of 6,400 carbon particles in a layer surrounded by vacuum. In the case of graphite, a 4,000-particle sample in a rectangular box was used. Periodic boundary conditions were used. The time step was set to 0.2 fs, and the whole simulation run was 2 ns. The temperature was set to 8,000 K. The pressure was fixed at 1 bar. For the crystal structure that collapsed during the simulation time, a system of linear chains (clusters) was obtained. The particles were considered to belong to the same cluster if the distance between them was less than 1.95 Å.

In the case of silicene, the Stillinger–Weber potential (Stillinger, Weber 1985) was employed. The system consisted of 20,000 silicon atoms surrounded by vacuum. Periodic boundary conditions were used. The time step was set to 1 fs, and the whole run was 10 ps. The system was simulated at constant volume and at several different temperatures. Two characteristics of the system were monitored during the simulation time: the average potential energy per particle and the thickness of the silicene film, which was defined as the difference between the z coordinates of the highest and the lowest particles in the system. When the time dependence of these quantities experienced a jump, the crystal structure collapsed.

Results and discussion

The case of graphene and graphite

Firstly, we performed a molecular dynamics study of the crystal structure collapse of graphene and graphite. As stated above, both systems are simulated at a very high temperature of T = 8,000 K, which is definitely above the melting or sublimation points. The snapshots of the configurations after the structure collapse of graphene and graphite are given in Fig. 1 (a) and (c) respectively. It is seen that the final configurations consist of linear chains of different length (linear clusters). We calculated the distribution of cluster sizes, which is given in Fig. 1 (b). It is seen that the probability distribution of cluster sizes perfectly coincides for both initial structures. Moreover, the probability distributions have a high peak at the chain length of three atoms.

According to the experimental data (Leider et al. 1973), gaseous carbon consists mostly of three atoms' clusters. Comparing it to our results, we conclude that gaseous carbon is obtained after the collapse of the crystal structure. Therefore, sublimation takes place in the case of graphite and graphene.

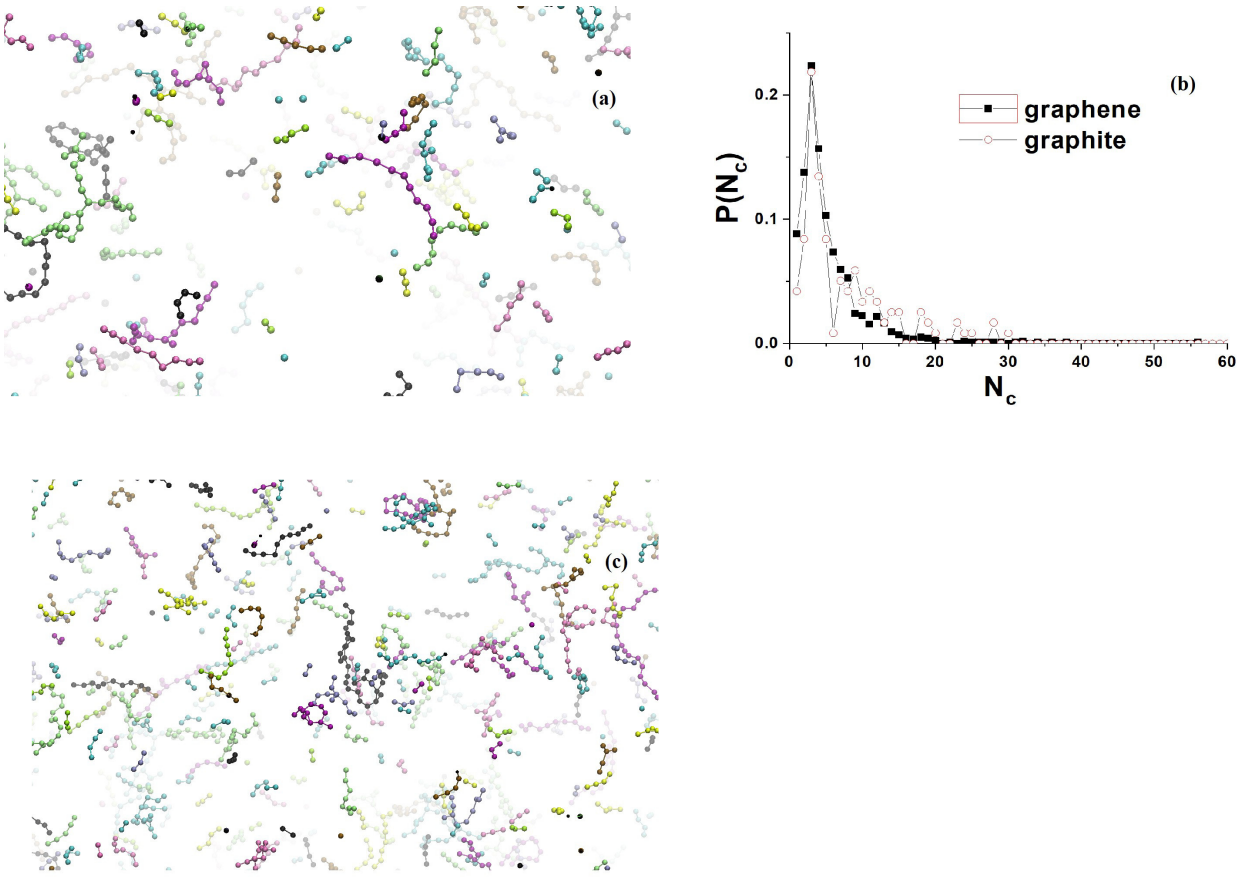

Fig. 1. (a) The snapshot of a system with the initial structure of graphene after the crystal structure collapse. (b) The probability distribution of the size of the clusters of carbon atoms in the systems with the initial structures of graphene and graphite after the crystal structure collapse. (c) The same as (a), but with the initial structure of graphite

The case of silicene

In the case of silicene we simulated the system at different temperatures and monitored its potential energy and the thickness of the sample. Fig. 2 (a) shows time dependence of the potential energy per particle of silicene at different temperatures. At room temperature, the silicene layer has buckled configuration at thickness 5 Å, but at the same time it retains its defect-free honeycomb shape. The potential energy does not change during the whole simulation time.

With temperature rising to 850 K, the potential energy increased slightly, which may be due to the formation of defects because of thermal instability, which leads to a growth in the thickness of the system. The potential energy and thickness of the system do not change during simulation at T = 850 K.

However, as soon as the temperature reaches T = 875 K, after a while there is a sharp drop in potential energy, which means that the structure of the system has changed dramatically. Apparently, the low-energy state of the system is thermodynamically more favorable than the initial defective one at T = 875 K. However, the energy still continues to decrease slightly over time, and the thickness of the system grows continuously, that is, silicene does not reach thermodynamic stability during simulation. The snapshots of the system at T = 850 and 875 K are shown in Fig. 2 (b) and (d) respectively. It is seen that the sample remains crystalline at the former temperature, but is disordered at the latter. At the same time, the system remains condensed at T = 850 K, since it has finite thickness, i. e. its atoms do not occupy the whole available volume.

We are not aware of any evaluation of the location of the gas–liquid–crystal triple point of silicon. However, the pressure of a saturated vapor is available (Babichev et al. 1991). The melting temperature of silicon at ambient pressure is 1,673 K. The pressure of the saturated vapor of silicon at 1,673 K is about 5 bar, which is very close to the ambient one. It means that although we do not know the exact position

 https://www.doi.org/10.33910/2687-153X-2024-5-4-172-176

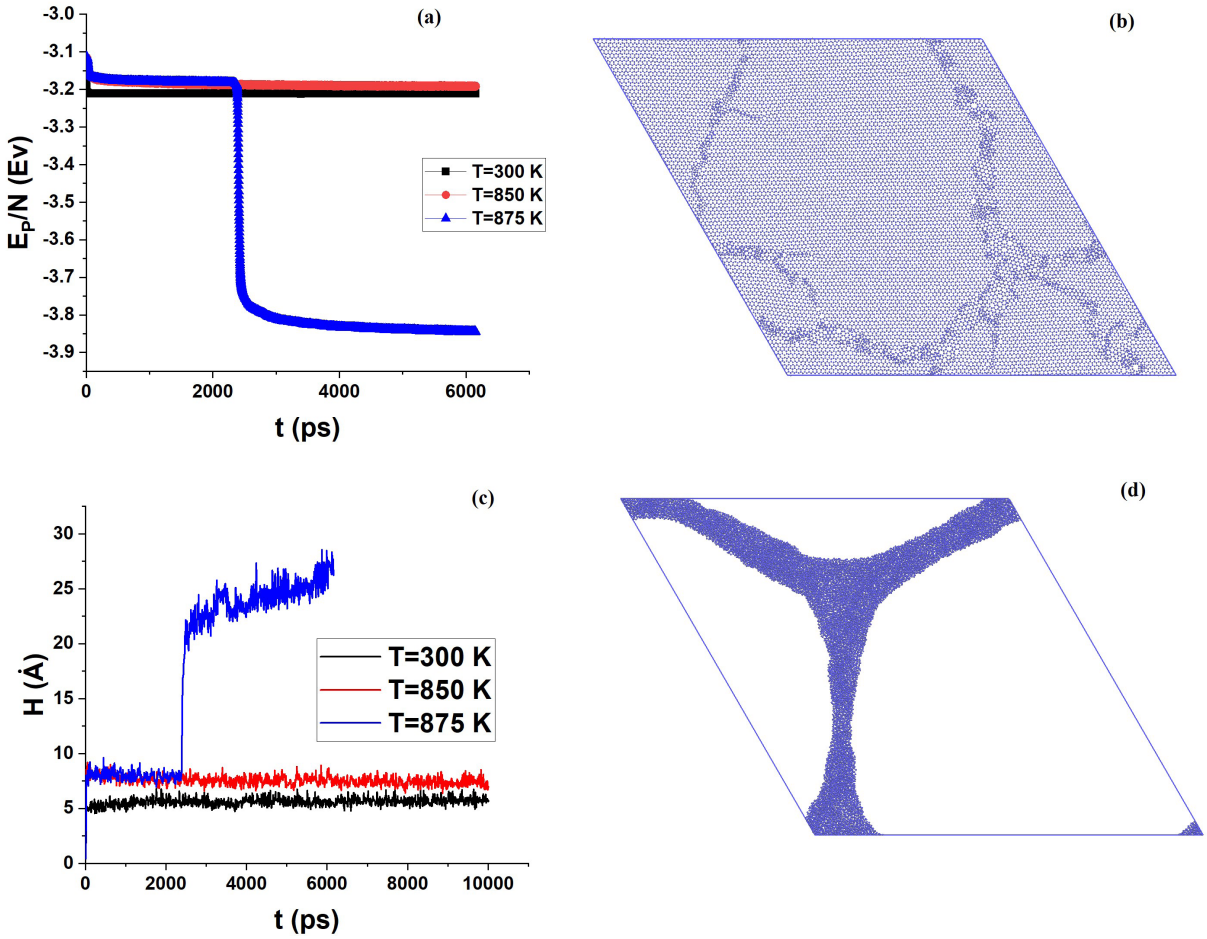

Fig. 2. (a) The time dependence of the potential energy per particle in the system of silicene at different temperatures. (b) The snapshot of the system at T = 850 K. (c) The time dependence of the thickness of the system at different temperatures. (d) The same as (b) at T = 875 K

of the triple point, it is not far from the P = 1 bar and T = 1.673 K. Therefore, it is possible that the heating of silicon at ambient pressure will cause melting rather than sublimation.

This conclusion is illustrated in the snapshots, which show the final structures of the systems at T = 850 and 875 K. In the case of T = 850 K, the system remains in the state of a strongly defective silicene layer, but the two-dimensional lattice is still retained. At the same time, at T = 875 K, the silicene layer breaks due to the formation of voids. Strongly compressed silicon atoms form a Y-shaped 'island'. Such structures appear in molecular simulations in liquid–gas two-phase regions: since the density of the gas phase is much smaller than the one of a liquid, the gaseous regions look like voids. We conclude that the heating of the silicene sample leads to a transition into the liquid–gas two-phase region, i. e. it is neither melting nor sublimation, but something in-between.

Conclusions

In the present paper, we have performed molecular dynamics simulations of the crystal structure collapse of graphene, graphite and silicene. It is shown that in the case of graphene and graphite, the crystal structure collapse is related to the sample sublimation. At the same time, when the silicene sample is heated at constant volume, it comes into the liquid–gas two-phase region of the phase diagram. The difference in the crystal structure collapse of graphene and silicene is caused by the differences in the pressure of the liquid–gas–crystal triple point: while in the case of carbon the pressure of the triple point is very high (P_{tr} =16 MPa), the pressure of the triple point of silicone is close to the ambient one.

Conflict of Interest

The authors of this work declare that they have no conflict of interest.

Author Contributions

Yu. D. Fomin performed the simulations and wrote the manuscript, and E. N. Tsiok and V. N. Ryzhov analyzed the results and wrote the manuscript.

Acknowledgements

The authors are grateful to V. V. Brazhkin for his interest in the work and useful discussions of various aspects of the subject. The work was partially performed using the equipment of the Interdepartmental Supercomputer Center and with computing resources of the federal collective usage center "Complex for Simulation and Data Processing for Mega-science Facilities", both affiliated with the National Research Center "Kurchatov Institute".

References

Agrawal, P. M., Raff, L. M., Komanduri, R. (2005) Monte Carlo simulations of void-nucleated melting of silicon via modification in the Tersoff potential parameters. *Physical Review B*, 72, article 125206. https://doi.org/10.1103/PhysRevB.72.125206 (In English)

Babichev, A. P., Babushkina, N. A., Bratkovsky, A. M. et al. (1991) *Fizicheskie velichiny. Spravochnik [Physical quantities. Handbook]*. Moscow: Energoatomizdat Publ., 1232 p. (In Russian)

Bocchetti, V., Diep, H. T., Enriquez, H. et al. (2014) Thermal stability of standalone silicene sheet. *Journal of Physics: Conference Series*, 491, article 012008. https://doi.org/10.1088/1742-6596/491/1/012008 (In English)

Das, D. K., Sarkar, J. (2018) Multiscale modeling of thermal properties of silicene using molecular dynamics. *Modern Physics Letters B*, 32 (27), article 1850331. https://doi.org/10.1142/S0217984918503311 (In English)

Leider, H. R., Krikorian, O. H., Young, D. A. (1973) Thermodynamic properties of carbon up to the critical point. *Carbon*, 11 (5), 555–563. https://doi.org/10.1016/0008-6223(73)90316-3 (In English)

Los, J. H., Zakharchenko, K. V., Katsnelson, K. V., Fasolino, A. (2015) Melting temperature of graphene. *Physical Review B*, 91, article 045415. https://doi.org/10.1103/PhysRevB.91.045415 (In English)

Min, T. K., Yoon, T. L., Lim, T. L. (2018) Molecular dynamics simulation of melting of silicone. *Materials Research Express*, 5 (6), article 065054. https://doi.org/10.1088/2053-1591/aacdb7 (In English)

On, V. V. (2020) To study the structure and thermodynamic properties of silicene materials when melting quickly by molecular dynamics simulation. *Journal of Physics: Conference Series*, 1706, article 012023. https://doi.org/10.1088/1742-6596/1706/1/012023 (In English)

Orekhov, N. D., Stegailov, V. V. (2015) Kinetics of graphite melting. *Doklady Physics*, 60 (3), 109–113. https://doi.org/10.1134/S1028335815030052 (In English)

Stillinger, F. H., Weber, T. A. (1985) Computer simulation of local order in condensed phases of silicon. *Physical Review B*, 31 (8), 5262–5271. https://doi.org/10.1103/PhysRevB.31.5262 (In English)

Stuart, S. J., Tutein, A. B., Harrison, J. A. (2000) A reactive potential for hydrocarbons with intermolecular interactions. *The Journal of Chemical Physics*, 112 (14), 6472–6486. https://doi.org/10.1063/1.481208 (In English)

Tersoff, J. (1989) Modeling solid-state chemistry: Interatomic potentials for multicomponent systems. *Physical Review B*, 39 (8), 5566–5568. https://doi.org/10.1103/PhysRevB.39.5566 (In English)

Zakharchenko, K. V., Fasolino, A., Los, J. H., Katsnelson, M. I. (2011) Melting of graphene: From two to one dimension. *Journal of Physics: Condensed Matter*, 23, article 202202. https://doi.org/10.1088/0953-8984/23/20/202202 (In English)

Check for updates

Condensed Matter Physics.
Physics of thin films.
Surfaces and interfaces

UDC 538.956

EDN PVLCLE
https://www.doi.org/10.33910/2687-153X-2024-5-4-177-186

Dielectric properties of thin-film metal/dielectric nanocomposites based on zirconium nitrides

A. A. Galiullin ✉[1], I. V. Lunev [1], A. I. Gumarov [1], I. V. Yanilkin [1]

[1] Kazan Federal University, 18 Kremlyovskaya Str., Kazan 420008, Russia

Authors

Artur A. Galiullin, ORCID: 0000-0002-4872-1486, e-mail: www.ag95@mail.ru

Ivan V. Lunev, ORCID: 0000-0001-6201-4393, e-mail: lounev75@mail.ru

Amir I. Gumarov, ORCID: 0000-0002-7250-4377, e-mail: amir@gumarov.ru

Igor V. Yanilkin, ORCID: 0000-0002-8879-8904, e-mail: yanilkin-igor@yandex.ru

For citation: Galiullin, A. A., Lunev, I. V., Gumarov, A. I., Yanilkin, I. V. (2024) Dielectric properties of thin-film metal/dielectric nanocomposites based on zirconium nitrides. *Physics of Complex Systems*, 5 (4), 177–186. https://www.doi.org/10.33910/2687-153X-2024-5-4-177-186 EDN PVLCLE

Received 5 September 2024; reviewed 11 October 2024; accepted 11 October 2024.

Funding: This research was supported by the grant allocated to Kazan Federal University as part of the state-commissioned research assignment (project number FZSM-2023-0012).

Copyright: © A. A. Galiullin, I. V. Lunev, A. I. Gumarov, I. V. Yanilkin (2024) Published by Herzen State Pedagogical University of Russia. Open access under CC BY-NC License 4.0.

Abstract. Zirconium oxynitride films were synthesized by sputtering zirconium nitride with subsequent atmospheric annealing to oxynitride. The resulting films were studied by dielectric spectroscopy. It was shown that the annealing temperature affects the dielectric properties of the film. Atmospheric annealing leads to dispersion of the permittivity and relaxation processes. The nonlinear nature of the temperature dependence of the relaxation time and the difference in the relaxation times are manifestations of the heterogeneous structure of the films and the size effect of the metal/dielectric structure.

Keywords: heterogeneous materials, dielectric spectroscopy, dielectric relaxation, zirconium oxynitrides, thin films

Introduction

Thin-film metal-dielectric composites based on transition metal nitrides are of considerable interest to photonics. In their pure form, they are modern plasmonic materials with an advantage over traditional silver, gold, and copper. This advantage is refractoriness. They play a significant role in such dynamic fields as telecommunications, information processing and storage, quantum information technologies, and spectroscopy.

The literature analysis has shown that zirconium oxynitride films are usually synthesized by reactive magnetron sputtering in a mixture of argon (active gas), oxygen, and nitrogen (reactive gases) (Carvalho et al. 2008; Courts, Swinehart 2003). In this case, the key parameter determining the resistive properties of the film is the ratio of the fractions of active and reactive gases.

Resistance thermometers (RTD) are commercially available and are made on the basis of ruthenium dioxide, rhenium oxide, rhodium with the addition of iron, platinum, zirconium nitride and oxynitride, germanium. They also include silicon and aluminum gallium arsenide diodes (Carvalho et al. 2008; Mohamed et al. 2015). The main difference between all these materials is the operating temperature range.

Heat treatment of zirconium oxynitride in air directly affects its physical properties. The effect of heat treatment on zirconium oxynitride was studied by You, *et al.* (You et al. 2022). Annealing of the samples resulted in a decrease in the nitrogen content and a spontaneous increase in the oxygen content. A huge increase in specific electrical resistance was observed during oxidation. Films annealed at higher temperatures (≥ 723 K) showed insulating properties.

The effect that the regulation of the oxygen content has on the structure and properties of this type of film was studied by (Mohamed et al. 2015). Oxygen atoms replace nitrogen atoms, introduce a Zr vacancy into the ZrN structure, and lead to a phase transition from ZrN to Zr_3N_4. Even small changes in the oxygen content lead to an electronic transition from metallic to semiconductor behavior in the ZrN structure. (da Silva-Oliveira et al. 2018; Khan et al. 2017) investigated the effect of heat treatment on the structural, morphological and mechanical properties of zirconium oxynitride films.

(Streibel et al. 2024) investigated the applicability of zirconium oxynitride thin films as semiconductor photoanodes, as well as the effect of annealing on photoelectrochemical characteristics.

During this study, metal/dielectric composites based on zirconium oxynitride were synthesized. The study analyses and describes the dielectric properties of thin-film metal/dielectric nanocomposites based on nitrides in wide temperature and frequency ranges.

Materials and methods

The films were synthesized by reactive magnetron sputtering of zirconium onto single-crystal, 0001-oriented corundum substrates (Monocrystal, Russia). The substrate surfaces were prepared in several stages. After an ultrasonic bath in acetone (high purity grade) and isopropyl alcohol (high purity grade), they were annealed at 1073 K for 5 minutes in an ultrahigh vacuum chamber (SPECS, Germany) with a residual vacuum of ~ 2×10^{-10} mbar. After annealing, the sample was moved along an ultrahigh vacuum line into a magnetron sputtering chamber (BESTEC, Germany) with a residual gas pressure below 5×10^{9} mbar.

The magnetron operated in DC mode, the discharge power was 50 W, the target was a zirconium washer (99.5% purity, GIRMET Ltd, Russia), 5 mm thick and 5 cm in diameter. Zirconium oxynitride films were synthesized in two stages: 1) zirconium nitride sputtering; 2) annealing of the nitride film in air for one hour to obtain oxynitride. The annealing temperature critically affects the resistive properties of the film. To protect the films against further uncontrolled exposure to the atmosphere, they were covered with a 20 nm thick zirconium oxide film after preliminary cleaning with argon ions. The initial zirconium nitride film has a resistivity of 0.29 mOhm×m at 300 K, which is two orders of magnitude higher than typical values for ZrN films. This is due to the presence of oxygen in the film, amounting to 15 at.%. The resistivity of zirconium oxynitride films annealed in air increases and is determined by the annealing temperature (up to the dielectric state), which is associated with an increase in the proportion of the oxide phase in the composite.

High-purity argon (> 99.99%) was used as a plasma-forming gas at a pressure of 6×10^{-3} mbar. For reactive spraying of nitride or zirconium oxide, nitrogen or oxygen (both gases with purity > 99.99%) were additionally introduced into the chamber, respectively, while maintaining the operating pressure unchanged. This gas purity (1 ppm) is achieved through the use of fine filters (PerkinElmer). The filter system is integrated into the gas aftertreatment stand through which all gases used in spraying experiments are filtered. When spraying zirconium nitride, the substrate was maintained at a temperature of 573 K, when spraying the oxide, at room temperature. To determine the spraying mode, the deposition rate was measured on a quartz thickness gauge (INFICON) depending on the composition of the plasma-forming gas. As a result, a concentration of about 3.9% was selected for both reactive gases, which corresponds to the spraying of the oxidized target surface ('oxidized' mode). The deposition rate of zirconium nitride was 1.5 nm/min, while it was 0.9 nm/min for zirconium oxide.

The electrical properties of the samples were studied using the dielectric spectroscopy on the Novocontrol Concept BDS-80 broadband measuring complex. Electrical characteristics were measured in the frequency range from 10^{-1} Hz to 10^{7} Hz and the temperature range from 123 to 473 K, with a step of 5 K.

The sample under study is located in the measuring cell (a plane-parallel capacitor), which is placed in the measuring head. During the measurements, the head is immersed in a cryothermostat chamber connected to a gaseous nitrogen supply line from the cooling system. The cooling rate is regulated by a programmable system for supplying gaseous nitrogen from a Dewar vessel due to the evaporation of liquid nitrogen. A temperature sensor with an accuracy of ± 0.1 K is connected to the measuring head.

See Supplementary Materials (Figure S1) for the temperature protocol for the dielectric measurements.

 https://www.doi.org/10.33910/2687-153X-2024-5-4-177-186

The studied sample was cooled to a temperature of 123 K. After the temperature stabilized, the dielectric spectrum was measured. Then the temperature was increased by 5 K, stabilized, and the next measurement was carried out. Upon reaching a temperature of 473 K and measuring the dielectric spectrum, the experiment was completed.

Samples of ZrON metal-dielectric films on a dielectric substrate Al_2O_3 were studied. The substrate and film samples with different temperatures of annealing were measured separately. The characteristics of the samples are given in Table 1.

Table 1. Characteristics of the studied ZrON-based samples

Sample	Thickness, mm	Annealing time, h	Annealing temperature, K
Al_2O_3 substrate	0.66	–	–
ZrN	0.660123	–	–
ZrON_573	0.660123	1	573
ZrON_623	0.660123	1	623

Results

Al_2O_3 substrate

Figure 1a shows the real part of the permittivity of the corundum substrate.

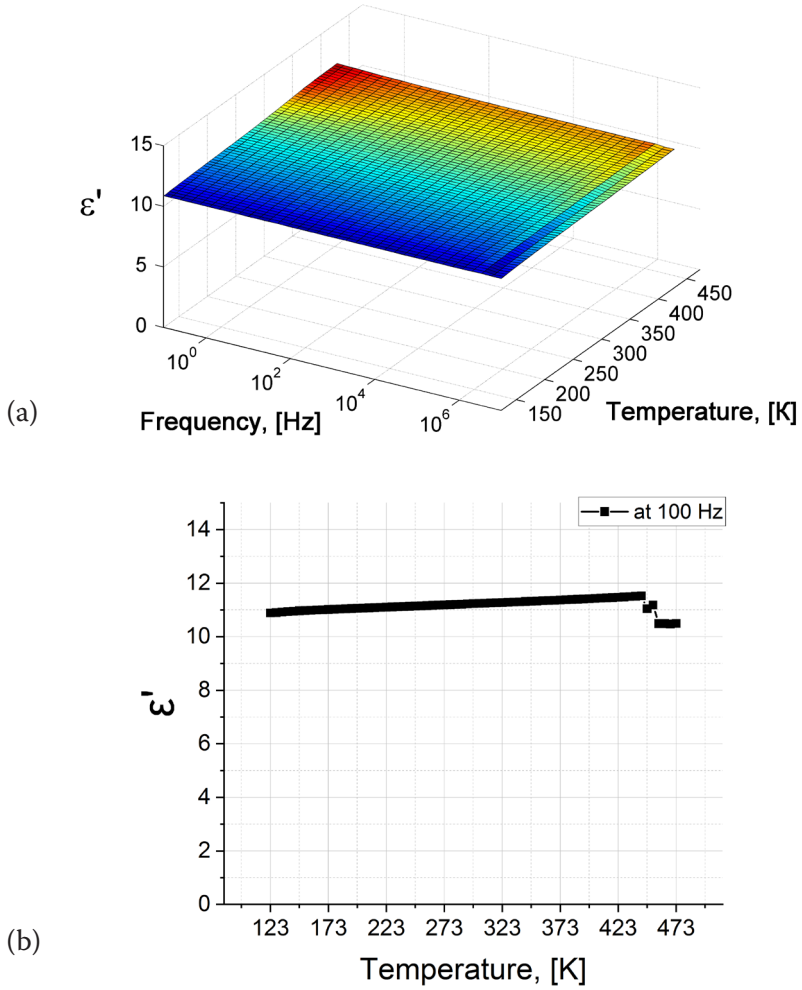

Fig. 1. 3D diagram in (f, T, ε') coordinates (a) and temperature dependence at a frequency of 100 Hz (b) of the real part of the permittivity of the Al_2O_3 substrate

The substrate demonstrates good dielectric properties, the real part of the permittivity increases linearly with increasing temperature (Figure 1b). At temperatures above 443 K there is some instability, probably related to the measurement technique.

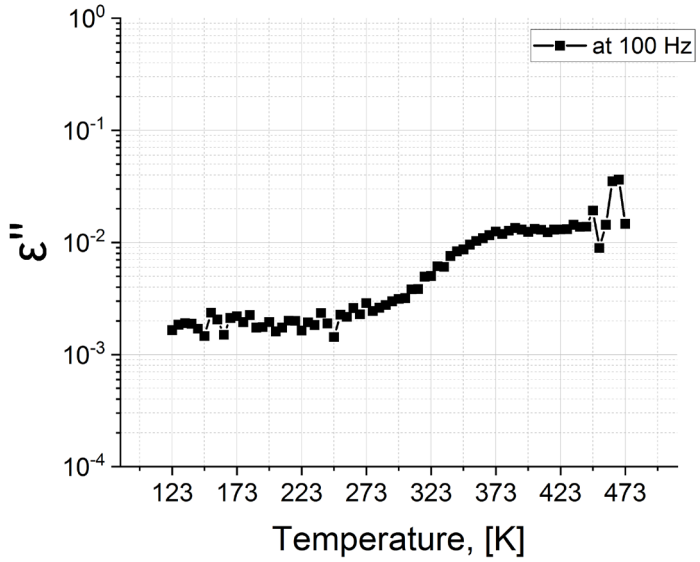

Fig. 2. Temperature dependence of the imaginary part of the permittivity of the Al_2O_3 substrate at a frequency of 100 Hz

No relaxation processes are observed in the entire temperature range. At a temperature of 293 K, the permittivity ε' equals to 11.2, dielectric losses $\varepsilon'' = 0.003$ (Figure 2).

ZrN film on the substrate without annealing

Figures 3a and 3b show three-dimensional diagrams of the real and imaginary parts of the permittivity of the ZrN film on the substrate without annealing. At a temperature of about 350 K, a local increase in the permittivity value is observed. This may be due to structural defects in the deposited film.

In direct current mode the ZrN film shows metallic properties and has a specific resistance of 0.29 mOhm×m, although dielectric properties are manifested on alternating current in the frequency range of 10^3–10^7 Hz. Therefore, it was possible to measure the dielectric characteristics in the specified frequency range. The sample has a through conductivity of $\sigma_0 = 2.5 \times 10^{-5}$ Sm×m^{-1} at a temperature of 293 K. It might be due to the film material getting onto the edges of the substrate during the synthesis.

Figure 4 shows the temperature dependence of the permittivity of the ZrN film determined at a frequency of 1 kHz. In the temperature range of 348–373 K, uneven behavior of ε' and ε'' is observed. This is probably due to the heterogeneous composition of the sample.

ZrON film after annealing at a temperature of 573 K

Figures 5a and 5b show 3D diagrams of the real and imaginary parts of the permittivity of the ZrON_573 sample.

A relaxation process is observed in the entire temperature range of 123–473 K (Figure 5b). The increase in amplitude in the frequency range of 10^{-1}–10^2 Hz in the temperature range of 300–473 K (Figure 5a) is associated with the manifestation of electrode polarization.

The relaxation process in the obtained spectra was approximated by superposition of the Cole-Cole function (Cole, Cole 1941) and Jonscher function:

$$\varepsilon^*(\omega) = \varepsilon'(\omega) - i\varepsilon''(\omega) = \varepsilon_\infty + \frac{\Delta\varepsilon}{1+(i\omega\tau)^\alpha} + B(i\omega)^{n-1}, \quad (1)$$

ε' and ε'' denotes the real and imaginary parts of the complex permittivity, $\omega = 2\times\pi\times f$ is the cyclic frequency. The parameter ε_∞ denotes the extrapolated high-frequency permittivity, and $\Delta\varepsilon = \varepsilon_s - \varepsilon_\infty$ is the relaxation amplitude (the permittivity low-frequency limit is denoted by ε_s). The parameter τ is the

 https://www.doi.org/10.33910/2687-153X-2024-5-4-177-186

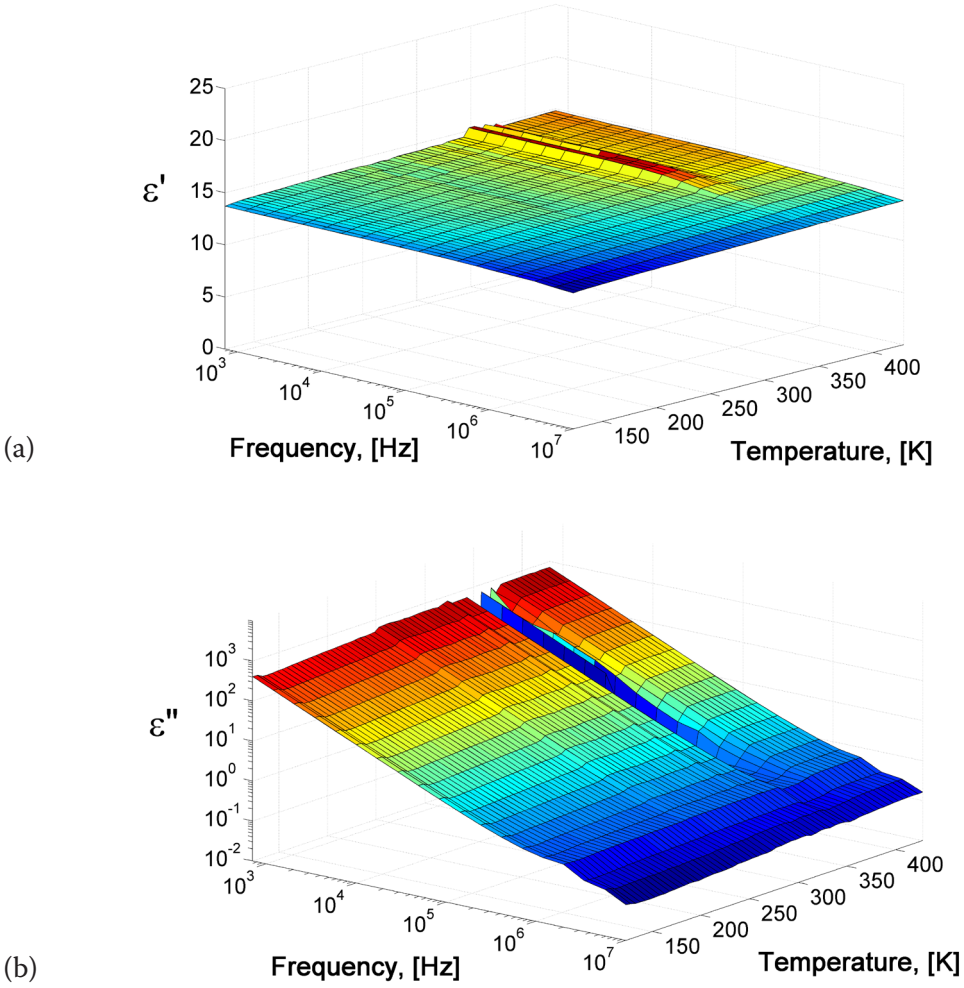

Fig. 3. 3D diagrams of the real (a) and imaginary (b) parts of the permittivity of the ZrN film on the substrate without annealing

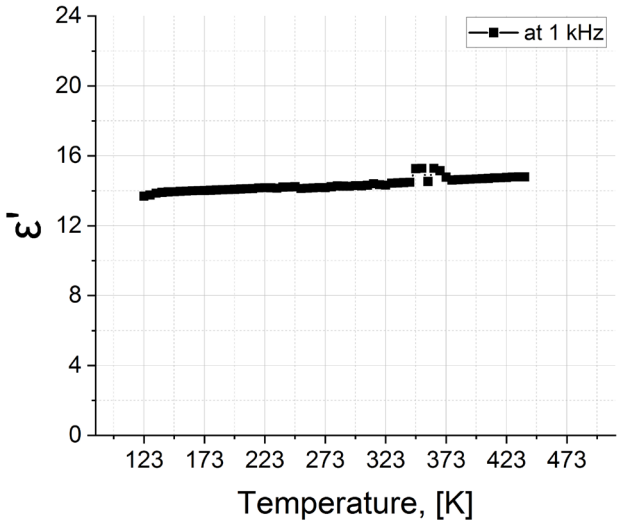

Fig. 4. Temperature dependence of the real part of the permittivity of the ZrN film

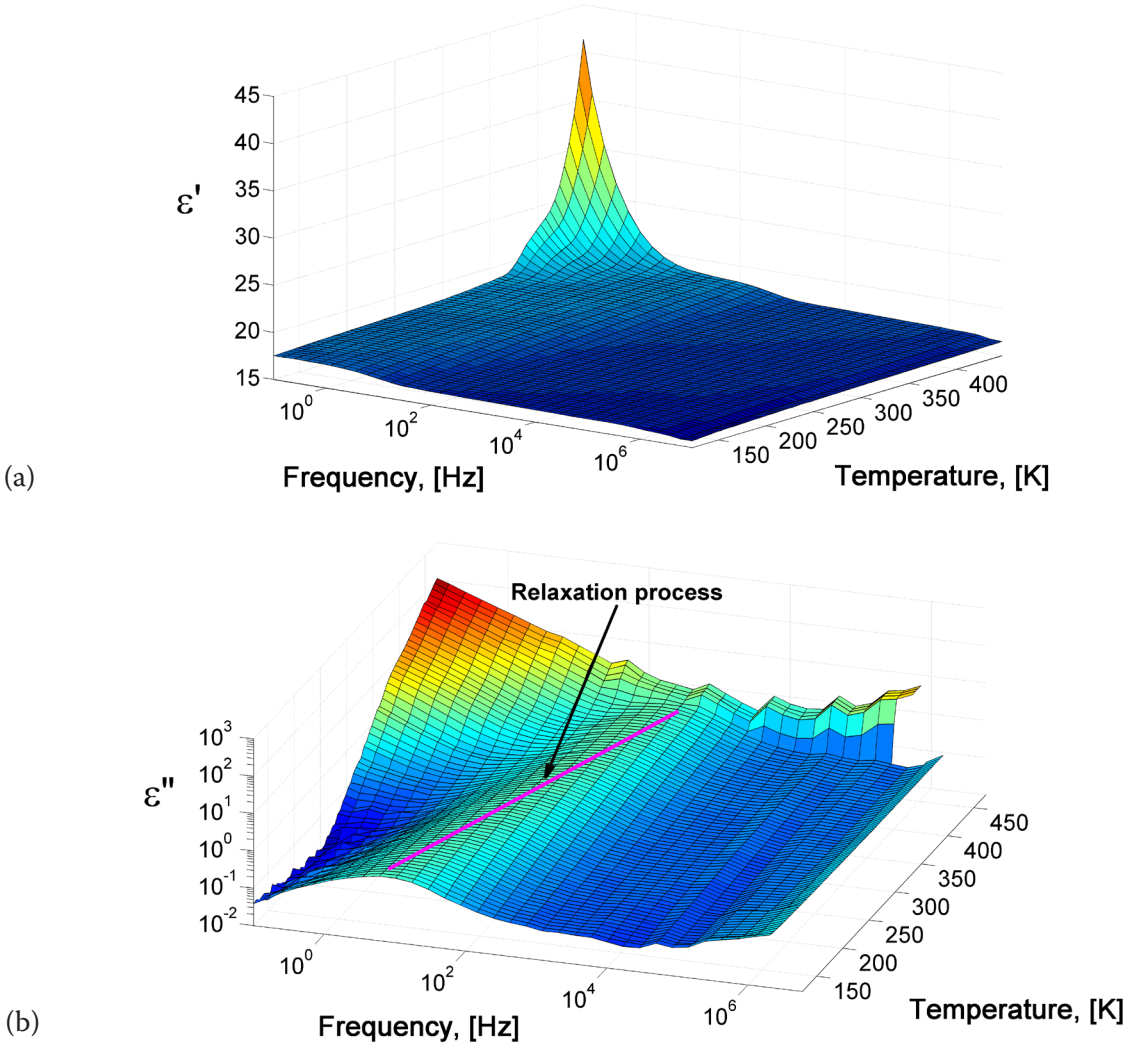

Fig. 5. 3D diagrams of the real (a) and imaginary (b) parts of the permittivity of the ZrON_573 sample

relaxation time. The exponent α ($0 < \alpha \leq 1$) is a measure of the symmetric broadening of the spectrum. The Jonscher function takes into account electrode effects. B is the contribution of the Jonscher function, $0 < n \leq 1$ is the function parameter.

ZrON film after annealing at 623 K

Figures 6a and 6b show 3D diagrams of the real and imaginary parts of the permittivity of the ZrON_623 sample. The relaxation process is observed in the entire temperature range of 123–473 K.

The relaxation process under consideration is described by formula (1). The increase in amplitude in the frequency range of 10^{-1}–10^{2} Hz in the temperature range of 300–473 K (Figure 10 and 11) is associated with the manifestation of the effect of electrode polarization.

Discussion

As a result of measuring the electrical properties of the samples indicated in Table 1 in the frequency range of 10^{-1}–10^{7} Hz and the temperature range of 123–473 K, the dielectric characteristics, permittivity ε' and relaxation time τ were determined, using formula (1).

Figure 7 shows the temperature dependences of permittivity ε'.

From Figure 7 it is evident that upon application of the ZrN film onto the Al_2O_3 substrate and its subsequent oxidation, the permittivity of the samples increases. If we consider the values of ε' at a temperature of 300 K, it is evident that ε' increases. For the substrate, ε' equals 11.2. After application of the ZrN film, the permittivity increases to a value of $\varepsilon' = 14.3$. After annealing at a temperature of 573 K for

 https://www.doi.org/10.33910/2687-153X-2024-5-4-177-186

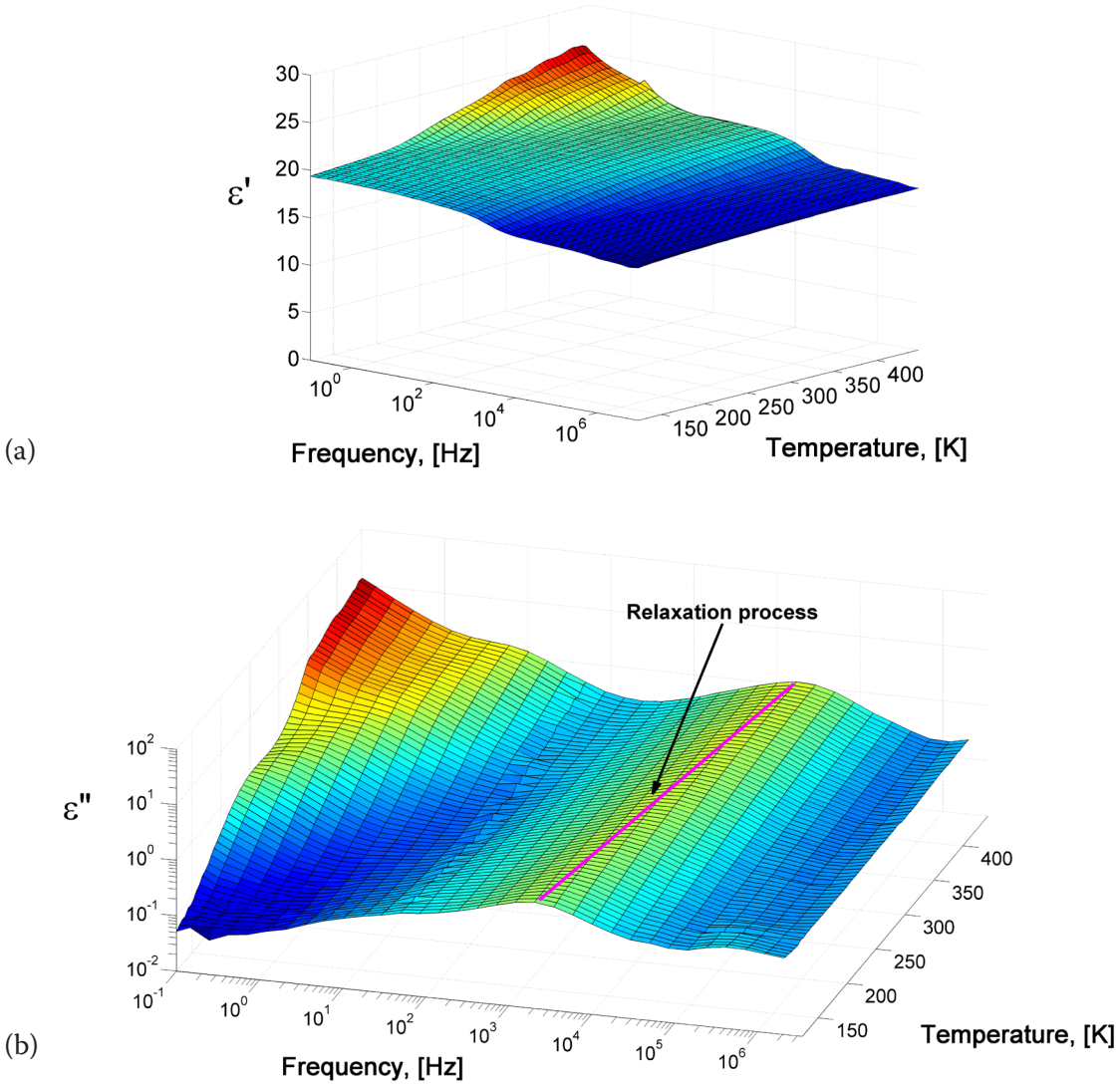

Fig. 6. 3D diagrams of the real (a) and imaginary (b) parts of the permittivity of the ZrON_623 sample in (f, T, ε′) coordinates

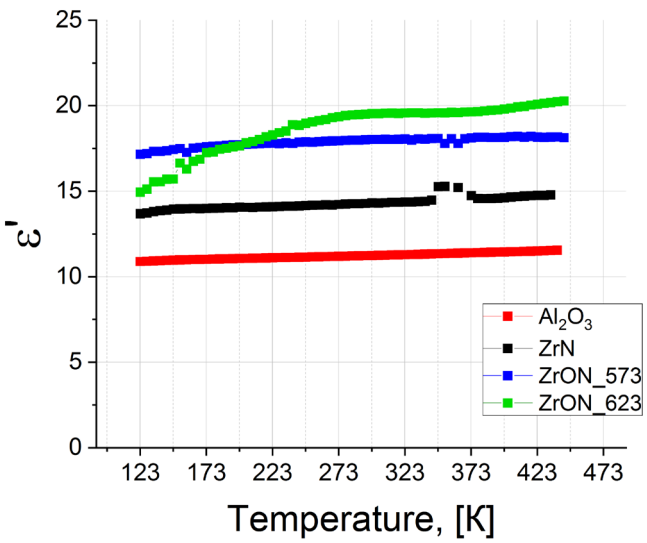

Fig. 7. Temperature dependence of the permittivity of the studied samples

one hour, the permittivity increases and has a value of $\varepsilon' = 18$. With further oxidation and annealing of the ZrN foam sample on the Al_2O_3 substrate for one hour at a temperature of 623 K, the permittivity value $\varepsilon' = 19.5$. For the ZrON_623 sample, the temperature dependence of $\varepsilon'(T)$ is non-uniform; in the temperature range of 123–300 K, it rapidly increases from 14.9 at 123 K to 19.5 at 300 K, then increases more smoothly with increasing temperature. Apparently, this is the way the heterogeneous structure of the ZrON_623 sample becomes manifest: it increases with increasing annealing temperature.

Figure 8 shows the temperature dependences of the relaxation time τ and processes detected in the ZrON_573 and ZrON_623 samples, in Arrhenius coordinates.

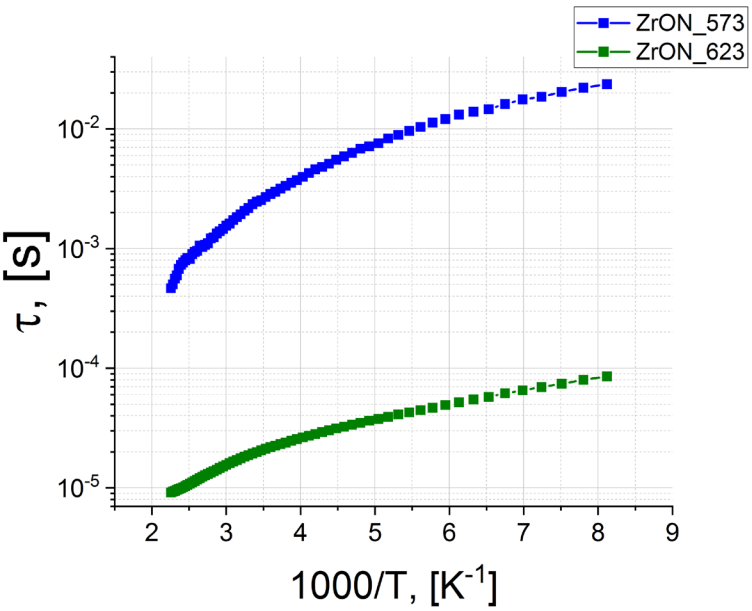

Fig. 8. Temperature dependence of the relaxation time τ of the ZrON_573 and ZrON_623 samples in Arrhenius coordinates

As was said earlier, no relaxation processes were observed in the ZrN substrate and film samples. Relaxation processes became manifest in the oxidized samples. The $\tau\ (1000/T)$ dependencies are non-linear (Figure 8). The ZrON_573 sample is characterized by longer relaxation times. The ZrON_623 sample has shorter relaxation times compared to ZrON_573. Apparently, during oxidation of zirconium due to atmospheric annealing, a change in the film structure occurs with the formation of dielectric regions. An increase in the annealing temperature leads to an increase in the number of dielectric regions and a wider distribution of their sizes, as well as an increase in the rate of charge exchange, which leads to a decrease in the relaxation time.

The mechanism by which dielectric dispersion occurs is as follows. The synthesized film has a metallic type of conductivity, that is, electrons transfer the charge, and there is no dielectric dispersion. The film under study has a polycrystalline granular structure. During atmospheric annealing, oxygen penetrates into the space between the grains, oxidizing particles of zirconium nitride ZrN to zirconium oxynitride ZrON, which is a dielectric. Thus, the film is transformed into a metal-dielectric composite. Dielectric particles are a kind of defect in the film structure that limits the mobility of electrons. This leads to the localization of electrons near defects for some time and the appearance of an additional dipole moment, which, in turn, leads to dispersion of the permittivity and the emergence of relaxation processes. An increase in the annealing temperature leads to an increase in the number of dielectric regions and a wider distribution of their sizes, as well as an increase in the rate of charge exchange, which leads to a decrease in relaxation time.

Conclusions

The reported study identified the effect of annealing temperature on the dielectric properties of a zirconium oxynitride film synthesized by zirconium nitride sputtering, followed by atmospheric annealing and the formation of oxynitride. An increase in the permittivity from 14.3 to 18 and 19.5 at a temperature

 https://www.doi.org/10.33910/2687-153X-2024-5-4-177-186

of 300 K was shown for the initial samples and those annealed at temperatures of 573 and 623 K, respectively. Atmospheric annealing leads to a dispersion of the permittivity and relaxation processes. For the samples annealed at a temperature of 573 and 623 K, the temperature dependencies of the relaxation times are nonlinear in Arrhenius coordinates and differ by almost two orders of magnitude. For example, at a temperature of 300 K, the values are 2.3×10^{-3} and 1.9×10^{-5} s, respectively. The nonlinear nature of the temperature dependence of the relaxation time and the difference in the relaxation times for samples annealed at a temperature of 573 and 623 K is a manifestation of their heterogeneous structure and the size effect of the metal/dielectric structure.

Supplementary Materials

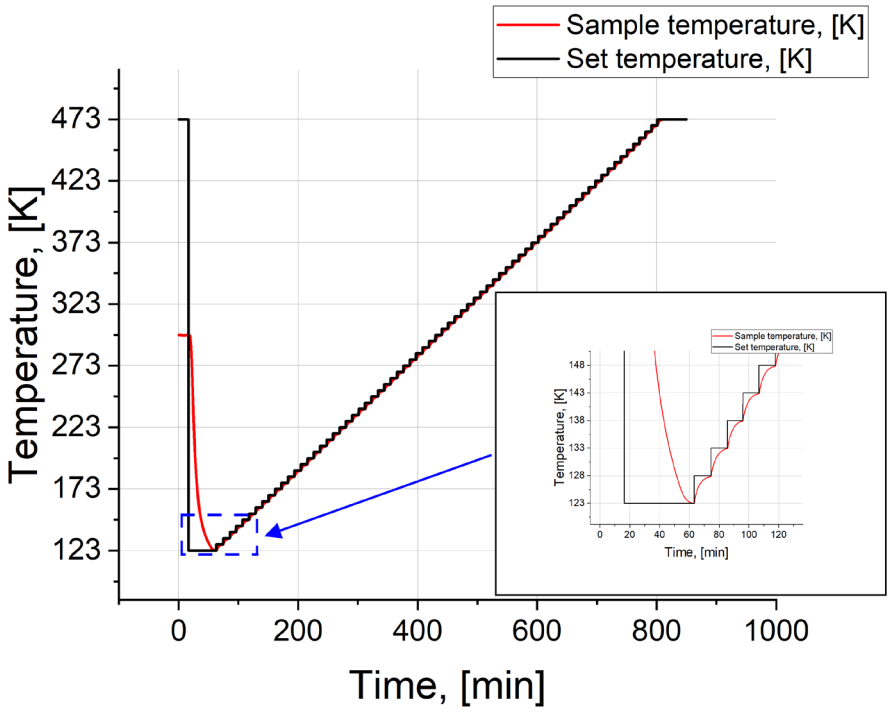

Fig. S1. Temperature protocol of dielectric measurements

Conflict of Interest

The authors declare that there is no conflict of interest, either existing or potential

Author Contributions

I. V. Lunev, A. A. Galiullin — investigation, visualization, writing, metodology; A. I. Gumarov, I. V. Yanilkin — resources.

References

Carvalho, P., Chappé, J. M., Cunha, L. et al. (2008) Influence of the chemical and electronic structure on the electrical behavior of zirconium oxynitride films. *Journal of Applied Physics*, 103 (10), article 104907. https://doi.org/10.1063/1.2927494 (In English)

Cole, K. S., Cole, R. H. (1941) Dispersion and absorption in dielectrics I. Alternating current characteristics. *The Journal of Chemical Physics*, 9 (4), 341–351. https://doi.org/10.1063/1.1750906 (In English)

Courts, S. S., Swinehart, P. R. (2003) Review of Cernox™ (zirconium oxy-nitride) thin-film resistance temperature sensors. *AIP Conference Proceedings*, 684 (1), 393–398. https://doi.org/10.1063/1.1627157 (In English)

Da Silva-Oliveira, C. I., Martínez-Martínez, D., Apreutesei, M. et al. (2018) Thermal stability of Zr-O-N(:Ti) thin films prepared by magnetron sputtering. *Vacuum*, 151, 148–155. https://doi.org/10.1016/j.vacuum.2018.02.002 (In English)

Khan, I. A., Kashif, M., Farid, A. et al. (2017) Effect of annealing temperature on the structural, morphological, and mechanical properties of polycrystalline zirconium oxynitride composite films deposited by plasma focus device. *Japanese Journal of Applied Physics*, 56 (12), article 125501. https://doi.org/10.7567/JJAP.56.125501 (In English)

Mohamed, S. H., Hadia, N. M. A., Ali, H. M. (2015) Effect of annealing on properties of decorative zirconium oxynitride thin films. *European Physical Journal Applied Physics*, 69 (3), article 30301. https://doi.org/10.1051/epjap/2015140475 (In English)

Streibel, V., Schönecker, J. L., Wagner, L. I. et al. (2024) Zirconium oxynitride thin films for photoelectrochemical water splitting. *ACS Applied Energy Materials*, 7 (9), 4004–4015. https://doi.org/10.1021/acsaem.4c00303 (In English)

You, M., Li, Y., Zhang, H. et al. (2022) The mechanism of phase transition induced by oxygen doping in zirconium nitride thin films. *Journal of Materials Science*, 57 (4), 18456–18467. https://doi.org/10.1007/s10853-022-07182-z (In English)

Check for updates

Condensed Matter Physics. Dielectrics

UDC 621.315.61:51-74

EDN HBQYTU
https://www.doi.org/10.33910/2687-153X-2024-5-4-187-194

Field dependence of the initiation time of electrical trees in polymer insulation

V. V. Kiselevich ✉[1]

[1] Sukhoi State Technical University of Gomel, 48 Oktyabrya Ave., Gomel 246029, Belarus

Author

Valentin V. Kiselevich, ORCID: 0000-0003-0542-0939, e-mail: valentinkis@list.ru

For citation: Kiselevich, V. V. (2024) Field dependence of the initiation time of electrical trees in polymer insulation. *Physics of Complex Systems*, 5 (4), 187–194. https://www.doi.org/10.33910/2687-153X-2024-5-4-187-194 EDN HBQYTU

Received 22 July 2024; reviewed 25 September 2024; accepted 25 September 2024.

Funding: The study did not receive any external funding.

Copyright: © V. V. Kiselevich (2024) Published by Herzen State Pedagogical University of Russia. Open access under CC BY-NC License 4.0.

Abstract. The article analyses the known expressions that describe the field dependence of the inception time of electrical trees in polymer insulation. It also highlights the need to modify these expressions to correctly determine the threshold parameters of tree initiation. We used the methods of catastrophe theory to develop the equation that describes the dependence of the tree inception time in polymer dielectrics on the value of the maximum local electric field strength. The parameters of this equation for epoxy and polyethylene insulation are determined. A good agreement has been established between the literature experimental data and the field dependencies of the inception time of trees constructed according to the proposed equation. The geometric properties of the fold catastrophe function, which characterizes the regularities of the change in the time of initiation of electrical trees in polyethylene insulation, are considered.

Keywords: polymer insulation, electrical trees, inception time of trees, maximum local electric field strength, threshold parameters of trees initiation, catastrophe theory, fold catastrophe

Introduction

The widespread use of polymers as insulating materials for various electrical devices causes considerable interest in the study of electrical aging and breakdown processes in polymer dielectrics (Tumusova et al. 2020; Zakrevskii et al. 2020). Knowledge of breakdown mechanisms allows the correct selection of permissible levels of operating and test voltages of electrical insulating structures (Borisova, Marchenko 1998; Dissado, Fothergill 1992). Studies aimed at identifying the patterns of electrical aging of polymer dielectrics, in turn, contribute to the improvement of methods for calculating the life characteristics of electrical insulation (Blythe, Bloor 2005; Borisova, Kojkov 1979).

The process of electrical aging of polymer dielectrics is closely related to the initiation of trees — hollow branched channels, the development of which is accompanied by partial discharges and, ultimately, leads to a breakdown of insulation. At moderate electric field strengths, the root cause of the occurrence and development of trees in polymer insulation, as a rule, is the presence of gas inclusions, foreign impurities in its volume, as well as the presence of mechanically strained molecular bonds (Blythe, Bloor 2005; Kuchinskij 1979). At high values of local strength, the prevailing mechanism for the initiation of trees in polymers is the injection of electrons from metal electrodes (Blythe, Bloor 2005; Dissado, Fothergill 1992).

The breakdown of polymer insulation usually occurs at the stage of development of tree-like channels. Therefore, the main attention of the authors of scientific papers is aimed at studying the mechanisms of development and distribution of trees (Sitole, Nyamupangedengu 2020). Mathematical and physical

models reflecting the patterns of development of electrical trees in polymers are described in detail in (Cai et al. 2019; Dissado et al. 1997; Noguchi et al. 2020; Wang et al. 2023). Analytical expressions that form the basis of such models are often very complex and cumbersome, which seriously constrains their real practical application. Moreover, in order to be able to reliably predict the service life of insulating structures, it is extremely necessary to know the quantitative characteristics of not only the development process but also the process of tree inception. This circumstance is of particular importance in the case of high-voltage electrical devices (insulators of overhead power lines, high- and ultrahigh-voltage cables, thin-film capacitors, etc.). This is due to the fact that the insulation of such devices is often subjected to considerable short-term overvoltages, as a result of which its breakdown can occur already at the stage of the inception of trees (Dissado, Hill 1990).

To quantitatively characterize the process of occurrence of trees, it is customary (Dissado, Fothergill 1992) to use such a parameter as the inception time, determined by the maximum electric field strength affecting the dielectric. The regularities of the change in the inception time of trees in polymer dielectrics when varying the value of the applied voltage were studied in (Dissado, Hill 1990; Hu et al. 2012; Sitole, Nyamupangedengu 2020; Tanaka, Greenwood 1978), where the exponential equation (Tanaka, Greenwood 1978) was used to process the experimental data. At the same time, as is known (Dissado, Fothergill 1992), at small levels of applied voltage, the exponential law can give greatly overestimated values of the tree inception time.

The purpose of this paper is to derive an equation to describe the dependence of the tree inception time on the value of the maximum electric field strength and to determine the parameters of this equation for epoxy and polyethylene insulation.

Formulation of the problem

It is known (Kuchinskij 1979) that the time t_{tr} of the tree inception in polymer insulation depends on the maximum strength E_m of the electric field at the place of occurrence of inhomogeneity. At a given voltage level, the maximum local strength E_m depends on two main factors: the shape of the inhomogeneity and the geometry of the electrodes. The known formulas for determining E_m, taking into account these factors, are presented in publications (Blythe, Bloor 2005; Dissado, Hill 1990; Kuchinskij 1979).

In practice, the time interval from the beginning of voltage supply to the insulation until the appearance of hollow channels with partial discharges at the level of tenths of pC is taken as t_{tr}. The minimum value of E_m, at which the appearance of trees is possible in electrical insulation, is called the threshold strength E_{th} of tree initiation, and the time t_{tr} corresponding to this strength is the threshold time t_{th} of tree inception. Under the given conditions of the experiment (the geometry of the electrodes, the thickness of the samples, and the environmental parameters), the value of E_{th} depends solely on the properties and state of the dielectric material.

The experimental curves reflecting the field dependence $t_{tr} = f(E_m)$ of the tree inception time in the polymer dielectric volume are satisfactorily described by the inverse power law (Kuchinskij 1979)

$$t_{tr}(E_m) = a / E_m^b \tag{1}$$

and exponential law (Sitole, Nyamupangedengu 2020; Tanaka, Greenwood 1978)

$$t_{tr}(E_m) = c\left[\exp\left(-kW_e^{3/2}/E_m\right) - \exp\left(-kW_e^{3/2}/E_{th}\right)\right]^{-1}. \tag{2}$$

Here a, b and c, k are the parameters determined by the properties of the dielectric material; W_e is the effective work function of electrons from the metal of the electrode.

The parameters of equations (1) and (2) are most often (Sitole, Nyamupangedengu 2020) selected based on the condition of the best smoothing of the experimental curves $t_{tr} = f(E_m)$. Due to the fact that the E_{th} value is not included in expression (1), an experiment is required to assess the threshold time t_{th} of tree initiation. However, the direct experimental determination of t_{th} is fraught with great difficulties, since when E_m decreases, the statistical spread between the obtained t_{tr} values increases, and as E_m approaches the preliminary predicted limit of E_{th}, the spread can reach two or three orders of magnitude (Dissado, Hill 1990; Sitole, Nyamupangedengu 2020). This is due not so much to the conditions of the experiment and the errors inevitable when approximating the experimental curves with theoretical expressions, as to the increase in the influence of the degree of inhomogeneity of the dielectric material

 https://www.doi.org/10.33910/2687-153X-2024-5-4-187-194

on the process of initiation and development of electrical trees when the maximum local strength tends to its threshold value.

In the exponential law (2), the limit value E_{th} corresponds to time $t_{th} \to \infty$. Meanwhile, in reality, even when the insulation is under voltage, which creates local areas of strength $E_m \approx E_{th}$ in it, the time t_{th} will be finite. In addition, the hypothesis about the correlation between the effective work function W_e and the strength E_{th} of the onset of tree initiation, used in deriving the exponential dependence (2), did not find proper experimental confirmation (Tanaka, Greenwood 1978).

Based on the foregoing, it can be concluded that obtaining an expression of field dependence $t_{tr} = f(E_m)$, free from these shortcomings of the known relations (1) and (2), is a rather relevant task. To derive the equation $t_{tr} = f(E_m)$, we will use the methods of catastrophe theory (Gilmore 1993).

Theoretical analysis

To be able to analyze the dependence $t_{tr} = f(E_m)$ in line with the mathematical catastrophe theory, first, it is necessary to identify the characteristic features — the flags of catastrophes (Gilmore 1993), which can be used to judge the presence of a catastrophe in a polymer dielectric exposed to an electric field. The fact of the existence of a threshold (critical) strength E_{th}, upon reaching which the process of tree inception begins in the dielectric, is the first sign of the probable presence of a catastrophe. The second sign of a catastrophe can be the above anomalous dispersion of the experimental values of the tree inception time t_{tr} in the case $E_m \approx E_{th}$.

The description of physical systems in catastrophe theory is performed using potential functions Φ (catastrophe functions), the form of which is determined by the complexity of the system under consideration. Suppose that the time t_{tr} of the inception of electric trees mainly depends on one significant parameter — the maximum local strength E_m of the electric field. Then, to establish the analytical relationship between t_{tr} and E_m in the first approximation, we can limit ourselves to considering the one-parameter fold catastrophe.

The known expression for the function Φ of the fold catastrophe has the form (Gilmore 1993):

$$\Phi(\chi;\ \mathcal{A}) = \chi^3/3 + \mathcal{A}\chi\,, \tag{3}$$

where χ is a variable that determines the state of the system under study; $\mathcal{A}$ is a control parameter, the smooth variation of which leads to a continuous or abrupt ('catastrophic') change in the variable χ.

The mathematical parameters χ and $\mathcal{A}$ included in equation (3) are dimensionless. To establish the relationship between the dimensionless parameters χ, $\mathcal{A}$ and their corresponding dimensional analogs *x*, *A*, normalization relations are used (Gilmore 1993):

$$\chi = x/x_{\mathcal{D}} - 1;\quad \mathcal{A} = A/A_{\mathcal{D}} - 1\,, \tag{4}$$

where *x* is the physical state variable; *A* is the physical control parameter; $x_{\mathcal{D}}$ and $A_{\mathcal{D}}$ are the critical parameters of the catastrophe function, which are understood as the values of the quantities *x* and *A* at the physical critical point identified with the mathematical point $\mathcal{D}$. In the case of a fold catastrophe, point $\mathcal{D}$ is a doubly degenerate critical point at which $\partial\Phi/\partial\chi = \partial^2\Phi/\partial\chi^2 = 0$ (Gilmore 1993).

It follows from equation (3) that the mathematical control parameter $\mathcal{A}$ is proportional to the square of the state variable χ: $\mathcal{A} \sim -\chi^2$. Therefore, given the proportionality $1/t_{tr} \sim E_m^b$ (where $b \geq 2$) characteristic of the physical quantities t_{tr} and E_m, it is convenient to take the strength E_m and not the time t_{tr} as a state variable; the value $v_{tr} = 1/t_{tr}$ will be considered a physical control parameter.

Let us match the physical critical point for which $E_m = E_{th}$ and $t_{tr} = t_{th}$ (or $v_{tr} = v_{th}$) to the mathematical point $\mathcal{D}$. Then the threshold physical parameters t_{th}, v_{th}, E_{th} will become equivalent to the critical parameters of the catastrophe function: $t_{th} \equiv t_{\mathcal{D}}$, $v_{th} \equiv v_{\mathcal{D}}$, $E_{th} \equiv E_{\mathcal{D}}$.

Next, using the normalization relations (4), we reduce the dimensional physical quantities E_m and v_{tr} to a dimensionless form

$$\mathcal{E}_m = E_m/E_{\mathcal{D}} - 1;\ \mathcal{V}_{tr} = v_{tr}/v_{\mathcal{D}} - 1 = t_{\mathcal{D}}/t_{tr} - 1\,, \tag{5}$$

where $\mathcal{E}_m$ is the dimensionless strength (mathematical state variable); $\mathcal{V}_{tr}$ is the dimensionless quantity, inverse of the tree inception time (mathematical control parameter).

Taking $\chi = \mathcal{E}_m$ and $\mathcal{A} = -a_t \mathcal{V}_{tr}$, we obtain the equation of fold catastrophe from formula (3)

$$\Phi(\mathcal{E}_m;\ \mathcal{V}_{tr}) = \mathcal{E}_m^3/3 - a_t \mathcal{V}_{tr} \mathcal{E}_m , \tag{6}$$

characterizing the relationship between the maximum local electric field strength and the tree inception time in polymer insulation. Through a_t in the equation (6), we denote a positive scaling factor introduced to better visualize the geometric characteristics of the fold catastrophe function Φ. The minus sign at a_t is taken for the convenience of further analysis of the function Φ.

The analysis of the functions of catastrophes is based on the study of the features of their behavior in the vicinity of critical points when the control parameters change (Gilmore 1993). The profiles $\Phi = f(\mathcal{E}_m)$ of the fold catastrophe function, corresponding to the three characteristic values of the control parameter $\mathcal{V}_{tr}$, are shown in Fig. 1.

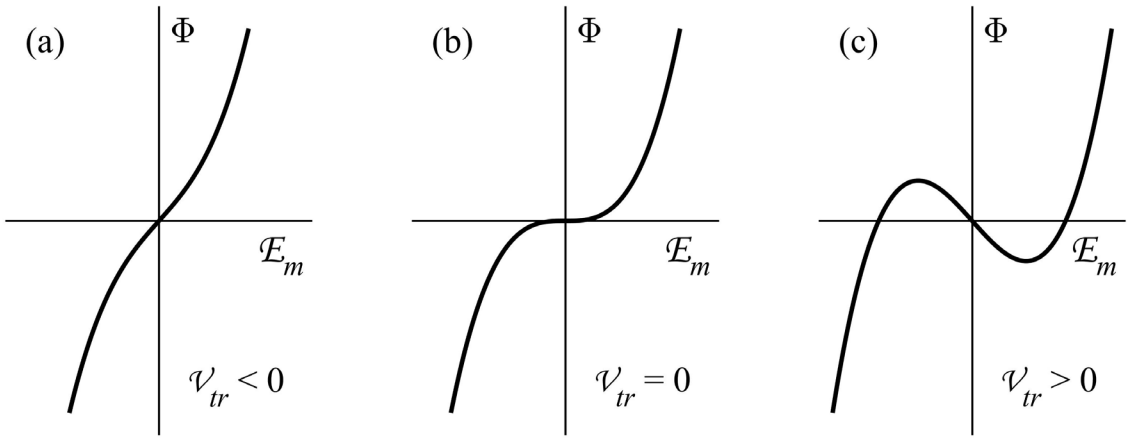

Fig. 1. Fold catastrophe function profiles

The position of the critical points of the function (6) is given by the equations:

$$\partial\Phi/\partial\mathcal{E}_m = \mathcal{E}_m^2 - a_t \mathcal{V}_{tr} = 0; \tag{7}$$

$$\partial^2\Phi/\partial\mathcal{E}_m^2 = 2\mathcal{E}_m = 0. \tag{8}$$

Since $a_t > 0$, when $\mathcal{V}_{tr} < 0$ the equation (7) has no solutions, and therefore, the catastrophe function $\Phi(\mathcal{E}_m;\ \mathcal{V}_{tr})$ has no critical points (Fig. 1a). With $\mathcal{V}_{tr} = 0$, the equation (7) has one root $\mathcal{E}_m = 0$, and the function $\Phi(\mathcal{E}_m;\ \mathcal{V}_{tr})$ has one critical point — the inflection point located at the origin (Fig. 1b). Moreover, due to the fact that equations (7) and (8) are simultaneously fulfilled in the case $\mathcal{V}_{tr} = 0$, this critical point is doubly degenerate. With $\mathcal{V}_{tr} > 0$, the equation (7) has two opposite in sign roots $\mathcal{E}_m = \pm\sqrt{a_t \mathcal{V}_{tr}}$, and the function $\Phi(\mathcal{E}_m;\ \mathcal{V}_{tr})$ has two critical points (Fig. 1c): the minimum point at $\mathcal{E}_m > 0$ and the maximum point at $\mathcal{E}_m < 0$. The minimum point characterizes the stable equilibrium state of the system, realized in practice, and the maximum point is an unstable state that does not take place in reality.

Using the conversion expressions (5), we write the relations that establish a correspondence between the characteristic values of dimensionless mathematical parameters ($\mathcal{E}_m$, $\mathcal{V}_{tr}$) and dimensional physical quantities (E_m, t_{tr}):

$$\begin{aligned} &\mathcal{E}_m < 0 \ \Leftrightarrow\ E_m < E_{\mathcal{D}}; \quad \mathcal{E}_m = 0 \ \Leftrightarrow\ E_m = E_{\mathcal{D}}; \quad \mathcal{E}_m > 0 \ \Leftrightarrow\ E_m > E_{\mathcal{D}}; \\ &\mathcal{V}_{tr} < 0 \ \Leftrightarrow\ t_{tr} > t_{\mathcal{D}}; \quad \mathcal{V}_{tr} = 0 \ \Leftrightarrow\ t_{tr} = t_{\mathcal{D}}; \quad \mathcal{V}_{tr} > 0 \ \Leftrightarrow\ t_{tr} < t_{\mathcal{D}}. \end{aligned} \tag{9}$$

Then, based on the relations (9) and the results of the analysis of equations (6)–(8), we can draw the following conclusions.

 https://www.doi.org/10.33910/2687-153X-2024-5-4-187-194

In the case when an electric field is applied to the dielectric, at which the maximum strength is $E_m < E_\mathcal{D}$, trees in insulation are not observed, since the time of their initiation exceeds the threshold time, i. e., $t_{tr} > t_\mathcal{D}$. With an increase in the voltage applied to the dielectric, the local strength E_m becomes greater than the threshold strength $E_\mathcal{D}$, which leads to the initiation of trees in this dielectric over time $t_{tr} < t_\mathcal{D}$. The equality $t_{tr} = t_\mathcal{D}$ that occurs in the case $E_m = E_\mathcal{D}$ corresponds to the condition of the onset of the catastrophe — the activation of the process of the inception of trees in electrical insulation and the appearance of dependence $t_{tr} = f(E_m)$.

Substituting (5) into (7), we obtain the desired expression of the field dependence of the tree inception time in polymer insulation:

$$t_{tr}(E_m) = t_\mathcal{D} \big/ [1 + a_t^{-1}(E_m / E_\mathcal{D} - 1)^2]. \tag{10}$$

Equation (10) is valid at $E_m \geq E_\mathcal{D}$, i. e., when conditions for the initiation of trees are created in the dielectric. The structure of this equation provides the finiteness of the value of the threshold time $t_\mathcal{D}$, when the minimum electric field strength $E_\mathcal{D}$ is induced in the dielectric. This fact is a strong point of the obtained expression (10).

Discussion of results

The processing of experimental data for polyethylene (Dissado, Hill 1990), cross-linked polyethylene (XLPE) (Hu et al. 2012), and epoxy resin (Sitole, Nyamupangedengu 2020) made it possible to find the parameters a_t, $t_\mathcal{D}$ and $E_\mathcal{D}$ of equation (10). The numerical values of these parameters are summarized in the Table 1, which additionally indicates the values of the threshold strength E_{th}, determined by the authors (Dissado, Hill 1990; Hu et al. 2012; Sitole, Nyamupangedengu 2020) using the equations of type (2).

Table 1. Parameters of the field dependence equation of the inception time of electrical trees in polymer insulation

Insulation	Parameters of the equation (10)			E_{th}, MV/m
	a_t	$t_\mathcal{D}$, s	$E_\mathcal{D}$, MV/m	
Polyethylene	1.289×10^{-4}	5.904×10^{5}	400.7	400
Cross-linked polyethylene (XLPE)	4.957×10^{-4}	3.522×10^{5}	301.4	441
Epoxy resin	1.518×10^{-3}	7.885×10^{4}	149.1	150

The Table 1 shows that for epoxy resin and polyethylene, the values of $E_\mathcal{D}$ and E_{th} agree well, while for cross-linked polyethylene, on the contrary, they diverge greatly. The main reason for the large scatter between $E_\mathcal{D}$ and E_{th} for XLPE seems to be the short duration of the experiment (60 min). A direct argument in favor of such an explanation is the authors' own indication (Hu et al. 2012) of the need to increase the duration of the experiment in order to obtain a more acceptable value of the threshold strength. An indirect argument is the fact that when estimating the $E_\mathcal{D}$ value for polyethylene, which was comparable to E_{th}, an experimental dependence $t_{tr} = f(E_m)$ was used, which was measured (Dissado, Hill 1990) over a substantially longer period of time (~110 h) than a similar dependence for cross-linked polyethylene.

As an example, Fig. 2 illustrates the field dependencies of the inception time of trees in the polymer dielectrics under study. Fig. 2 shows a high degree of correlation between the experimental data (Dissado, Hill 1990; Hu et al. 2012; Sitole, Nyamupangedengu 2020), indicated by symbols, and continuous curves constructed according to equation (10). This confirms the possibility of applying equation (10) to describe the field dependencies $t_{tr} = f(E_m)$ observed in polymer dielectrics.

In conclusion, we consider the main geometric images of the fold catastrophe function, given by equation (6). To do this, using the data (Dissado, Hill 1990), we will build a surface $\Phi = f(\mathcal{E}_m, \mathcal{V}_{tr})$ for polyethylene (Fig. 3).

The surface $\Phi = f(\mathcal{E}_m, \mathcal{V}_{tr})$, shown in Fig. 3, is the result of combining individual curves $\Phi = f(\mathcal{E}_m)$ corresponding to different values of the scaled control parameter $a_t \mathcal{V}_{tr}$. Therefore, it summarizes all the regularities of the change in the fold catastrophe function, resulting from the above analysis of the profiles $\Phi = f(\mathcal{E}_m)$ of this function. So, from Fig. 3, it can be seen that the curves $\Phi = f(\mathcal{E}_m)$ corresponding

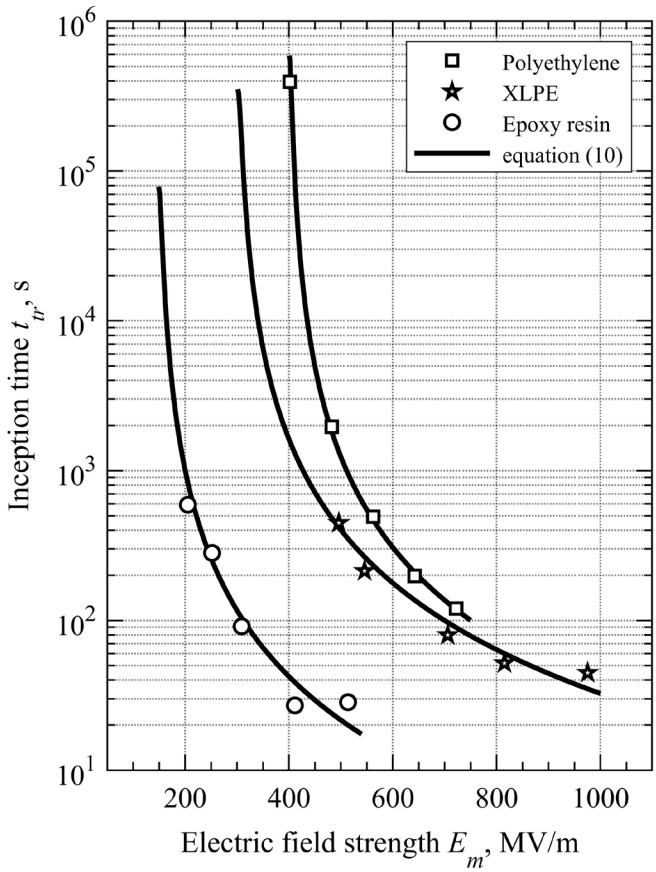

Fig. 2. Field dependencies of the inception time of trees in the polymer dielectrics

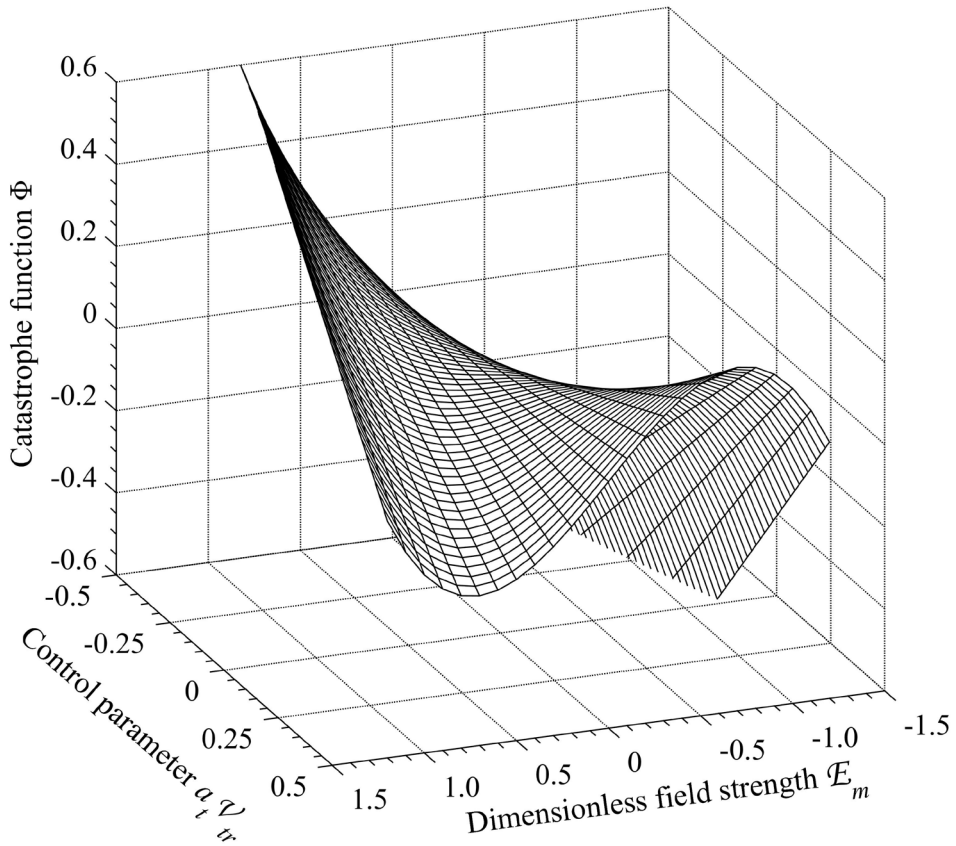

Fig. 3. Fold catastrophe function surface for polyethylene

 https://www.doi.org/10.33910/2687-153X-2024-5-4-187-194

to $\mathcal{V}_{tr} < 0$ and forming the back side of the surface do not have a single critical point. On each of the curves $\Phi = f(\mathcal{E}_m)$ corresponding to $\mathcal{V}_{tr} > 0$ and forming the front side of the surface, there are two critical points: points of minimum (at $\mathcal{E}_m > 0$) and maximum (at $\mathcal{E}_m < 0$). The cross-section of the surface $\Phi = f(\mathcal{E}_m, \mathcal{V}_{tr})$ by the plane $\mathcal{V}_{tr} = 0$, of course, gives a curve $\Phi = f(\mathcal{E}_m)$ with a doubly degenerate critical point at the origin.

The projection of the surface $\Phi = f(\mathcal{E}_m, \mathcal{V}_{tr})$ onto the plane $\Phi\mathcal{E}_m$ is shown in Fig. 4. This projection is a set of curves $\Phi = f(\mathcal{E}_m)$ plotted for dimensionless strength $\mathcal{E}_m \in [0;\ 1.2]$ when the parameter $a_t\mathcal{V}_{tr}$ changes in the range from 0 to 0.5 in increments of 0.025. The upper curve $\Phi = f(\mathcal{E}_m)$ in Fig. 4 corresponds to the case $\mathcal{V}_{tr} = 0$, and the bottom one corresponds to the condition $a_t\mathcal{V}_{tr} = 0.5$. Fig. 4 shows that as the control parameter $\mathcal{V}_{tr}$ increases, the minimum of the function Φ becomes deeper and shifts towards larger values of dimensionless strength $\mathcal{E}_m$. This behavior of the function Φ is consistent with the known nature of the dependence $t_{tr} = f(E_m)$ change, namely, with a decrease in the tree inception time t_{tr} due to an increase in the maximum local strength E_m of the electric field acting on the polymer dielectric.

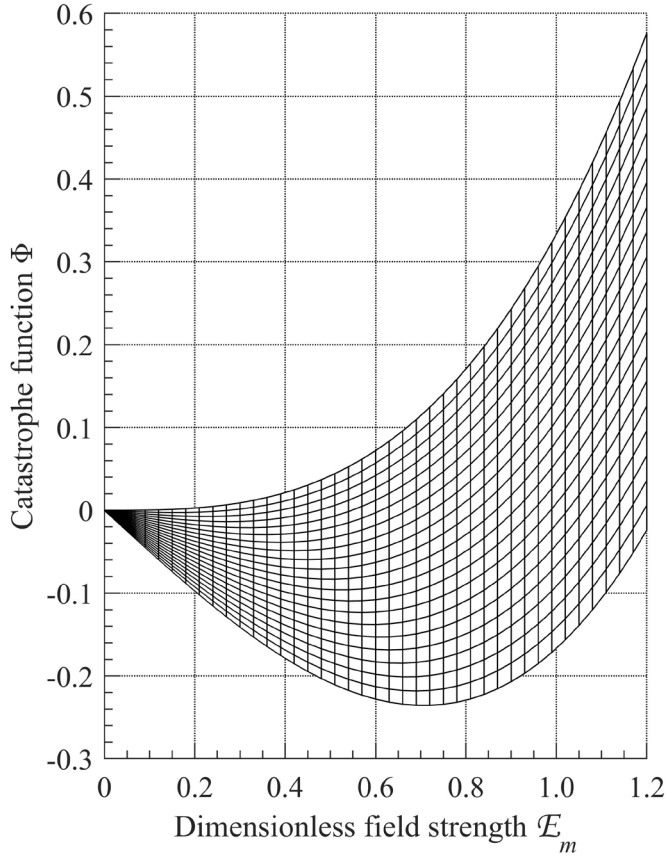

Fig. 4. Fold catastrophe function surface projection for polyethylene

Conclusions

Within the framework of catastrophe theory, the derivation of equation (10) is presented, which makes it possible, at a known maximum local electric field strength, to estimate the tree inception time in polymer insulation. The representation of equation (10) in the form of a time dependence $E_m = f(t_{tr})$ makes it possible to solve the inverse problem quite often encountered in practice — to determine the level of strength that excludes the appearance of trees in the insulation during a given time of its operation.

Field dependencies of the tree inception time are constructed and the threshold parameters of tree initiation in epoxy and polyethylene insulation are estimated. A high degree of correlation between the literature experimental data and field dependencies corresponding to equation (10) is shown. The geometric images of the fold catastrophe function, which reflect the general nature of the change in the inception time of electrical trees in polyethylene, are analyzed.

The results obtained in the article can be used to explain the patterns of tree inception arising from the data of operation and technical tests of polymer dielectrics.

Conflict of Interest

The author declares that there is no conflict of interest, either existing or potential.

References

Blythe, T., Bloor, D. (2005) *Electrical properties of polymers*. 2nd ed. Cambridge: Cambridge University Press, 480 p. (In English)

Borisova, M. E., Kojkov, S. N. (1979) *Fizika dielektrikov [Physics of dielectrics]*. Leningrad: Leningrad University Publ., 240 p. (In Russian)

Borisova, M. E., Marchenko, M. S. (1998) Elektricheskaya prochnost' plenok poliimida [Electric strength of polyimide films]. *Elektrotekhnika*, 5, 4–6. (In Russian)

Cai, Z., Wang, X., Li, L., Hong, W. (2019) Electrical treeing: A phase-field model. *Extreme Mechanics Letters*, 28, 87–95. https://doi.org/10.1016/j.eml.2019.02.006 (In English)

Dissado, L. A., Fothergill, J. C. (1992) *Electrical degradation and breakdown in polymers*. London: Peter Peregrinus Publ., 601 p. (In English)

Dissado, L. A., Hill, R. M. (1990) The statistics of electrical tree inception. *IEEE Transactions on Electrical Insulation*, 25 (4), 660–666. https://doi.org/10.1109/14.57087 (In English)

Dissado, L. A., Dodd, S. J., Champion, J. V. et al. (1997) Propagation of electrical tree structures in solid polymeric insulation. *IEEE Transactions on Dielectrics and Electrical Insulation*, 4 (3), 259–279. https://doi.org/10.1109/94.598282 (In English)

Gilmore, R. (1993) *Catastrophe theory for scientists and engineers*. New York: Dover Publ., 666 p. (In English)

Hu, L., Xu, Y., Chen, X. et al. (2012) The electrical trees initiation at different electric field strength in XLPE cable insulation. In: *Proceedings of the IEEE International symposium on electrical insulation*. San Juan: IEEE Publ., pp. 14–17. https://doi.org/10.1109/ELINSL.2012.6250958 (In English)

Kuchinskij, G. S. (1979) *Chastichnye razryady v vysokovol'tnykh konstruktsiyakh [Partial discharges in high-voltage structures]*. Leningrad: Energiya Publ., 224 p. (In Russian)

Noguchi, S., Nakamichi, M., Oguni, K. (2020) Proposal of finite element analysis method for dielectric breakdown based on Maxwell's equations. *Computer Methods in Applied Mechanics and Engineering*, 371, article 113295. https://doi.org/10.1016/j.cma.2020.113295 (In English)

Sitole, S., Nyamupangedengu, C. (2020) Comparing electrical tree inception in epoxy and polyethylene using Fowler-Nordheim based model. In: B. Németh (ed.). *Proceedings of the 21st International symposium on high voltage engineering. ISH 2019. Lecture notes in electrical engineering. Vol. 599*. Cham: Springer Publ., pp. 1303–1313. https://doi.org/10.1007/978-3-030-31680-8_125 (In English)

Tanaka, T., Greenwood, A. (1978) Effects of charge injection and extraction on tree initiation in polyethylene. *IEEE Transactions on Power Apparatus and Systems*, PAS-97 (5), 1749–1759. https://doi.org/10.1109/TPAS.1978.354668 (In English)

Tumusova, A. N., Kapralova, V. M., Sudar, N. T. (2020) Impulse and DC breakdown strength of polypropylene thin film. *Physics of Complex Systems*, 1 (2), 56–60. https://doi.org/10.33910/2687-153X-2020-1-2-56-60 (In English)

Wang, Q., Deng, Y., Yap, M. et al. (2023) Electrical tree modelling in dielectric polymers using a phase-field regularized cohesive zone model. *Materials & Design*, 235, article 112409. https://doi.org/10.1016/j.matdes.2023.112409 (In English)

Zakrevskii, V. A., Pakhotin, V. A., Sudar', N. T. (2020) Lifetime of polymers in AC electric field. *Technical Physics*, 65 (2), 238–242. https://doi.org/10.1134/S1063784220020255 (In English)

Check for updates

Condensed Matter Physics.
Physics of nanostructures

UDC 539.216:537.226.4

EDN JARMUT
https://www.doi.org/10.33910/2687-153X-2024-5-4-195-201

Electrophysical properties of the Rochelle salt dispersed in a porous dielectric matrix of type A zeolite

T. G. Matveeva [1], M. S. Ivanova [2], V. G. Solovyev ✉[2, 3], A. I. Vanin [2]

[1] Pskov State University Branch in Velikiye Luki, 24 Novoslobodskaya Emb., Velikiye Luki 182100, Russia
[2] Pskov State University, 2 Lenin Square, Pskov 180000, Russia
[3] S. M. Budyonny Military Academy of Telecommunications, 3 Tikhoretskii Ave., Saint Petersburg 194064, Russia

Authors

Tamara G. Matveeva, ORCID: 0009-0009-8382-1667, e-mail: mtg88@yandex.ru

Marina S. Ivanova, ORCID: 0000-0003-1602-4202, e-mail: ivanovams@mail.ru

Vladimir G. Solovyev, ORCID: 0000-0002-8452-6928, e-mail: solovyev_v55@mail.ru

Alexander I. Vanin, ORCID: 0000-0002-6722-4848, e-mail: a.ivanin@mail.ru

For citation: Matveeva, T. G., Ivanova, M. S., Solovyev, V. G., Vanin, A. I. (2024) Electrophysical properties of the Rochelle salt dispersed in a porous dielectric matrix of type A zeolite. *Physics of Complex Systems*, 5 (4), 195–201. https://www.doi.org/10.33910/2687-153X-2024-5-4-195-201 EDN JARMUT

Received 28 August 2024; reviewed 25 September 2024; accepted 25 September 2024.

Funding: The study did not receive any external funding.

Copyright: © T. G. Matveeva, M. S. Ivanova, V. G. Solovyev, A. I. Vanin (2024) Published by Herzen State Pedagogical University of Russia. Open access under CC BY-NC License 4.0.

Abstract. Electrical conductivity, real part of dielectric permittivity and dielectric losses of a novel nanocomposite material obtained by the infiltration of a NaA zeolite matrix with Rochelle salt were studied in the frequency range from 100 Hz to 100 kHz. A low-temperature shift of the Curie point T_C of the guest substance's upper ferroelectric transition due to the influence of confined geometry was observed. It was shown that the kind of temperature dependence of the Rochelle salt's electrical conductivity as well as the character of the dielectric losses' frequency dependence change significantly when this ferroelectric is dispersed in the NaA zeolite.

Keywords: ferroelectrics, Rochelle salt, permittivity, dielectric losses, electrical conductivity, zeolite, nanocomposite

Introduction

The idea of using zeolites for fabricating three-dimensional superlattices from nanoparticles within the regular systems of calibrated voids and channels of these nanoporous dielectric matrices was proposed at the end of the twentieth century (Bogomolov 1978; Stucky, Mac Dougall 1990). The most promising application of zeolites is their use in the creation of quantum confined nanocomposite materials in order to study size effects.

A theoretical explanation of the T_C value shift towards lower temperatures (Zhong et al. 1994) is based on Landau phenomenological theory. A confined geometry effect has been frequently observed in experiments with small ferroelectric particles in porous matrices (Cizman et al. 2013; Matveeva, Solovyev 2022; Pan'kova et al. 1996; Tien et al. 2008). However, in some cases (Baryshnikov et al. 2011; Rogazinskaya et al. 2009) a T_C value shift towards higher temperatures is also possible in systems of ferroelectric nanoparticles in porous matrices, compared with the temperature of the phase transition in a bulk substance.

The aim of this study was to determine experimentally the electrophysical properties of the well-researched ferroelectric (Gurevich 1969; Malyshkina, Gavrilova 2002; Mitani et al. 1974; Singaravadivelu et al. 2019; Zhou et al. 2008), i. e. Rochelle salt ($KNaC_4H_4O_6 \times 4H_2O$, hereinafter referred to as RS) embedded into a NaA-type zeolite matrix near the upper ferroelectric Curie point (T_C = 297 K for the bulk material). NaA zeolite is a porous dielectric matrix which contains an ordered system of interconnected cavities and three-dimensional channels with diameters of ~ 1 nm (Breck 1974). The Rochelle salt's cell parameters $a \approx 1.2$ nm, $b \approx 1.4$ nm, $c \approx 0.6$ nm (Solans et al. 1997) are rather large; thus, we suppose that RS molecules can be located only in α-cavities along <100> directions of the NaA crystal.

Experimental methods

We used granules (spheres with a diameter of 2 mm) of the NaA zeolite as a porous dielectric matrix. The Rochelle salt was embedded into zeolite cavities from a saturated aqueous solution at room temperature; the ferroelectric/zeolite nanocomposite sample was then washed with distilled water. Then it was dried at T = 300 K, and the procedure was repeated once more to increase the pore filling factor. To remove the 'guest' substance from the surface of the sample, it was subjected to mechanical processing (surface grinding) and given the shape of a tablet with a diameter of 2 mm and a thickness of 0.5 mm. After applying graphite contacts to the surface of the sample, it was clamped between the metal electrodes of the measuring cell. For control, similar measurements were also carried out on a bulk Rochelle salt single crystal with its ***c*** — axis parallel to the applied electric field, as well as on the polycrystalline zeolite host matrix.

The temperature dependences of the nanocomposite electrophysical characteristics (electric conductivity σ, dielectric permittivity ε` and dielectric losses *tg*δ) were studied using a high-precision bridge (RLC-meter MS5308) at frequencies of 100 Hz, 120 Hz, 1 kHz, 10 kHz and 100 kHz by the method of two parallel conductors (copper plates between which our nanocomposite was placed). The error bars did not exceed 5%. The temperature was measured on one of the electrodes using a two-channel thermometer GM1312 (instrument accuracy 0.1 K).

Results and discussion

The temperature dependences of ε` for the bulk RS (curve 1) and for the ferroelectric / zeolite nanocomposite (curve 2)) are presented in Fig. 1.

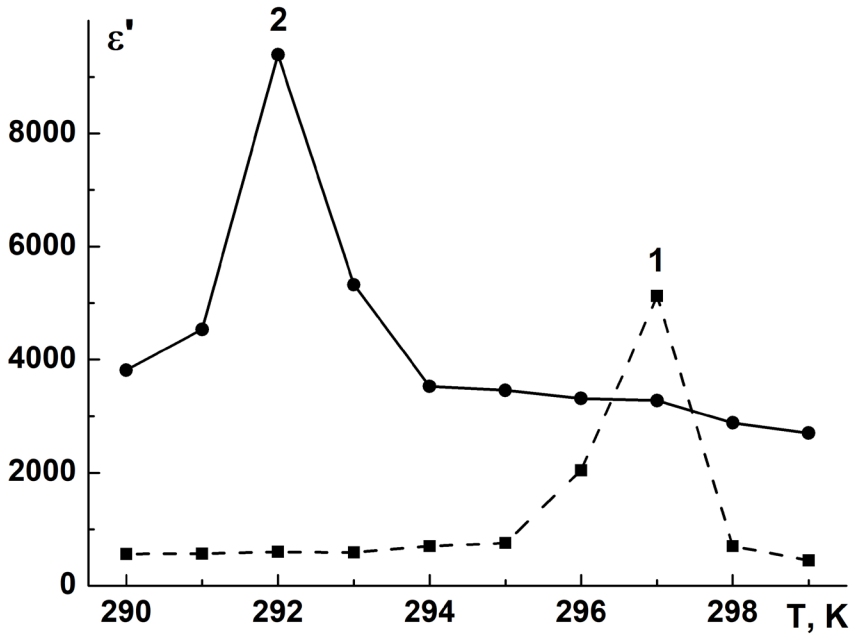

Fig. 1. Temperature dependences of the dielectric permittivity for the bulk RS (curve 1) and for the ferroelectric / zeolite nanocomposite (curve 2) at 120 Hz

 https://www.doi.org/10.33910/2687-153X-2024-5-4-195-201

It is easy to see that due to the confined geometry there is a significant shift of T_C ($\Delta T \approx 5K$) towards lower temperatures.

It should be noted that the initial zeolite matrix has a much smaller ε` value (ε`≈ 200 at 120 Hz) without any observable temperature dependence in the studied temperature range.

The temperature dependence of the reference sample's (a bulk RS crystal) electrical conductivity at 1 kHz (Fig. 2) is qualitatively consistent with the previously published results (Gurevich 1969).

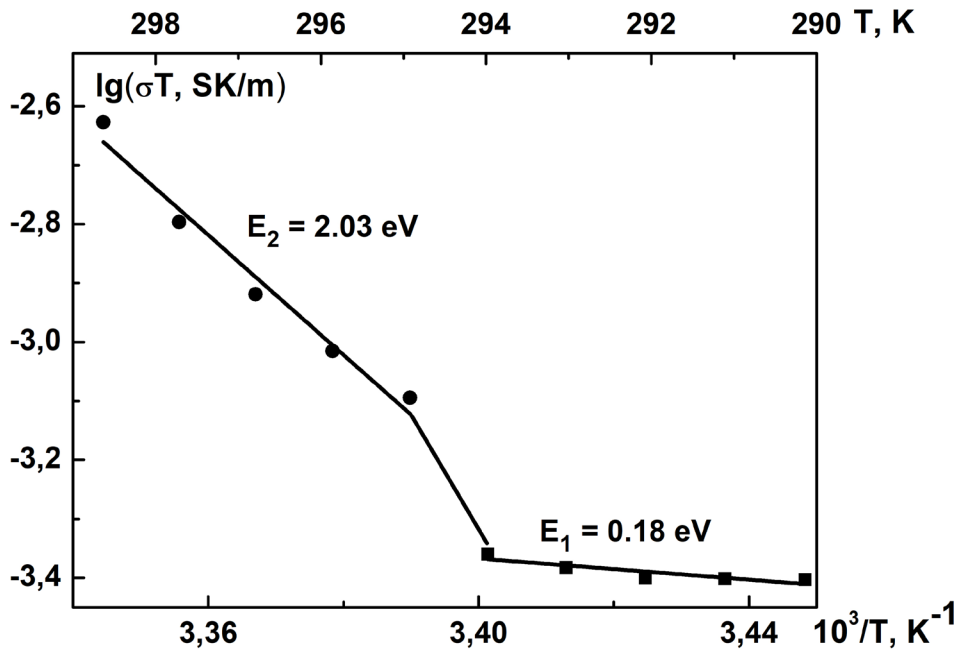

Fig. 2. Temperature dependence of the electrical conductivity for the bulk RS at 1 kHz

As one can see from the graph, there are two sections on the Arrhenius temperature dependence of conductivity with different activation energies: E_1 = (0.18 ± 0.05) eV at temperatures below T_C and E_2 = (2.03 ± 0.19) eV at temperatures above T_C.

Such an abrupt change in the activation energy of carriers in the case of impurity electronic electrical conductivity of the ferroelectric may be due to a significant difference in the electronic components of the permittivity of para- and ferroelectric phases (Gurevich 1969). At the same time, it is noted in the literature (Ovchinnikova et al. 1997) that the electrical conductivity of the RS can be largely associated with proton transport.

Arrhenius temperature dependence of the ferroelectric / zeolite sample's electrical conductivity (Fig. 3) also has two sections with different activation energy values. However, in this case, the value of the activation energy in the ferroelectric phase E_3 = (1.14 ± 0.08) eV is higher than the value of the activation energy in the paraelectric phase E_4 = (0.49 ± 0.08) eV. At the same time, specific conductivity of the composite significantly exceeds the corresponding value for a bulk ferroelectric. It was pointed out (Gurevich 1969) that the processes of hydration and dehydration have a noticeable effect on the electrophysical properties of $KNaC_4H_4O_6 \times 4H_2O$ crystals. For an ultradispersed ferroelectric, when its nanoparticles with a developed surface intensively interact with zeolite water in the pores of the matrix, this effect can be even more significant.

The frequency dependences of *tg*δ for the bulk RS (Fig. 4) as well as for the initial zeolite matrix (Fig. 5) display a smooth decrease in the value of *tg*δ with increasing frequency *f* without any maxima in the studied frequency range which is typical for many dielectrics (Woodward 2021).

On the other hand, the frequency dependences $tg\delta = F(f)$ for the ferroelectric / zeolite sample (Fig. 6) have clearly expressed maxima at frequencies of ~10 kHz in the ferroelectric phase and ~1 kHz in the paraelectric phase (above the upper Curie point $T_C \approx 292$ K for the nanocomposite). These results can be interpreted within the framework of Debye theory taking into account the relaxation processes in a heterogeneous nanocomposite ferroelectric / zeolite, which has a sufficiently high ionic conductivity and a significant difference in the static (low-frequency) and high-frequency permittivity values:

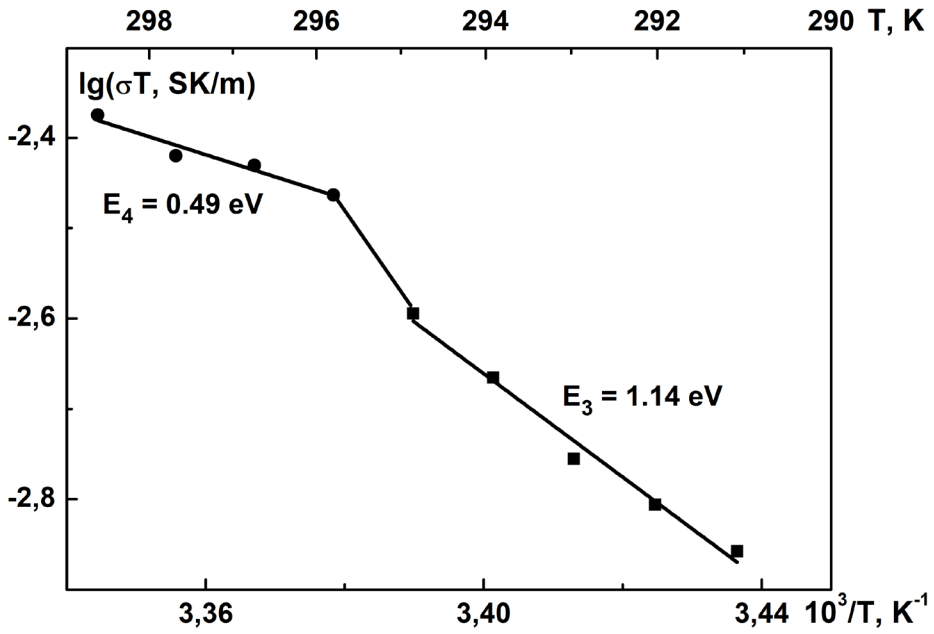

Fig. 3. Temperature dependence of the electrical conductivity for the ferroelectric / zeolite nanocomposite at 1 kHz

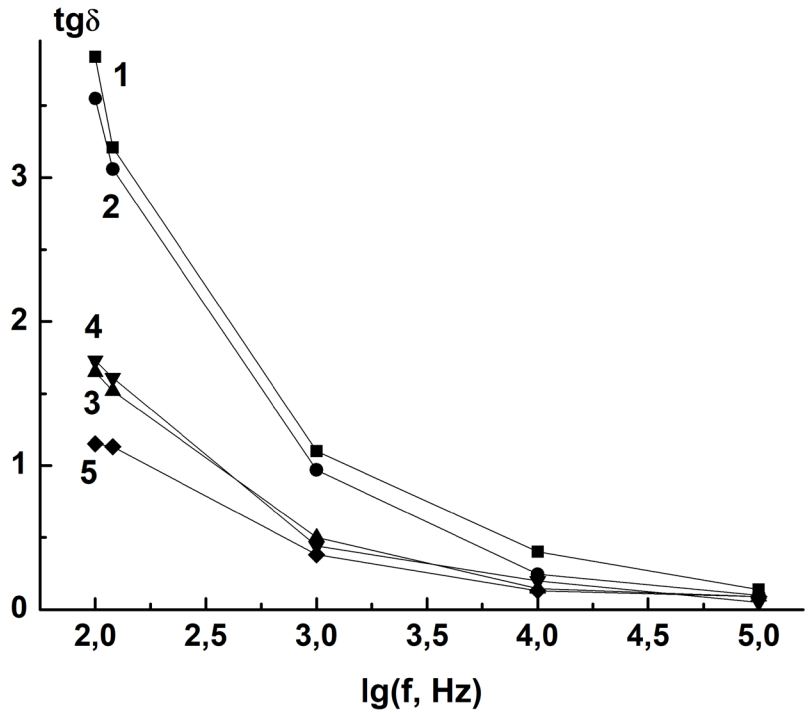

Fig. 4. Frequency dependences of *tg*δ for the bulk RS at 290 K (curve 1), 292 K (curve 2), 294 K (curve 3), 296 K (curve 4) and 298 K (curve 5)

https://www.doi.org/10.33910/2687-153X-2024-5-4-195-201

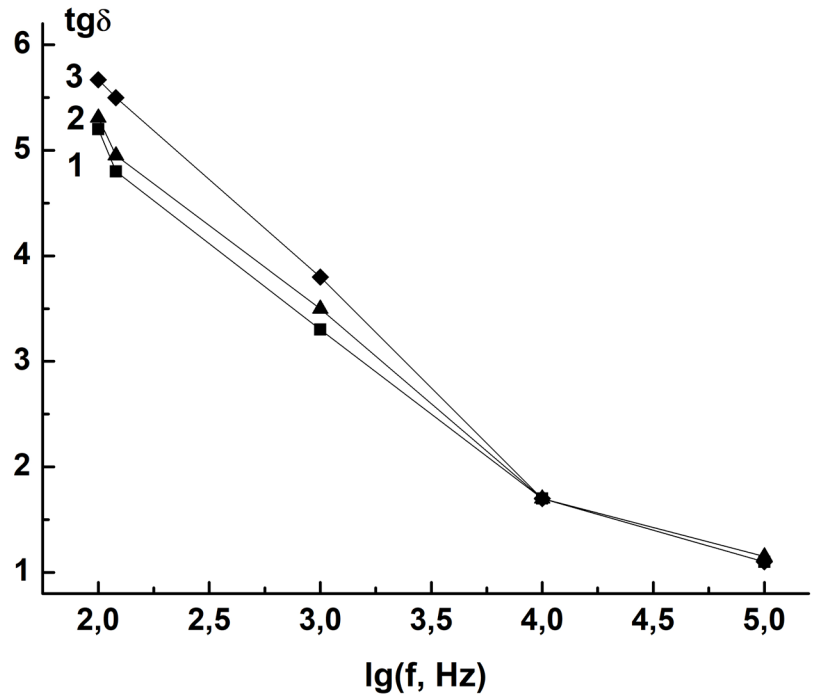

Fig. 5. Frequency dependences of *tg*δ for the zeolite NaA at 290 K (curve 1), 294 K (curve 2) and 298 K (curve 3)

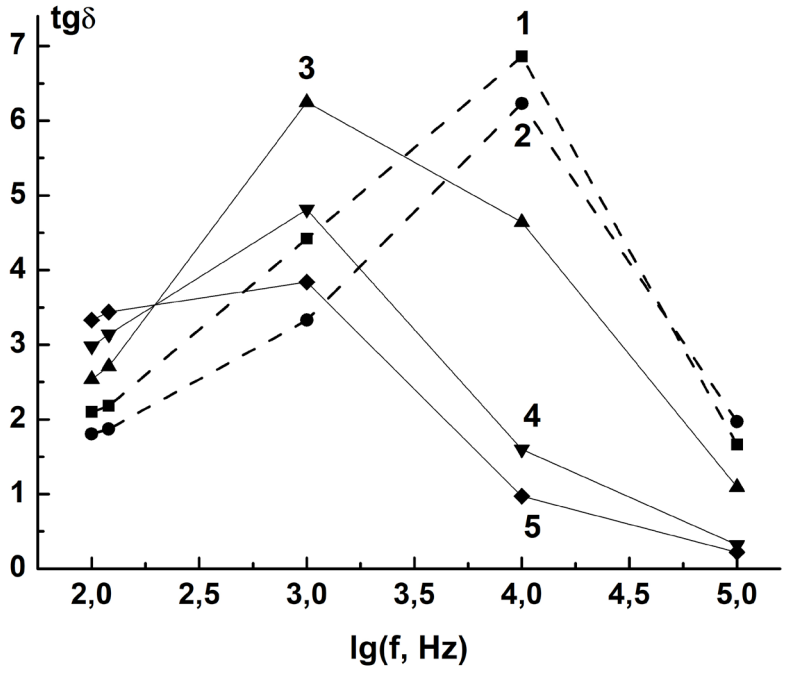

Fig. 6. Frequency dependences of *tg*δ for the ferroelectric / zeolite nanocomposite at 290 K (curve 1), 292 K (curve 2), 294 K (curve 3), 296 K (curve 4) and 298 K (curve 5)

$\Delta\varepsilon = (\varepsilon_{st} - \varepsilon_{\infty}) > 8\varepsilon_{\infty}$ (Bogatin et al. 2002; Bogatin 2012). It should be emphasized that the components of the nanocomposite differ significantly in electrical characteristics, which makes the development of interlayer polarization possible.

It is pointed out in literature (Steeman, van Turnhout 2003) that conductivity differences in the phases of an inhomogeneous medium give rise to interfacial polarization — the build-up of space charges near the interfaces between various phases. Such a polarization usually occurs at frequencies lower than the time scales typical of dipolar polarizations. Moreover, the contribution of interfacial polarization to the dielectric properties of a material is often much larger than dipolar contributions.

Conclusions

The novel nanocomposite ferroelectric / zeolite material obtained by the infiltration of a NaA zeolite host matrix with a Rochelle salt guest substance demonstrates a shift of the Rochelle salt's upper ferroelectric transition Curie point T_C by ~ 5 K towards lower temperatures, compared with the temperature of the phase transition in a bulk ferroelectric.

The character of the temperature dependence of the Rochelle salt's electrical conductivity (namely, the sequence of sections with high and low activation energies) changes significantly when it is dispersed in the NaA zeolite matrix, which is probably due to the influence of water molecules.

On heating through T_C, the position of a maximum on the $tg\delta$ frequency dependence of the ferroelectric / zeolite nanocomposite shifts towards lower frequencies. A possible interpretation of this effect has been given within the framework of Debye theory, taking into account the electrical conductivity of the heterogeneous nanocomposite consisting of components with different electrical characteristics, which makes the development of interlayer polarization possible.

Conflict of Interest

The authors declare that there is no conflict of interest, either existing or potential.

Author Contributions

All the authors discussed the final work and took part in writing the article.

References

Baryshnikov, S. V., Charnaya, E. V., Shatskaya, Yu. A. et al. (2011) Effect of confined geometry on linear and nonlinear dielectric properties of triglycine sulfate near the phase transition. *Physics of the Solid State*, 53 (6), 1212–1215. https://doi.org/10.1134/S1063783411060059 (In English)

Bogatin, A. S. (2012) Relaxation polarizations: Strong and weak processes. *Physics of the Solid State*, 54 (1), 62–69. https://doi.org/10.1134/S1063783412010064 (In English)

Bogatin, A. S., Lisitsa, I. V., Bogatina, S. A. (2002) The effect of percolation conductivity on the characteristics of relaxation polarization processes. *Technical Physics Letters*, 28 (9), 779–781. https://doi.org/10.1134/1.1511783 (In English)

Bogomolov, V. N. (1978) Liquids in ultrathin channels (Filament and cluster crystals). *Soviet Physics Uspekhi*, 21 (1), 77–83. https://doi.org/10.1070/PU1978v021n01ABEH005510 (In English)

Breck, D. W. (1974) *Zeolite molecular sieves: Structure, chemistry and use*. New York: Wiley Publ., 771 p. (In English)

Cizman, A., Antropova, T., Anfimova, I. et al. (2013) Size-driven ferroelectric–paraelectric phase transition in TGS nanocomposites. *Journal of Nanoparticle Research*, 15 (8), article 1807. https://doi.org/10.1007/s11051-013-1807-y (In English)

Gurevich, V. M. (1969) *Elektroprovodnost' segnetoelektrikov [Electrical conductivity of ferroelectrics]*. Moscow: The Committee on Standards, Measures, and Measuring Instruments of the Council of Ministers of the USSR Publ., 384 p. (In Russian)

Malyshkina, I. A., Gavrilova, N. D. (2002) Low-frequency dielectric properties of the Rochelle salt and its deuterated analogue. *Ferroelectrics*, 268 (1), 41–46. http://doi.org/10.1080/00150190211066 (In English)

Matveeva, T. G., Solovyev, V. G. (2022) Dielektricheskie svojstva nanochastits segnetovoj soli v matritse tseolita NaA [Dielectric properties of the Rochelle salt nanoparticles in the NaA zeolite matrix]. *Tekhnika radiosvyazi — Radio Communication Technology*, 4 (55), 118–124. (In Russian)

Mitani, S., Fukui, S., Shibuya, I. et al. (1974) Crystal structure refinement of ferroelectric Rochelle salt. *Ferroelectrics*, 8 (1), 477–478. http://dx.doi.org/10.1080/00150197408234131 (In English)

Ovchinnikova, G. I., Gavrilova, N. D., Lotonov, A. N. et al. (1997) Ion transport as manifested in microwave spectra and static conduction of seignette salt crystals. *Bulletin of the Russian Academy of Sciences: Physics*, 61 (12), 1913–1917. (In English)

Pan'kova, S. V., Poborchii, V. V., Solov'ev, V. G. (1996) The giant dielectric constant of opal containing sodium nitrate nanoparticles. *Journal of Physics: Condensed Matter*, 8 (12), L203–L206. https://doi.org/10.1088/0953-8984/8/12/001 (In English)

Rogazinskaya, O. V., Milovidova, S. D., Sidorkin, A. S. et al. (2009) Properties of nanoporous aluminum oxide with triglycine sulfate and Rochelle salt inclusions. *Physics of the Solid State*, 51 (7), 1518–1520. https://doi.org/10.1134/S1063783409070506 (In English)

Singaravadivelu, S., Uthayakumar, A., Balaji Bhargav, P. (2019) Study of the relative growth rate, the anisotropy of electrical resistivity and anomalous photocurrent behavior of the unidirectional grown Rochelle salt crystals. *Ferroelectrics*, 550 (1), 112–126. https://doi.org/10.1080/00150193.2019.1652501 (In English)

Solans, X., Gonzalez-Silgo, C., Ruiz-Pérez, C. (1997) A structural study on the Rochelle salt. *Journal of Solid State Chemistry*, 131 (2), 350–357. (In English)

Steeman, P. A. M., van Turnhout, J. (2003) Dielectric properties of inhomogeneous media. In: F. Kremer, A. Schönhals (eds.). *Broadband dielectric spectroscopy*. Berlin; Heidelberg: Springer Publ., pp. 495–522. https://doi.org/10.1007/978-3-642-56120-7 (In English)

Stucky, G. D., Mac Dougall, J. E. (1990) Quantum confinement and host/guest chemistry: Probing a new dimension. *Science*, 247 (4943), 669–678. https://doi.org/10.1126/science.247.4943.669 (In English)

Tien, C., Charnaya, E. V., Lee, M. K. et al. (2008) NMR studies of structure and ferroelectricity for Rochelle salt nanoparticles embedded in mesoporous sieves. *Journal of Physics: Condensed Matter*, 20 (21), article 215205. https://doi.org/10.1088/0953-8984/20/21/215205 (In English)

Woodward, W. H. H. (2021) Broadband dielectric spectroscopy — A practical guide. In: *Broadband dielectric spectroscopy: A modern analytical technique. ACS symposium series. Vol. 1375*. Washington: American Chemical Society Publ., pp. 3–59. https://pubs.acs.org/doi/10.1021/bk-2021-1375# (In English)

Zhong, W. L., Wang, Y. G., Zhang, P. L., Qu, B. D. (1994) Phenomenological study of the size effect on phase transitions in ferroelectric particles. *Physical Review. B*, 50 (2), 698–703. https://doi.org/10.1103/PhysRevB.50.698 (In English)

Zhou, G., Wu, J., Wang, A. et al. (2008) Investigation of ferroelectric phase transition of Rochelle salt. *Ferroelectrics*, 366 (1), 67–73. http://dx.doi.org/10.1080/00150190802363173 (In English)

Check for updates

Condensed Matter Physics. Dielectrics

UDC 544.7

EDN WNDCIU
https://www.doi.org/10.33910/2687-153X-2024-5-4-202-204

Electret properties and wettability of polymer materials treated by DC glow discharge

M. Yu. Yablokov ✉[1], A. A. Kuznetsov[1]

[1] Enikolopov Institute of Synthetic Polymeric Materials, Russian Academy of Sciences, 70 Profsoyuznaya Str., Moscow 117393, Russia

Authors

Mikhail Yu. Yablokov, ORCID: 0000-0003-4572-8989, e-mail: yabl1@yandex.ru

Alexander A. Kuznetsov, ORCID: 0000-0001-7527-2869, e-mail: kuznets24@yandex.ru

For citation: Yablokov, M. Yu., Kuznetsov, A. A. (2024) Electret properties and wettability of polymer materials treated by DC glow discharge. *Physics of Complex Systems*, 5 (4), 202–204. https://www.doi.org/10.33910/2687-153X-2024-5-4-202-204 EDN WNDCIU

Received 23 September 2024; reviewed 11 October 2024; accepted 11 October 2024.

Funding: The work was financially supported by the Ministry of Science and Higher Education of the Russian Federation, Contract FFSM-2024-0002.

Copyright: © M. Yu. Yablokov, A. A. Kuznetsov (2024) Published by Herzen State Pedagogical University of Russia. Open access under CC BY-NC License 4.0.

Abstract. We studied the influence of electret charge on the hydrophilicity of polytetrafluoroethylene (PTFE) films treated by direct-current (DC) glow discharge. DC discharge treatment of polymers leads to significant hydrophilization and appearance of surface charges on initially hydrophobic polymer surfaces. It was shown that the storage of plasma-treated PTFE films in environments with different relative humidity leads to an increased water contact angle along with a decreased surface potential. The process of hydrophobic recovery of plasma-treated PTFE films is considered as a consequence of charge relaxation in a humid atmosphere. It was established that surface charging of plasma-treated polymers makes a significant contribution to their hydrophilicity.

Keywords: direct-current glow discharge, plasma treatment, wettability, polymer electrets, hydrophobic recovery

Introduction

Surface modification by low-temperature plasma is a very efficient tool for a significant improvement of surface properties of polymer materials. It is known that plasma treatment results in a considerable change in the chemical composition of the surface caused by chemical reactions leading to an increase in oxygen-containing groups (Cvelbar et al. 2019). Hydrophobic polymer surfaces become hydrophilic after plasma treatment; however, this hydrophilicity is partially lost with time. This process is called 'hydrophobic recovery' (Primc, Mozetič 2022). The nature of this process is not yet understood. Hydrophilicity of plasma-treated polymer surfaces is usually interpreted as a result of the increase in the content of oxygen-containing polar groups on the surface. We consider this interpretation too simplified as it does not take into account the charging of polymers during their plasma treatment. Earlier, we observed correlations between surface charging, wettability and adhesion properties of PTFE films treated by direct-current (DC) glow discharge (Yablokov et al. 2015). Electret charges were measured after the corona discharge treatment of fluorocarbon polymers, and the role of high humidity in surface charge relaxation was underlined (Shuvayev et al. 1977).

The aim of the present work is to study the influence of electret charges arising in PTFE films treated by DC glow discharge on the hydrophilicity of these films.

Materials and methods

PTFE film samples with a thickness of 40 μm ('Plastpolymer', Saint Petersburg, Russia) were used in this study. The procedure for film modification by DC glow discharge is outlined in detail in (Rychkov et al. 2012). Polymer samples were placed on the bottom electrode of a two-electrode system (anode or cathode) and treated in the air as a working plasma gas, at a pressure of 10–15 Pa and a discharge current of 50 mA for 30 s. Electret measurements were performed using Ultra Stable Surface DC Voltmeter Model USSVM2 (AlphaLab, Inc.). Surface properties were characterized by the contact angle values measured with an Easy Drop DSA100 instrument (KRUSS) using distilled water as a test liquid. Plasma treated samples were stored in plastic boxes at room temperature in the air with different relative humidity (RH). Different RH of air was obtained above saturated aqueous solutions of salts. Air with RH = 75% was obtained over the saturated aqueous solution of NaCl. Air with RH ≤ 1% was obtained in a plastic box with a desiccant.

Results

The water contact angle (WCA) and the electret properties of DC glow-discharge-treated PTFE films were measured simultaneously. After treatment, polymer films were stored at different relative humidity at room temperature. The experimental data on changes in the contact angle by water (θ) with time for polymer films treated at the anode and at the cathode are shown in Fig. 1. The surface potential of PTFE films treated at the anode and at the cathode is shown in Fig. 2. The decay curves are normalized by the value measured just after the plasma treatment. The highest hydrophilicity (the lowest WCA value) can be seen (Fig. 1) in the film treated at the anode. The film treated at the cathode has the lowest hydrophilicity (highest WCA). A significant difference is observed for the hydrophobic recovery of films stored in dry (RH ≤ 1%) and humid (RH = 75%) atmosphere. Hydrophobic recovery, or increase of the WCA of films stored in humid atmosphere, is larger. This difference is observed both for films treated at the anode and at the cathode. Storage in humid atmosphere leads to a significant decrease in the normalized surface potential. This result corresponds to the well-known effect of the influence of ambient air humidity on the stability of the electret charge. Slower relaxation of the normalized surface potential is observed for the films treated at the anode (electrons and negative ions are active agents during plasma treatment) compared to the treatment at the cathode.

Surface potential decay of the polymer film in humid atmosphere is the result of the increased surface conductivity (Shuvayev et al. 1977). Electret charges on the polymer surface attract polar water molecules, thus increasing water droplet–surface interaction during WCA measurement.

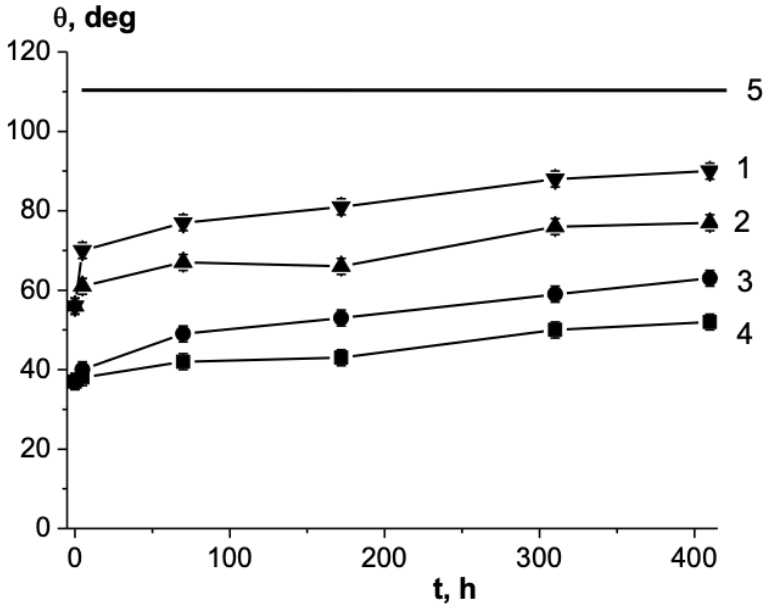

Fig. 1. Water contact angle temporal evolution of direct-current glow-discharge-treated PTFE films, stored at different relative humidity: 1 — film treated at the cathode, stored at RH = 75%; 2 — film treated at the cathode, stored in dry (less than RH = 1%) atmosphere; 3 — film treated at the anode, stored at RH = 75%; 4 — film treated at the anode, stored in dry (less than RH = 1%) atmosphere; 5 — contact angle of the pristine PTFE film

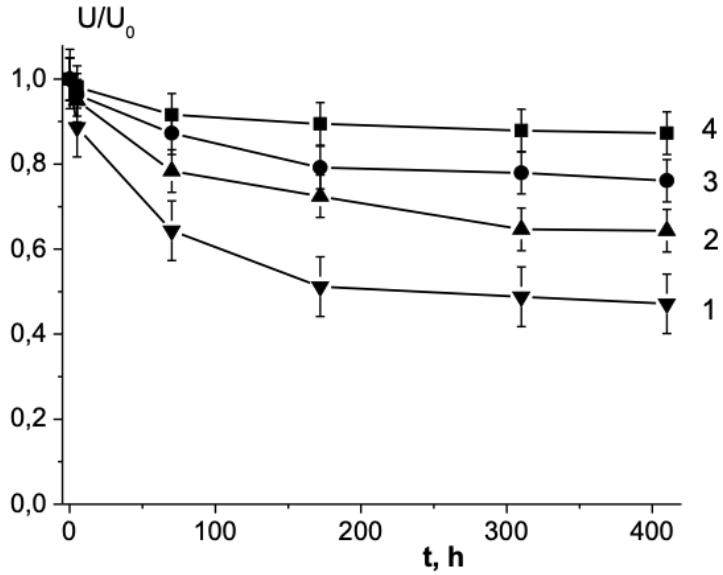

Fig. 2. Normalized surface-potential decay of direct-current glow-discharge — treated PTFE films, stored at different relative humidity: 1 — film treated at the cathode, stored at RH = 75%; 2 — film treated at the cathode, stored in dry (less than RH = 1%) atmosphere; 3 — film treated at the anode, stored at RH = 75%; 4 — film treated at the anode, stored in dry (less than RH = 1%) atmosphere

Conclusions

The results of the study of wettability degradation and charge relaxation of PTFE films after treatment by direct-current glow discharge are presented here. The water contact angle was shown to increase during the storage of polymers at room temperature in environments with different relative humidity. It was also demonstrated that surface potential decreases in time in humid atmosphere faster than in dry air. Hydrophobic recovery of plasma-treated polymer films may be considered as a consequence of electret charge relaxation. It means that surface charging in the process of plasma treatment contributes to the effect of polymer surface hydrophilicity improvement.

Conflict of Interest

The authors declare that there is no conflict of interest, either existing or potential.

Author Contributions

All the authors discussed the final work and took part in writing the article.

References

Cvelbar, U., Walsh, J. L., Černák, M. et al. (2019) White paper on the future of plasma science and technology in plastics and textiles. *Plasma Processes and Polymers*, 16 (1), article 1700228. https://doi.org/10.1002/ppap.201700228 (In English)

Primc, G., Mozetič, M. (2022) Hydrophobic recovery of plasma-hydrophilized polyethylene terephthalate polymers. *Polymers*, 14 (12), article 2496. https://doi.org/10.3390/polym14122496 (In English)

Rychkov, D., Yablokov, M., Rychkov, A. (2012) Chemical and physical surface modification of PTFE films—an approach to produce stable electrets. *Applied Physics A*, 107 (3), 589–596. https://doi.org/10.1007/s00339-012-6834-5 (In English)

Shuvayev, V. P., Turyshev, B. I., Romanovskaya, O. S. et al. (1977) On the mechanism of electret charge relaxation under conditions of high humidity. *Polymer Science U.S.S.R.*, 19 (3), 698–703. https://doi.org/10.1016/0032-3950(77)90129-0 (In English)

Yablokov, M. Yu., Piskarev, M. S., Gilman, A. B. et al. (2015) Interrelation between adhesive, contact, and electret properties of DC discharge-modified polytetrafluoroethylene films. *High Energy Chemistry*, 49, 207–210. https://doi.org/10.1134/S0018143915030170 (In English)

Check for updates

Physics of Semiconductors.
Physics of thin films

UDC 538.9

EDN THHPQB
https://www.doi.org/10.33910/2687-153X-2024-5-4-205-214

The formation of $MoTe_2$ nanofilms on metal substrates

P. N. Yakushev [1], V. A. Bershtein [1], A. V. Kolobov [2] ✉

[1] Ioffe Institute, 26 Polytechnicheskaya Str., Saint Petersburg 194021, Russia
[2] Herzen State Pedagogical University of Russia, 48 Moika Emb., Saint Petersburg 191186, Russia

Authors
Pavel N. Yakushev, ORCID: 0000-0002-9947-1245, e-mail: yak@pav.ioffe.ru
Vladimir A. Bershtein, ORCID: 0000-0003-4524-8766, e-mail: vbersht.polmater@mail.ioffe.ru
Alexandr V. Kolobov, ORCID: 0000-0002-8125-1172, e-mail: akolobov@herzen.spb.ru

For citation: Yakushev, P. N., Bershtein, V. A., Kolobov, A. V. (2024) The formation of $MoTe_2$ nanofilms on metal substrates. *Physics of Complex Systems*, 5 (4), 205–214. https://www.doi.org/10.33910/2687-153X-2024-5-4-205-214 EDN THHPQB

Received 22 September 2024; reviewed 28 September 2024; accepted 09 October 2024.

Funding: This work was partially supported by the Russian Science Foundation (grant 22-19-00766).

Copyright: © P. N. Yakushev, V. A. Bershtein, A. V. Kolobov (2024) Published by Herzen State Pedagogical University of Russia. Open access under CC BY-NC License 4.0.

Abstract. Transition-metal dichalcogenides are among most studied two-dimensional semiconductors for applications in electronics, optoelectronics, spintronics, and memory devices. One of the simple commercially friendly methods to fabricate thin crystalline films is solid-state crystallization from the amorphous phase. In this work, using differential scanning calorimetry (DSC) measurements, we demonstrate that $MoTe_2$ nanolayers deposited on different substrates (Ta, Al, W, Mo) manifest distinctly different crystallization behavior. We argue that these differences are associated with different chemical affinity of the film constituents towards the substrate material and propose a scheme of this complex crystallization process.

Keywords: transition-metal dichalcogenides, solid-state crystallization, differential scanning calorimetry, nanofilms, two-dimensional semiconductors

Introduction

The success of graphene has triggered an intensive search for other two-dimensional (2D) materials, especially 2D semiconductors. One of the promising classes of such materials is transition-metal dichalcogenides (TMDCs) (Kolobov, Tominaga 2016) with the generic formula MX_2 (M = Mo, W, X = S, Se, Te). These materials possess a layered structure, where M-X-M sandwiches, often called monolayers, are held together by weak van der Waals forces. The interest in these materials was reignited about ten years ago when it was found that the electronic structure of MoS_2 changed from indirect in the bulk form to a direct gap in the monolayer limit (Mak et al. 2010), which makes TMDCs an important class of optoelectronic materials. Unique properties of 2D TMDCs were reported. Among them are extremely large exciton binding energies (Chernikov et al. 2014), spin-valley coupling (Xiao et al. 2012), etc. Numerous and various devices based on few-layer and monolayer TMDCs have been demonstrated, ranging from various electronics (Cho et al. 2015; Lin et al. 2014; Sarkar et al. 2015), optoelectronics (Yin et al. 2016), and spintronics (Suzuki et al. 2014) applications to biomedical uses (Liu, Liu 2018).

An additional benefit of using monolayer thick semiconductors as active layers in devices is their ultra-low power consumption (Tang et al. 2023). The sub-nanometer thickness of such layers also enables the use of few monolayer TMDC in transparent and flexible electronics (Li et al. 2020). Monolayer-thick 2D materials are usually very strong mechanically, which opens the possibility to further control their electronic structure and properties through the application of strain (straintronics) (Wei et al. 2017).

While most 2D transition-metal dichalcogenides (TMDCs) possess only one single phase stable at room temperature, 2D $MoTe_2$ exhibits intriguing polymorphism: the semi- conducting 2H phase and the metallic 1T' phase. In the semiconducting 2H phase, the Mo and Te atoms are arranged in in-plane hexagonal symmetry and out-of-plane trigonal prismatic coordination with a space group of *P*6*m*2. In the metallic 1T' phase, they are arranged in in-plane monoclinic symmetry and out-of-plane octahedral coordination with a space group of $P12_1/m1$ (Huang et al. 2016). A remarkable feature of this material is that the energy barrier between the two states is rather low (Duerloo 2014), which enables an easy transition between these states. The transition can be driven thermally or, alternatively, stimulated by supplying external energy by means of strain (Song et al. 2016) or electronic excitation (Cho et al. 2015; Kolobov et al. 2016; Li et al. 2016).

Bulk $MoTe_2$ can be directly synthesized in either a semiconducting 2H or a metallic 1T' phase (Park et al. 2015; Yoo et al. 2017; Zhou et al. 2015), while both phases are stable at temperatures up to 815 °C and 900 °C, respectively (Ueno, Fukushima 2015). The fabrication methods for monolayer thick structures can be classified into two broad categories, namely, top-down methods and bottom-up methods. In the top-down approach, nanolayers are produced by removing building blocks from the bulk phase to generate the desired structure. Bottom-up synthesis, on the other hand, involves the formation of a nanostructure by stacking up atoms, molecules or other nanoparticles. This process generally uses two methods: physical and/or chemical synthesis. In the former, the constituents of the nanolayers are deposited physically during the fabrication process. The most common method is physical vapor deposition where vapour moieties are condensed through processes such as sputtering or evaporation. In chemical synthesis, chemical reactions are involved as in the chemical vapor deposition (CVD) process.

In most of the reported cases, devices were made from monolayer TMDCs manually exfoliated from a bulk crystal. This approach, while important in proof-of-principle studies, is not suitable, however, for industrial applications. The latter need a simple industry-friendly method to fabricate thin TMDC crystals. The lack of a reliable large-area synthesis process greatly hinders their practical use. An alternative is bottom-up fabrication methods such as chemical vapour transport. This method allows one to fabricate thin layers of TMDC and significant progress has been recently made, but the area of the grown samples remains small, which is also insufficient for mass production of devices. In addition, it requires very high temperatures.

When proof-of-principle results have to be transformed to an industrial scale, a user-friendly cheap mass production technology is needed. One such approach is to use sputtering to fabricate amorphous films with subsequent solid-state crystallization. This approach is more suitable than many alternatives from the viewpoint of cost and productivity since sputtering is a well-established fabrication method, which has long been used for thin film production, for example, of semiconductor devices and optical media. Successful uses of this method have been demonstrated for various transition-metal dichalcogenide films (Hatayama et al. 2022; Huang et al. 2017; 2019; Krbal et al. 2021).

The crystallization process of transition-metal dichalcogenides is unique. Generally, amorphous solids possess the local structure similar to that of the parent crystals, which is known as the Zachariasen paradigm (Zachariasen 1932) stating that glasses must be considered as a media maintaining the local bonding structure of their parent crystals and where only the long-range order is missing. In transition-metal dichalcogenides the situation is fundamentally different. An amorphous solid is isotropic (3D), whereas TMDCs in the crystalline form are layered 2D materials. Consequently, the crystallization of TMDC nanofilms involves lattice dimensionality change, i. e., a 3D-2D transition, which makes this process interesting from the basic physics perspective.

For $MoTe_2$ this transformation is even more complex because of its polymorphism. A multi-step process for recrystallizing 2H-$MoTe_2$ was previously reported (Hatayama et al. 2022; Huang et al. 2017). Namely, as-sputtered amorphous $MoTe_2$ film first crystallizes into the 1T'-phase. It was argued to be a consequence of favorable strain condition in the encapsulated structure (Song et al. 2016), the presence of local tellurium vacancies in the amorphous film (Zhou et al. 2016), and/or potential pre-existence of 1T' nucleation sites. Subsequently, at higher temperatures, the 1T'-MoTe film recrystallizes into a homogeneous 2H-$MoTe_2$ phase. At specific heating conditions the film may directly crystallize into the 2H phase.

Another feature of 2D crystallization is the very unusual sequences of changes in the short and long-range order. While typically crystallization can be viewed as the establishment of the long-range order with the pre-existing short-range order (the same in the amorphous and crystalline phases), in the case of 2D crytallization, long range order (the formation of the layered structure) may be established first, with chemical ordering coming into play later (Saito et al. 2021).

 https://www.doi.org/10.33910/2687-153X-2024-5-4-205-214

Schematically, the process is illustrated in Fig. 1. Figure 1 (right panel) shows the effect of the annealing temperature and time on the obtained polymorphic structure. According to the shown phase diagram, for annealing temperatures of 500 °C and below the $MoTe_2$ film remained in the amorphous phase for annealing times as long as 30 hours (Huang et al. 2019). In contrast, in (Hatayama et al. 2022) crystallization of the amorphous $MoTe_2$ film was reported to start at temperatures just above 300 °C. The observed differences may be explained by different thicknesses of the films in the two cases and/or existing strains. The presence of strain is known to have a significant effect on the structural relaxation processes in chalcogenide films (Kolobov et al. 1982; Raoux et al. 2008; Simpson et al. 2010).

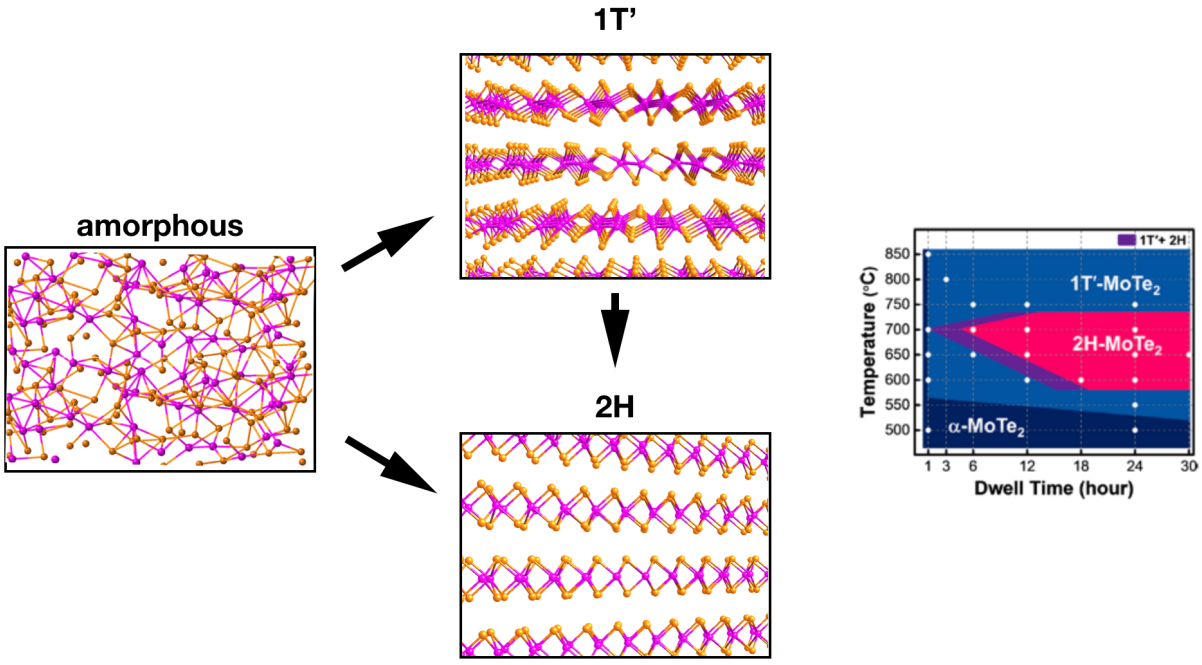

Fig. 1. Schematics of the amorphous $MoTe_2$ crystallization process: depending on the treatment conditions an amorphous film may initially crystallize to the 1T' phase and then to the 2H phase or directly to the 2H phase. The right panel shows the phase diagram after ref. (Huang et al. 2019)

It should be noted that crystallization of TMDC requires heating to relatively low temperatures compared to the process of direct synthesis of the crystalline phase. Indeed, chemical vapor transportation, which is a common method for synthesizing both 2H- and 1T'-$MoTe_2$ bulk materials through a chemical reaction between mixed Mo and Te powders, requires exposure to temperatures on the order of 1100 °C for tens of hours.

At the same time, this solid-state crystallization temperature is sufficiently high to ensure potential chemical interaction of the amorphous film with a substrate. This process, obviously, depends on the substrate material and its chemical reactivity with the components of the film. A solid-state reaction between the substrate and an amorphous TMDC film is especially likely when the substrate is metallic and such situations may exist during devices fabrication process when a film has to be deposited on a metallic contact. The likelihood of such an interaction increases further when the metal belongs to the class of transition metals that can form transition-metal dichalcogenides.

The strong effect of the substrate materials on the formation of oriented 2D crystalline layers was observed by some of the present authors when amorphous Sb_2Te_3 films were grown by magnetron sputtering (Saito et al. 2015). In the cited work, a novel deposition mechanism based on the selective reactivity of the constituent elements of the film (Sb, Te) and the substrate materials giving rise to van der Waals epitaxy was proposed based on the analysis of the binary phase diagrams of (a) Sb–W, (b) Te–W, (c) Sb–Si, (d) Te–Si, (e) Sb–O, and (f) Te–O systems (Bailey 1966; Boller, Nowotny 1964; Knop, Haraldsen 1956; Thurmond, Kowalchik 1960) (see ref. (Saito et al. 2015)). These diagrams could be divided into three classes: one class having no compounds or solid solutions, while for other combinations compounds are formed. In the latter case, compounds with either just one constituent element selectively or with both of them may be formed. In cases when no compounds are formed or both Sb and Te species can

chemically react with the substrate materials, amorphous or polycrystalline films were formed. On the other hand, the use of substrates where Sb did not form a compound with the substrate, while Te did, resulted in significantly different sticking coefficients for the two kinds of atoms, i. e., when Sb and Te atomic species from the plasma reached the substrate, the surface was initially covered with a quasi-monolayer of Te thus passivating the surface.

Upon subsequent film growth the layers became oriented with respect to the substrate. This growth method, called self-organized epitaxy of layered materials was demonstrated to be an efficient industry-friendly fabrication method. It can be speculated that when an amorphous film deposited on a substrate is heated, the selectivity of the substrate material to its constituent elements will also significantly affect the crystallization process. In particular, the film may crystallize (i) as a self-standing film simply supported by the substrate, or (ii) the substrate materials may also be involved in the crystallization process. Furthermore, tellurium is known to crystallize at temperatures as low as room temperature (Zhao et al. 2021). While the presence of transition metal atoms and Te-metal bonds hinders this process, in an amorphous phase Te-rich regions may exist that may be prone to crystallization.

Consequently, investigation of the crystallization process of TMDC nanofilms is important from both fundamental and applied perspectives. In this work, we have experimentally studied the crystallization process of $MoTe_2$ nanolayers on different metallic substrates using differential scanning calorimetry (DSC).

Experimental details

Samples were fabricated by magnetron sputtering and were 100 nm thick $MoTe_2$ films deposited on both sides of 20–25 μm thick foils of four different metals: Al, Ta, Mo, and W. 50 nm nanolayers of SiO_2 were additionally sputtered on top of the $MoTe_2$ to prevent oxidation. We note here that three of the metals used (Mo, W, and Ta) form TMDCs while one of them (Mo) is the same as the transition metal in the studied film. Consequently, when amorphous films are prepared by sputtering, chalcogen species arriving at the substrate may interact not only with metal ions deposited from the plasma but also with the substrate, which can have a certain effect on the composition and structure of the grown films as well as on the details of the crystallization process.

DSC measurements were performed using a DSC 6300 calorimeter (Seiko Instruments, Japan) with the heating rate of 10 deg/min in N_2 atmosphere; the rate of nitrogen flow was 40 ml/min. The cooling rate after scanning was 20 deg/min. Calibration of the temperature scale and enthalpy effects was performed using indium (T_m = 156.6 °C, ΔH_m = 28.6 J/g) and zinc (T_m = 419.6 °C, ΔH_m = 107.5 J/g) standards.

Each studied sample was a stack of 5 mm diameter circles cut from the foil covered on both sides by $MoTe_2$ nanolayers. Depending on the substrate material, the total sample weight varied from 250 to 500 mg, whereas the $MoTe_2$ mass equaled 1–2 mg (see Table 1). This stack was placed into a DSC capsule (aluminium or ceramic) with the internal diameter of 6 mm. The reference was a similar capsule with a stack of the same number of metallic circles cut from the same foil but without $MoTe_2$ and SiO_2 nanolayers. The accuracy of the determination of the glass transition temperatures, T_g's, and crystallization temperatures, T_{cr}'s, was 1–2 °C, whereas the crystallization enthalpies, ΔH_{cr}'s, could be determined with the accuracy of 20% only due to the limited accuracy of mass determination of $MoTe_2$ samples. DSC curves were obtained in temperature ranges from 200 °C to 900 °C in the cases of Ta, W, and Mo substrates (and ceramic pans), and in a range of 200 °C to 600 °C in the case of Al substrate (and Al pan).

Table 1. DSC characteristics of $MoTe_2$ nanolayers on different substrates

Substrate	$MoTe_2$ mass,mg	T_g, °C	Crystallization range, °C	T_{cr}^{max}, °C	Crystallization enthalpy ΔH_{cr}, kj/g
Ta	1.8	333	355–470	400	18.6
–	–	–	428–490	470	3.8
–	–	–	624–807	680	3.7
W	1.6	450	468–800	494	3.8
–	–	–	–	680	–
Al	1.2	468	475–560	495	0.5
Mo	1.8	–	–	–	–

 https://www.doi.org/10.33910/2687-153X-2024-5-4-205-214

Results and Discussion

Figure 2 shows the DSC curves for $MoTe_2$ nanolayers on different substrates (foils) obtained in temperature ranges from 200 °C to 600–900 °C. The crystallization ranges, Tg and T_{cr}^{max} values and the crystallization enthalpies ΔH_{cr} obtained from the measurements are summarized in Table 1.

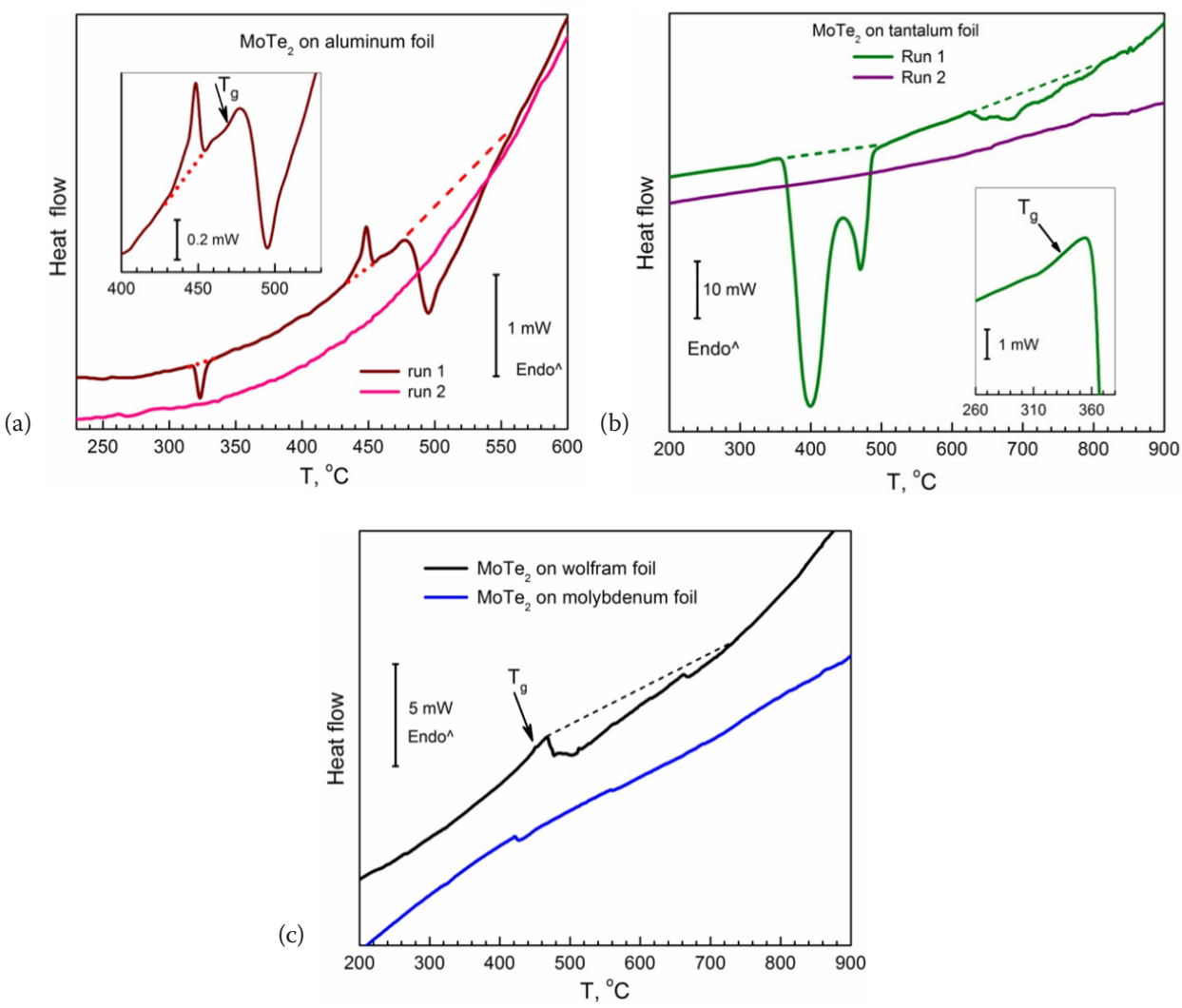

Fig. 2. DSC curves of $MoTe_2$ nanolayers (100 nm thick) during the first and second scans on aluminum (a), tantalum (b) and during the first scan on tungsten and molybdenum foils (c)

One obvious result of these measurements is a drastically different thermal behavior of $MoTe_2$ nanolayers caused by the strong influence of the substrate material on the structural state of deposited nanolayers. Figure 2a shows a DSC curve obtained during the first scan for $MoTe_2$ nanolayers on Al substrate. Several peaks can be clearly observed. The lowest (exothermic) peak at 323 °C can be attributed to the crystallization of Te in the film. The result is consistent with the findings of (Fukuda et al. 2022; Hatayama et al. 2022), where segregation and crystallization of Te upon heating or photoexcitation of an amorphous $MoTe_2$ film to approximately 300 °C was reported. The higher temperature endothermic peak of 445 °C is due to Te melting, which, again, is consistent with the results reported in (Hatayama et al. 2022) and with the literature data (the melting point of pure Te ~ 450 °C).

The relatively high glass-transition temperature around 468 °C (compared with T_g = 350 °C for the film on a tantalum substrate, Fig, 2b) suggests that a film is relatively ordered. Maximal crystallization of the film takes place at 495 °C. A low crystallization enthalpy ΔH_{cr} in this case further indicates a mixed amorphous-crystalline state of $MoTe_2$ nanolayers, with a high degree of ordering already in the initial nanolayer. The heat capacity step at T_g = 468 °C is also dozens of times smaller than that for $MoTe_2$ nanolayers deposited on a Ta substrate. Therefore, the 'residual' crystallization of $MoTe_2$ nanolayers

on Al foil occurs at much higher temperatures, starting at 475 °C. According to the literature, this process corresponds to the formation of the 1T' crystalline phase. Regrettably, the use of Al substrate naturally precluded us from continuing the experiment to higher temperatures.

In the case of a Ta substrate, the DSC curve (green) obtained at the first scan and shown in Fig. 2b had a significantly lower glass-transition temperature (333 °C) indicating that the film was in a more disordered phase, as also evidenced by the maximal heat capacity step in this transition, and high crystallization enthalpy ΔH_{Cr}. In this case, three regions of the crystallization process at temperatures from 355 °C to 807 °C were observed (Fig. 2b, Table 1). Crystallization starts at a much lower temperature than in the case of an Al substrate and the exothermic peak, corresponding to this process, splits into two peaks. It may be possible that the lower peak is associated with the crystallization of Te, while the crystallization of the $MoTe_2$ phase is associated with the second peak. Finally, a second exothermic (crystallization) peak is observed at temperatures higher than 680 °C. We believe that this transition is associated with the 1T' to 2H transformation, which agrees well with the observations and conclusions made in (Hatayama et al. 2022). The features observed for the films on Al and Ta substrates disappeared in the DSC curves during the second scan after heating up and cooling the sample, clearly demonstrating that they are associated with an irreversible crystallization process.

A rather close initial state of partially ordered $MoTe_2$ nanolayers on W foil was observed although their residual crystallization occurred at heating up to 728 °C (Table 1) and the enthalpies associated with the process are significantly lower. Finally, the DSC curve for $MoTe_2$ nanolayers on Mo substrate did not show any essential features upon heating; there was no exothermic or endothermal effects in the DSC curve even during the first scanning process, which suggests they were to a large extent crystalline already in the as-deposited state (Fig. 2c).

The configuration–energy diagram of the crystallization process of amorphous $MoTe_2$ nanofilms, as revealed by the present results, and its schematic representations are shown in Fig. 3 and Fig. 4, respectively.

Thus, we revealed a drastic influence of the substrate material on the structural state of deposited $MoTe_2$ nanolayers, which demonstrates that the crystallization of amorphous $MoTe_2$ is a very complex process. We propose that the underlying cause is the competition of several processes, viz., (i) the film growth from the particles arriving at the substrate from the target, (ii) thermal behavior of various components of the film, and (iii) the interaction of chalcogen atoms with transition metal ions of the substrate leading to oriented growth of the layered crystal as illustrated schematically in Fig. 5. We note that there is a strong similarity between this process and the process of self-organized van der Waals epitaxial growth of Sb_2Te_3 films reported by some of the present authors earlier (Saito et al. 2015).

Based on these results, we can speculate that for oriented growth of layered $MoTe_2$, the substrate material should satisfy one of the following conditions:

- The substrate should have a Te-terminated surface of a properly oriented tellurium compound, such as CdTe.
- The substrate should be made of a material that readily and selectively reacts with Te forming a Te passivation layer, which is the initial step for the oriented growth.
- An advantageous property of a potential substrate is also its flatness. In this case, subsequent growth of the film will proceed in the van der Waals epitaxy mode resulting in the formation of a crystalline film.

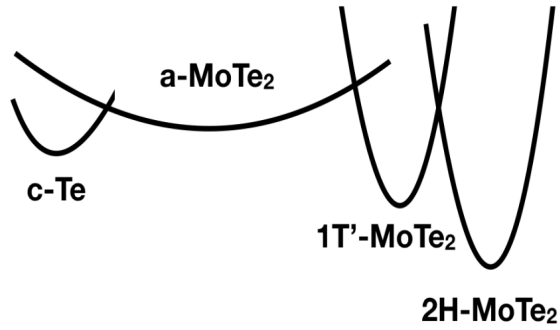

Fig. 3. Configuration–energy diagram describing the $MoTe_2$ crystallization process

 https://www.doi.org/10.33910/2687-153X-2024-5-4-205-214

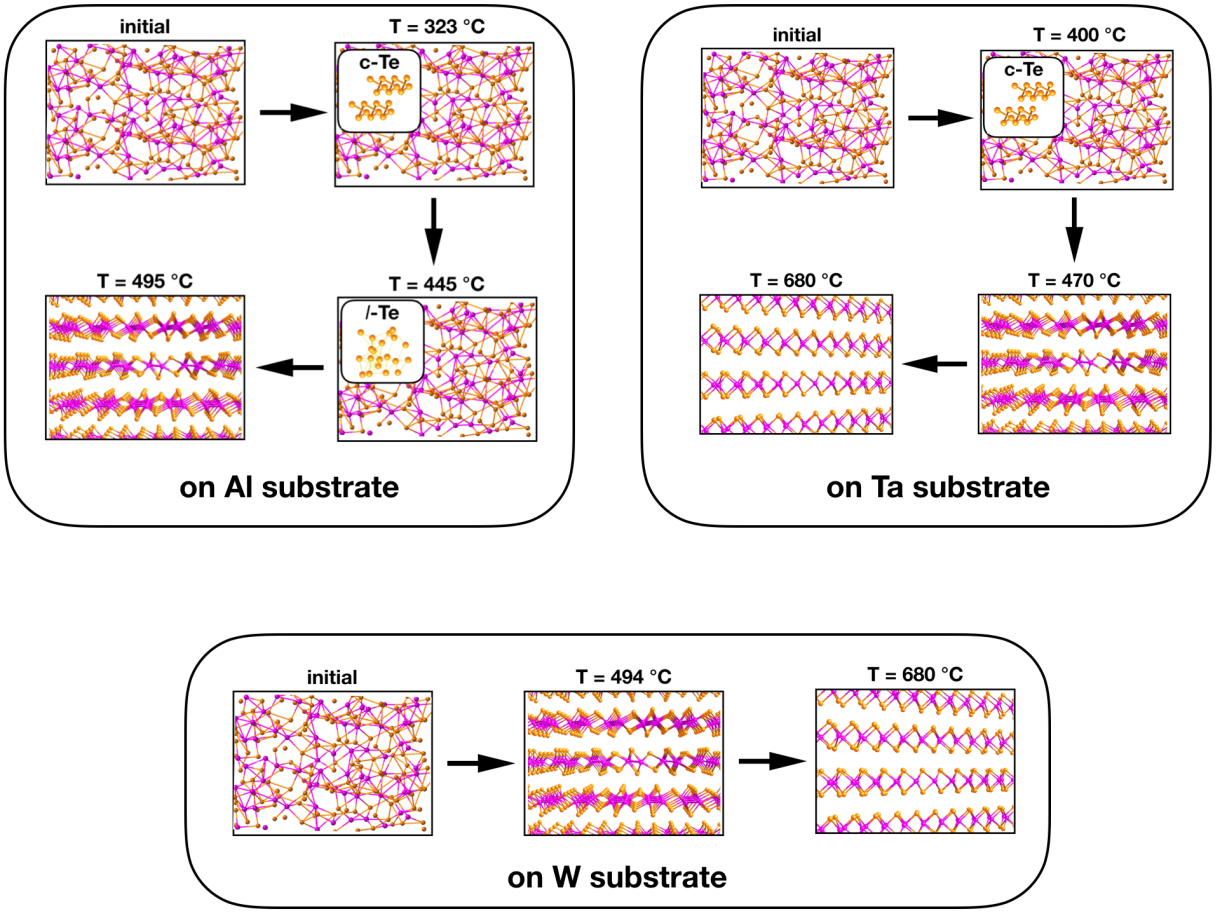

Fig. 4. Schematics of structural evolution of a $MoTe_2$ film deposited on Al, Ta, and W substrates

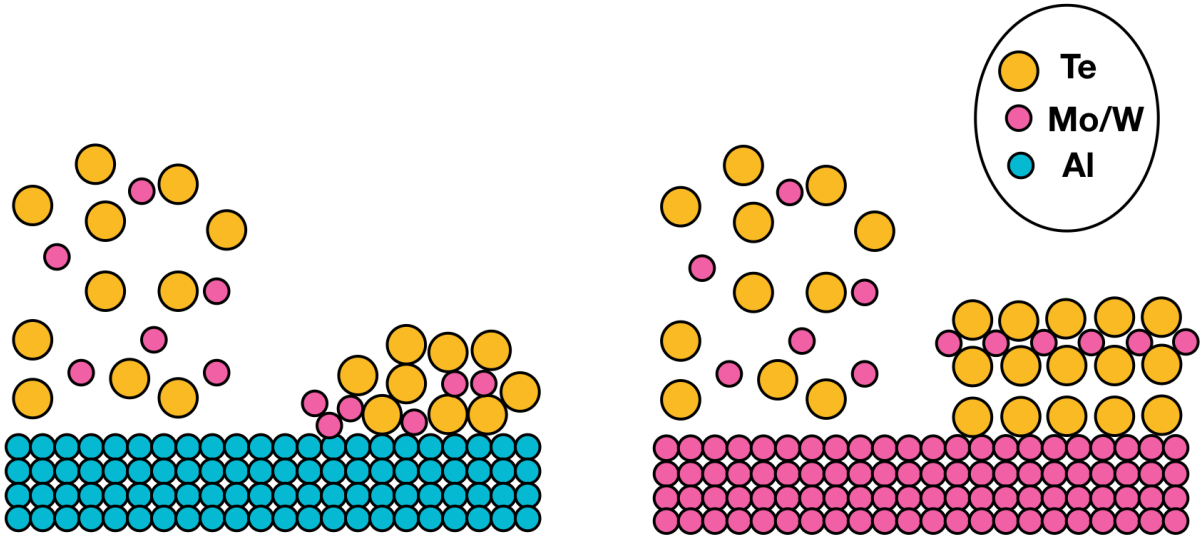

Fig. 5. Schematics of the film growth on an 'inert' substrate such as aluminum/tantalum (left) and on a chemically 'active' substrate such as molybdenum/tungsten (right). In the former case, an amorphous film is formed, while in the latter, strong chemical affinity of the chalcogen atoms in the plasma and TMDC atoms of the substrate results in the growth of a layered crystalline film

Probably the best substrates for this purpose would be terminated surfaces of van der Waals chalcogenides, such as InTe or GaTe of topological insulators such as Sb_2Te_3. While most experimental work concentrates on InSe and GaSe, layered tellurides with the similar structure are also stable as was demonstrated based on the absence of imaginary modes in corresponding phonon dispersion spectra (Demirci et al. 2017) The latter are also a 2D semiconductor with covalently bonded blocks having the Te-In-In-Te stacking sequence. While the lattice constants of InTe (4.40 Å) and GaTe (4.13 Å) (Demirci et al. 2017) are both larger than that of $MoTe_2$ (3.55 Å), van der Waals epitaxy has an advantage that it does not depend on the lattice constant difference between the substrate materials and an overlayer. Hypothetically, the chemical nature of the terminated chalcogen species is not important for van der Waals epitaxy, i. e., $MoTe_2$ should grow as a layered material also on a flat Se-terminated surface. In this case, GaSe (with the lattice constant of 3.82 Å) can be a suitable material.

Conclusions

In conclusion, the fine details of the solid-state crystallization process of amorphous $MoTe_2$ films are known to depend on many aspects such as the film thickness and the heating conditions. Our present results additionally demonstrate a very strong substrate dependence. All these parameters must be taken into consideration when developing technology of $MoTe_2$ film fabrication. We believe that the results obtained for $MoTe_2$ are of general nature and are also applicable to other transition-metal dichalcogenides such as $MoS(e)_2$, $WS(e)_2$ etc. and, possibly, to other classes of van der Waals chalcogenides.

Based on the obtained results we propose a model of the $MoTe_2$ crystallization process and we note that the interpretation of the process based on the DSC studies is very similar to that suggested from direct structural measurements using x-ray diffraction, Raman scattering, and EXAFS (Saito et al. 2015).

Conflict of Interest

The authors of this work declare that they have no conflicts of interest, either existing or potential.

Author Contributions

Conceptualization — Alexandr V. Kolobov, Vladimir A. Bershtein; methodology — Vladimir A. Bershtein; investigation — Pavel N. Yakushev; writing (original draft preparation) — Vladimir A. Bershtein; writing (review and editing) — Alexandr V. Kolobov, Vladimir A. Bershtein. All the authors have read and agreed to the published version of the manuscript.

References

Bailey, L. G. (1966) Preparation and properties of silicon telluride. *Journal of Physics and Chemistry of Solids*, 27 (10), 1593–1598. https://doi.org/10.1016/0022-3697(66)90237-X (In English)

Boller, H., Nowotny, H. (1964) Kristallchemische Untersuchungen in Systemen (Ti, Nb, Ta, Mo, W)–(As, Sb). *Monatshefte für Chemie und Verwandte Teile Anderer Wissenschaften*, 95, 1272–1282. https://doi.org/10.1007/BF00904725 (In English)

Chernikov, A., Berkelbach, T. C., Hill, H. M. et al. (2014) Exciton binding energy and nonhydrogenic Rydberg series in monolayer WS_2. *Physical Review Letters*, 113, article 076802. https://doi.org/10.1103/PhysRevLett.113.076802 (In English)

Cho, S., Kim, S., Kim, J. H. et al. (2015) Phase patterning for ohmic homojunction contact in $MoTe_2$. *Science*, 349 (6248), 625–628. https://doi.org/10.1126/science.aab3175 (In English)

Demirci, S., Avazlı, N., Durgun, E., Cahangirov, S. (2017) Structural and electronic properties of monolayer group III monochalcogenides. *Physical Review B*, 95, article 115409. https://doi.org/10.1103/PhysRevB.95.115409 (In English)

Duerloo, K.-A. N., Li, Y., Reed, E. J. (2014) Structural phase transitions in two-dimensional Mo- and W-dichalcogenide monolayers. *Nature Communications*, 5, article 4214. https://doi.org/10.1038/ncomms5214 (In English)

Fukuda, T., Kaburauchi, R., Saito, Y. et al. (2022) Photo-induced tellurium segregation in $MoTe_2$. *physica status solidi (RRL) — Rapid Research Letters*, 16 (9), article 2100633. https://doi.org/10.1002/pssr.202100633 (In English)

Hatayama, S., Saito, Y., Makino, K. et al. (2022) Phase control of sputter-grown large-area $MoTe_2$ films by preferential sublimation of Te: Amorphous, 1T′ and 2H phases. *Journal of Materials Chemistry C*, 10 (29), 10627–10635. https://doi.org/10.1039/D2TC01281B (In English)

Huang, H. H., Fan, X., Singh, D. J. et al. (2016) Controlling phase transition for single-layer MTe_2 (M = Mo and W): Modulation of the potential barrier under strain. *Physical Chemistry Chemical Physics*, 18 (5), 4086–4094. https://doi.org/10.1039/C5CP06706E (In English)

Huang, J.-H., Hsu, H.-H., Wang, D. et al. (2019) Polymorphism control of layered $MoTe_2$ through two-dimensional solid-phase crystallization. *Scientific Reports*, 9, article 8810. https://doi.org/10.1038/s41598-019-45142-x (In English)

Huang, J.-H., Deng, K.-Y., Liu, P.-S. et al. (2017) Large-area 2D layered $MoTe_2$ by physical vapor deposition and solid-phase crystallization in a tellurium-free atmosphere. *Advanced Materials Interfaces*, 4 (17), article 1700157. http://dx.doi.org/10.1002/admi.201700157 (In English)

Knop, O., Haraldsen, H. (1956) A note on the system wolfram-tellurium. *Canadian Journal of Chemistry*, 34 (8), 1142–1145. https://doi.org/10.1139/v56-149

Kolobov, A. V., Tominaga, J. (2016) *Two-dimensional transition-metal dichalcogenides. Springer Series in Materials Science. Vol. 239*. Cham: Springer Publ., 538 p. https://doi.org/10.1007/978-3-319-31450-1 (In English)

Kolobov, A. V., Fons, P., Tominaga, J. (2016) Electronic excitation-induced semiconductor-to-metal transition in monolayer $MoTe_2$. *Physical Review B*, 94 (9), article 094114. https://doi.org/10.1103/PhysRevB.94.094114 (In English)

Kolobov, A. V., Lyubin, V. M., Taguyrdzhanov, M. A. (1982) Effect of pressure on photoinduced changes in chalcogenide vitreous semiconductors. *Solid State Communications*, 41 (6), 453–455. https://doi.org/10.1016/0038-1098(82)90523-3 (In English)

Krbal, M., Prokop, V., Kononov, A. A. et al. (2021) Amorphous-to-crystal transition in quasi-two-dimensional MoS_2: Implications for 2D electronic devices. *ACS Applied Nano Materials*, 4 (9), 8834–8844. https://doi.org/10.1021/acsanm.1c01504 (In English)

Li, N., Wang, Q., Shen, C. et al. (2020) Large-scale flexible and transparent electronics based on monolayer molybdenum disulfide field-effect transistors. *Nature Electronics*, 3, 711–717. https://doi.org/10.1038/s41928-020-00475-8 (In English)

Li, Y., Duerloo, K.-A. N., Wauson, K., Reed, E. J. (2016) Structural semiconductor-to-semimetal phase transition in two-dimensional materials induced by electrostatic gating. *Nature Communications*, 7, article 10671. https://doi.org/10.1038/ncomms10671 (In English)

Lin, Y.-F., Xu, Y., Wang, S.-T. et al. (2014) Ambipolar $MoTe_2$ transistors and their applications in logic circuits. *Advanced Materials*, 26 (20), 3263–3269. https://doi.org/10.1002/adma.201305845 (In English)

Liu, T., Liu, Z. (2018) 2D MoS_2 nanostructures for biomedical applications. *Advanced Healthcare Materials*, 7 (8), article 1701158. https://doi.org/10.1002/adhm.201701158 (In English)

Mak, K. F., Lee, C., Hone, J. et al. (2010) Atomically thin MoS_2: A new direct-gap semiconductor. *Physical Review Letters*, 105 (13), article 136805. https://doi.org/10.1103/PhysRevLett.105.136805 (In English)

Park, J. C., Yun, S. J., Kim, H. et al. (2015) Phase-engineered synthesis of centimeter-scale 1T′-and 2H-molybdenum ditelluride thin films. *ACS Nano*, 9 (6), 6548–6554. https://doi.org/10.1021/acsnano.5b02511 (In English)

Raoux, S., Jordan-Sweet, J. L., Kellock, A. J. (2008) Crystallization properties of ultrathin phase change films. *Journal of Applied Physics*, 103 (11), article 114310. https://doi.org/10.1063/1.2938076 (In English)

Saito, Y., Fons, P., Kolobov, A. V., Tominaga, J. (2015) Self-organized van der Waals epitaxy of layered chalcogenide structures. *physica status solidi (b)*, 252 (10), 2151–2158. https://doi.org/10.1002/pssb.201552335 (In English)

Saito, Y., Hatayama, S., Shuang, Y. et al. (2021) Dimensional transformation of chemical bonding during crystallization in a layered chalcogenide material. *Scientific Reports*, 11 (1), article 4782. https://doi.org/10.1038/s41598-020-80301-5 (In English)

Sarkar, D., Xie, X., Liu, W. et al. (2015) A subthermionic tunnel field-effect transistor with an atomically thin channel. *Nature*, 526 (7571), 91–95. https://doi.org/10.1038/nature15387 (In English)

Simpson, R. E., Krbal, M., Fons, P. et al. (2010) Toward the ultimate limit of phase change in $Ge_2Sb_2Te_5$. *Nano Letters*, 10 (2), 414–419. https://doi.org/10.1021/nl902777z (In English)

Song, S., Keum, D. H., Cho, S. et al. (2016) Room temperature semiconductor–metal transition of $MoTe_2$ thin films engineered by strain. *Nano Letters*, 16 (1), 188–193. https://doi.org/10.1021/acs.nanolett.5b03481 (In English)

Suzuki, R., Sakano, M., Zhang, Y. J. et al. (2014) Valley-dependent spin polarization in bulk MoS_2 with broken inversion symmetry. *Nature Nanotechnology*, 9 (8), 611–617. https://doi.org/10.1038/nnano.2014.148 (In English)

Tang, J., Wang, Q., Tian, J. et al. (2023) Low power flexible monolayer MoS2 integrated circuits. *Nature Communications*, 14 (1), article 3633. https://doi.org/10.1038/s41467-023-39390-9 (In English)

Thurmond, C. D., Kowalchik, M. (1960) Germanium and silicon liquidus curves. *The Bell System Technical Journal*, 39 (1), 169–204. https://doi.org/10.1002/j.1538-7305.1960.tb03927.x (In English)

Ueno, K., Fukushima, K. (2015) Changes in structure and chemical composition of α-$MoTe_2$ and β-$MoTe_2$ during heating in vacuum conditions. *Applied Physics Express*, 8 (9), article 095201. https://doi.org/10.7567/APEX.8.095201 (In English)

Wei, W., Dai, Y., Huang, B. (2017) Straintronics in two-dimensional in-plane heterostructures of transition-metal dichalcogenides. *Physical Chemistry Chemical Physics*, 19 (1), 663–672. https://doi.org/10.1039/C6CP07823K (In English)

Xiao, D., Liu, G.-B., Feng, W. et al. (2012) Coupled spin and valley physics in monolayers of MoS_2 and other group-VI dichalcogenides. *Physical Review Letters*, 108 (19), article 196802. https://doi.org/10.1103/PhysRevLett.108.196802 (In English)

Yin, L., Zhan, X., Xu, K. et al. (2016) Ultrahigh sensitive $MoTe_2$ phototransistors driven by carrier tunneling. *Applied Physics Letters*, 108 (4), article 043503. https://doi.org/10.1063/1.4941001 (In English)

Yoo, Y., DeGregorio, Z. P., Su, Y. et al. (2017) In-plane 2H-1T′ $MoTe_2$ homojunctions synthesized by flux-controlled phase engineering. *Advanced Materials*, 29 (16), article 1605461. https://doi.org/10.1002/adma.201605461 (In English)

Zachariasen, W. H. (1932) The atomic arrangement in glass. *Journal of the American Chemical Society*, 54 (10), 3841–3851. https://doi.org/10.1021/ja01349a006 (In English)

Zhao, C., Batiz, H., Yasar, B. et al. (2021) Tellurium single-crystal arrays by low-temperature evaporation and crystallization. *Advanced Materials*, 33 (37), article 2100860. https://doi.org/10.1002/adma.202100860 (In English)

Zhou, L., Xu, K., Zubair, A. et al. (2015) Large-area synthesis of high-quality uniform few-layer $MoTe_2$. *Journal of the American Chemical Society*, 137 (37), 11892–11895. https://doi.org/10.1021/jacs.5b07452 (In English)

Zhou, L., Zubair, A., Wang, Z. et al. (2016) Synthesis of high-quality large-area homogenous 1T′ $MoTe_2$ from chemical vapor deposition. *Advanced Materials*, 28 (43), 9526–9531. https://doi.org/10.1002/adma.201602687 (In English)

Check for updates

Physics of Semiconductors.
Defects in the crystal structure

UDC 538.9

EDN ZDGBEQ
https://www.doi.org/10.33910/2687-153X-2024-5-4-215-220

Calculation of the formation energy and transformation probabilities of some intrinsic defects in hexagonal boron nitride

I. I. Yanibekov ✉[1], Yu. V. Petrov [1]

[1] Saint Petersburg State University, 7/9 Universitetskaya Emb., Saint Petersburg 199034, Russia

Authors

Iskander I. Yanibekov, ORCID: 0009-0003-4400-0168, e-mail: iskander1331@mail.ru

Yuri V. Petrov, ORCID: 0000-0003-3084-3677, e-mail: y.petrov@spbu.ru

For citation: Yanibekov, I. I., Petrov, Yu. V. (2024) Calculation of the formation energy and transformation probabilities of some intrinsic defects in hexagonal boron nitride. *Physics of Complex Systems*, 5 (4), 215–220. https://www.doi.org/10.33910/2687-153X-2024-5-4-215-220 EDN ZDGBEQ

Received 28 August 2024; reviewed 11 October 2024; accepted 11 October 2024.

Funding: The research is supported by the Russian Science Foundation, project No. 23-22-00067.

Copyright: © I. I. Yanibekov, Yu. V. Petrov (2024) Published by Herzen State Pedagogical University of Russia. Open access under CC BY-NC License 4.0.

Abstract. Hexagonal boron nitride (h-BN) is of interest due to its potential use in electronics and, in particular, the fabrication of single-photon emitters. In this paper, some properties of defects, namely, a boron vacancy (V_B) and an anti-site complex with a nitrogen vacancy (N_BV_N) in various charge states are studied. The energies of defect formation are calculated using density functional theory (DFT). Probabilities of transitions between them are estimated, and the annealing temperatures required for the transformation of h-BN are calculated.

Keywords: defects in hexagonal boron nitride, DFT, boron vacancy, anti-site nitrogen vacancy complex, defect transformation

Introduction

Hexagonal boron nitride (h-BN) is currently used as a material for dielectric substrates in electronics (Dean et al. 2010) and high-frequency devices (Pazos et al. 2024), and is considered as a promising candidate for single-photon emitters for quantum cryptography. It has a hexagonal structure and a band gap of about 6 eV (Cassabois et al. 2016).

One of the variants of single-photon sources can be an anti-site complex with a nitrogen vacancy (N_BV_N) (Liu et al. 2024; Tran et al. 2016). At the moment, there are several works (Grosso et al. 2017; Venturi et al. 2024) devoted to the methods of fabricating N_BV_N by irradiating a sample with helium ions with V_B formation and subsequent annealing, but the modeling of the V_B–N_BV_N transformation process has not been published yet.

The purpose of this work is to calculate the formation energies of V_B and N_BV_N vacancies in various charge states by means of DFT and to determine which of them is the most energetically favorable under given conditions, as well as finding the energy barriers required to transform one type of a defect into another.

Methods

In this paper, we perform calculations of h-BN energy using a density functional theory (DFT) approach. The structure was simulated using the ASE software package (Larsen et al. 2017). First, we created a h-BN supercell consisting of 4 layers with a total number of 128 atoms and hexagonal lattice constants a = 2.5 and c = 6.65 (Fig. 1 (a)). Then we obtained the required defect types by removing and moving atoms (Fig. 1 (b, c)).

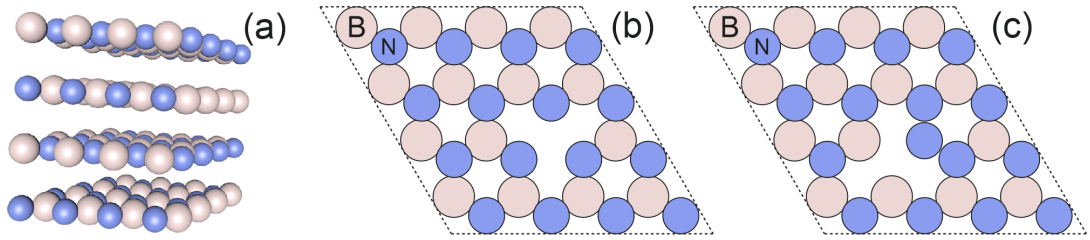

Fig. 1. (a) General side view of the modeled structure; (b) schematic representation of the first layer of the simulated structure with a V_B defect; (c) schematic representation of the first layer of the simulated structure with a $N_B V_N$ defect

The energy was calculated using the GPAW energy calculator (Mortensen et al. 2024) with the following parameters: periodic boundary conditions in all directions, plane wave basis (PW) and PBE exchange-correlation functional (Perdew et al. 1996). The calculation was performed for 2 special points in the Brillouin zone, namely Γ and M. The Kohn–Sham orbitals occupations determined using the Fermi–Dirac function with kT = 25 meV, corresponding to room temperature. Then, the structure was optimized using the MDMin method (Verlet method modification) by minimizing the energy using the minimum of the forces between atoms.

When calculating the energies for different charge states, the charges were added to the GPAW calculator, and the resulting electrostatic corrections, which will be discussed below, were taken into account during the final energy calculation.

After optimizing the structures, we calculated the defect energy taking into account its charge using the following formula (Weston et al. 2018):

$$E_{def}(E_F) = E_{dfull} - E_{h-BN} - \mu_B - E_{elc}[q] + q(\Delta V + E_F) \quad (1)$$

where E_{dfull} — full energy of the structure with a defect after optimization, E_{h-BN} — full energy of the structure without defects, $\mu_B = 2{,}9\ eV$ — chemical potential of Boron (Weston et al. 2018), $E_{elc}[q]$ — electrostatic correction, q — defect charge, E_F — Fermi energy, and ΔV — parameter required to align the electrostatic potential of the defect-containing supercell with the electrostatic potential of a pristine supercell. Its value is a function of the distance from the defect and has to be selected from an area located far from the defect (Freysoldt et al. 2011).

The chemical potential of Boron μ_B can be 0 eV or 2.9 eV depending on the conditions of growth: B-poor or N-poor correspondingly (Weston et al. 2018). However, this choice does not play a significant role not only in the calculation of the barriers, but also in comparing the formation energies, since it leads to the same shift of the zero level of the formation energies for both types of defects considered.

Then, using the energies of defect formation as edge points, we calculated the energy barriers of the transitions between defects using the Nudged Elastic Band (NEB) method (Lindgren et al. 2019) with 8 intermediate points between the initial and final positions of atoms in the supercell.

Knowing the values of the transition barrier energies, we calculated the transition probabilities at room temperature using (Weston et al. 2018):

$$\Gamma = \Gamma_0 \exp\left(-\frac{E_b}{k_b T}\right) \quad (2)$$

where $\Gamma_0 = 10^{14}\, s^{-1}$ h-BN phonon frequency (Geick et al. 1966), E_b — transition barrier, k_b — Boltzmann constant, and T — temperature.

Then we estimated the annealing temperature corresponding to $\Gamma = 1 s^{-1}$:

$$T = \frac{-E_b}{k_b \ln\left(\frac{\Gamma}{\Gamma_0}\right)} \quad (3)$$

It is also worth noting that the annealing temperature is not so sensitive to the choice of the constant Γ_0 because of the logarithmic dependence in (3).

 https://www.doi.org/10.33910/2687-153X-2024-5-4-215-220

Results and discussion

After the structural optimization we calculated the maximum atom displacements relative to the lattice sites in an ideal crystal, and for neutral defects they were of 0.075 Å for V_B and 0.045 Å for N_BV_N. These values are two orders of magnitude smaller than the lattice constants, and their detailed analysis is beyond the scope of this study.

Based on the obtained defect formation energies, we can plot the dependence of the defect formation energy on the Fermi level in various charge states (Fig. 2). As it can be seen from (1), when the defect is neutral ($q = 0$), there is no dependence of the defect formation energy on the Fermi level within the band gap. These states correspond to the horizontal solid red and black lines in (Fig. 2).

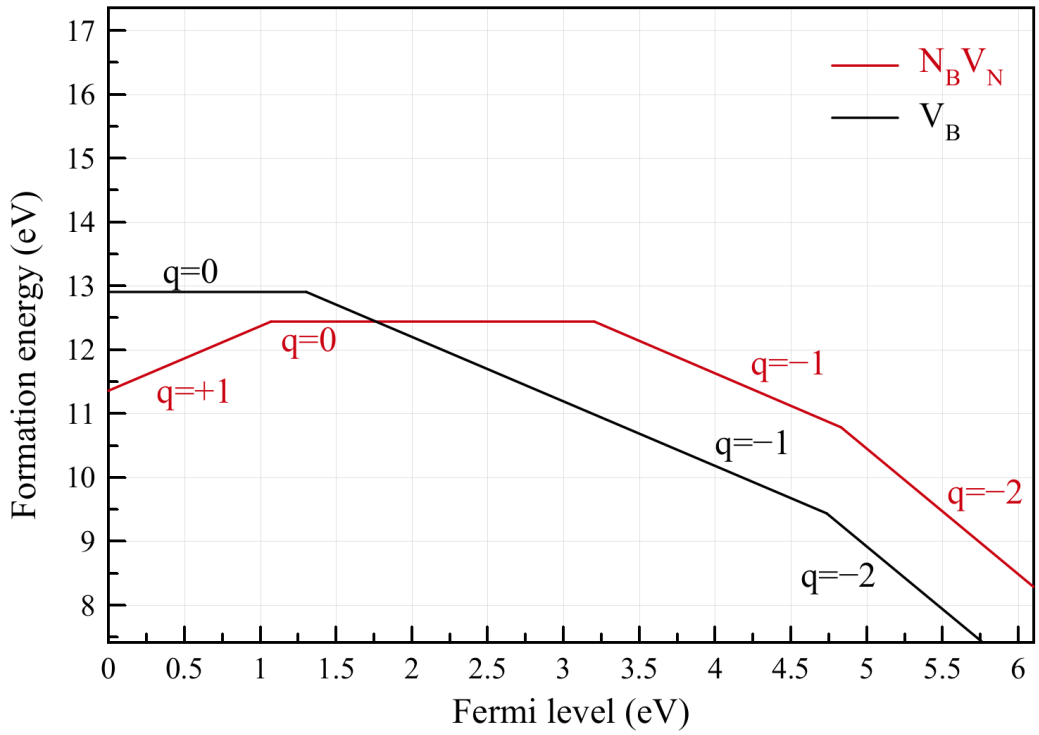

Fig. 2. Dependences of the defect formation energy on the Fermi level in different charge states

Table 1 presents the ranges of Fermi level values at which certain charge states are energetically more favorable for each type of defect, as well as the transition points between charge states. The red curve in (Fig. 2), corresponding to V_B, intersects with the black curve N_BV_N at a Fermi level of 1.75 eV and a formation energy of 12.9 eV.

Table 1. The most energetically favorable defect charges depending on the Fermi level

Charge of defect	V_B		N_BV_N	
	Fermi level, eV	Transition point, eV	Fermi level, eV	Transition point, eV
+1	–	–	0–1	12.4
0	0–1.25		1–3.2	
–1	1.25–4.75	12,9	3.2–4.8	12.4
–2	4.75–6	9,4	4.8–6	10.9

For further analysis, we will consider an intrinsic semiconductor, and therefore, focus on the transitions with the Fermi level near the center of the band gap. Thus, according to (Fig. 2), in the intrinsic h-BN, the boron vacancy V_B in the center of the band gap has a charge of –1, while N_BV_N is neutral. During annealing or electron irradiation (Petrov et al. 2023), ionization of the vacancy is possible, so several processes leading to the transformation between V_B and N_BV_N are possible:

(0) V_B^{-1}–V_B^0 transition (blue arrow in Fig. 3(a)) — this transition is the ionization and a starting point for processes (1) and (2).

(1) V_B^0–$N_BV_N^0$ transition (orange arrow in Fig. 3(a)).

(2) Transition from V_B^0 (dotted line in Fig. 3(a)) in the atomic positions corresponding to the optimized charge state V_B^{-1} to $N_BV_N^0$ (purple arrow in Fig. 3(a)) — transition without relaxation, which might take place immediately after ionization, when the atomic structure has not relaxed yet.

In addition to the process described above, a transition without ionization is also possible:

(3) V_B^{-1}–$N_BV_N^{-1}$ transition (bright-green arrow in Fig. 3(a)).

And then, after the ionization, the system comes to the same neutral N_BV_N:

(4) $N_BV_N^{-1}$–$N_BV_N^0$ transition (dark-green arrow in Fig. 3(a)).

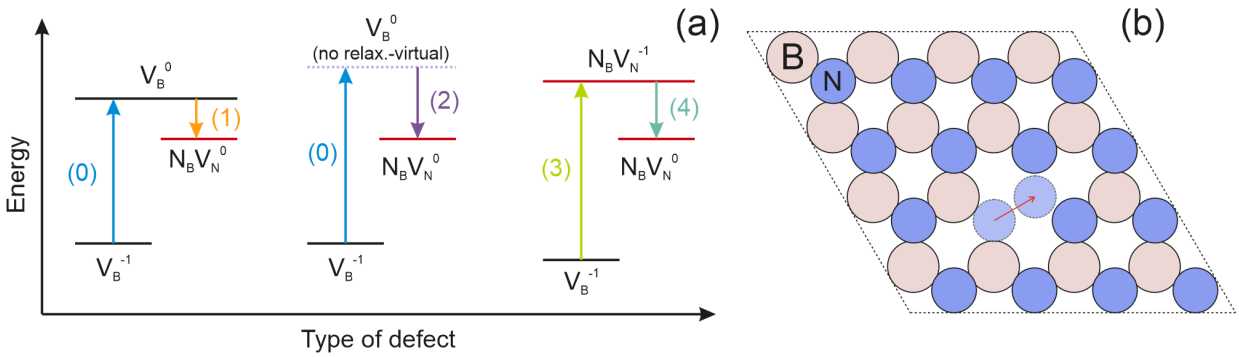

Fig. 3. (a) Schematic representation of transitions; (b) schematic representation of V_B–N_BV_N transformation

Considering the initial and final states for the processes (1), (2) and (3) mentioned above, we can calculate the transition barriers between different types of defects (Fig. 4).

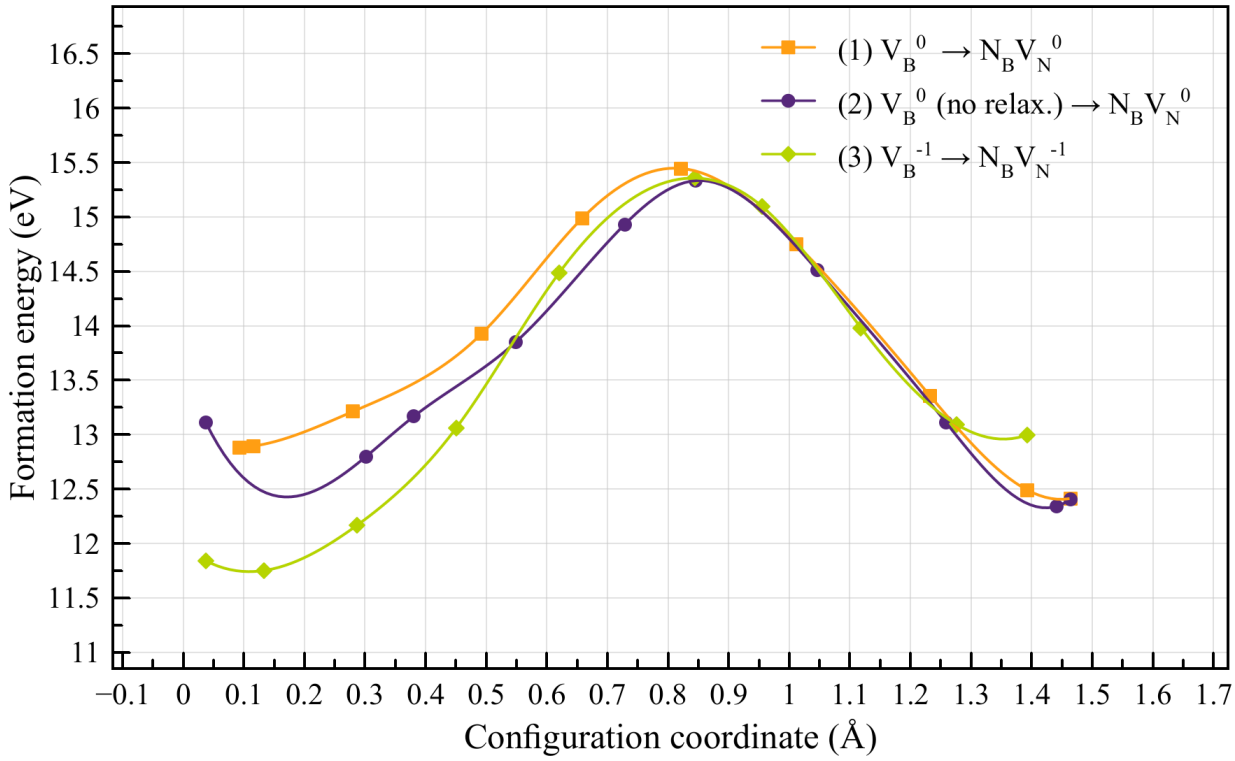

Fig. 4. Transition barriers between V_B and N_BV_N. Zero configuration coordinate corresponds to V_B

Based on the obtained barrier values using formulas (2) and (3), we can calculate the transition probabilities and annealing temperatures for forward (V_B to N_BV_N) and reverse (N_BV_N to V_B) transitions. The results are presented in Table 2.

 https://www.doi.org/10.33910/2687-153X-2024-5-4-215-220

Table 2. The values of the forward (E_f) and reverse (E_r) transition barriers (1) – (3), along with the calculated transition probabilities and annealing temperatures

Type of transition	E_f, eV	E_r, eV	Γ_f, s^{-1}	Γ_r, s^{-1}	T_f, K	T_b, K
(1)	2.57	3.03	2.76×10^{-31}	2.13×10^{-39}	923	1091
(2)	2.22	2.93	2.41×10^{-25}	–	800	–
(3)	3.52	2.36	8.33×10^{-48}	9.66×10^{-28}	1265	849

As shown in Table 2, the barrier for the transition from V_B to N_BV_N in the neutral state is lower than in the negatively charged state, but in all cases exceeds 2 eV, and the transition probabilities at room temperature are negligible. This indicates that to create N_BV_N–type defects from V_B, the structure must be provided with sufficient energy, such as through heating. The obtained annealing temperatures for the transitions are consistent with experimental results (Grosso et al. 2017; Tran et al. 2016; Venturi et al. 2024). Additionally, since the barrier for the reverse transition (3) is lower than that for the forward transition, the probability of the transformation from N_BV_N to V_B in the negatively charged state is quite high.

Conclusions

In this work, we calculated the formation energy of V_B and N_BV_N in different charge states for h-BN using the DFT method. The obtained values allowed us to consider transitions between defects and calculate their barriers. The latter were used to calculate the annealing temperatures and transition probabilities at room temperature. We assume that the process of defect transformation at room temperature observed in the work (Petrov et al. 2023) can be caused by the recombination of nonequilibrium excess charge carriers excited during electron irradiation. To complete the description of the studied processes, ionization processes should be considered in more detail. Therefore, we plan to continue investigating the ionization energies of V_B and N_BV_N further.

Conflict of Interest

The authors declare that there is no conflict of interest, either existing or potential.

Author Contributions

All the authors discussed the final work and took an equal part in writing the article.

References

Cassabois, G., Valvin, P., Gil, B. (2016) Hexagonal boron nitride is an indirect bandgap semiconductor. *Nature Photonics*, 10 (4), 262–266. https://doi.org/10.1038/nphoton.2015.277 (In English)

Dean, C. R., Young, A. F., Meric, I. et al. (2010) Boron nitride substrates for high-quality graphene electronics. *Nature Nanotechnology*, 5 (10), 722–726. https://doi.org/10.1038/nnano.2010.172 (In English)

Freysoldt, C., Neugebauer, J., van de Walle, C. G. (2011) Electrostatic interactions between charged defects in supercells. *Physica Status Solidi B*, 248 (5), 1067–1076. https://doi.org/10.1002/pssb.201046289 (In English)

Geick, R., Perry, C. H., Rupprecht, G. (1966) Normal modes in hexagonal boron nitride. *Physical Review*, 146 (2), article 543. https://doi.org/10.1103/PhysRev.146.543 (In English)

Grosso, G., Moon, H., Lienhard, B. et al. (2017) Tunable and high-purity room temperature single-photon emission from atomic defects in hexagonal boron nitride. *Nature Communications*, 8 (1), article 705. https://doi.org/10.1038/s41467-017-00810-2 (In English)

Larsen, A. H., Mortensen, J. J., Blomqvist, J. (2017) The atomic simulation environment—a Python library for working with atoms. *Journal of Physics: Condensed Matter*, 29 (27), article 273002. https://doi.org/10.1088/1361-648X/aa680e (In English)

Lindgren, P., Kastlunger, G., Peterson, A. A. (2019) Scaled and dynamic optimizations of nudged elastic bands. *Journal of Chemical Theory and Computation*, 15 (11), 5787–5793. https://doi.org/10.1021/acs.jctc.9b00633 (In English)

Liu, G-L., Wu, X-Y., Jing, P-T. et al. (2024) Single photon emitters in hexagonal boron nitride fabricated by focused helium ion beam. *Advanced Optical Materials*, 12 (9), article 2302083. https://doi.org/10.1002/adom.202302083 (In English)

Mortensen, J. J., Larsen, A. H., Kusima, M. et al. (2024) GPAW: An open python package for electronic structure calculations. *The Journal of Chemical Physics*, 160 (9), article 092503. https://doi.org/10.1063/5.0182685 (In English)

Pazos, S., Shen, Y., Zhang, H. et al. (2024) Memristive circuits based on multilayer hexagonal boron nitride for millimetre-wave radiofrequency applications. *Nature Electronics*, 7 (7), 557–566. https://doi.org/10.1038/s41928-024-01192-2 (In English)

Perdew, J. P., Burke, K. Ernzerhof, M. (1996) Generalized gradient approximation made simple. *Physical Review Letters*, 77 (18), 3865–3868. https://doi.org/10.1103/PhysRevLett.77.3865 (In English)

Petrov, Yu. V., Gogina, O. A., Vyvenko, O. F. et al. (2023) Effect of combined ion and electron irradiation on 2 eV luminescence band in hexagonal boron nitride. *Technical Physics*, 68 (7), 856–862. https://doi.org/10.61011/TP.2023.07.56627.62-23 (In English)

Tran, T. T., Bray, K., Ford, M. J. et al. (2016) Quantum emission from hexagonal boron nitride monolayers. *Nature Nanotechnology*, 11 (1), 37–41. https://doi.org/10.1038/NNANO.2015.242 (In English)

Venturi, G., Chiodini, S., Melchioni, N. et al. (2024) Selective generation of luminescent defects in hexagonal boron nitride. *Laser & Photonics Reviews*, 18 (6), article 2300973. https://doi.org/10.1002/lpor.202300973 (In English)

Weston, L., Wickramaratne, D., Mackoit, M. et al. (2018) Native point defects and impurities in hexagonal boron nitride. *Physical Review B*, 97 (21), article 214104. https://doi.org/10.1103/PhysRevB.97.214104 (In English)

Summaries in Russian / Информация о статьях на русском языке

Физика конденсированного состояния

ПЛАВЛЕНИЕ И ВОЗГОНКА ГРАФЕНА И СИЛИЦЕНА

Юрий Дмитриевич Фомин, Елена Николаевна Циок, Валентин Николаевич Рыжов

Аннотация. В данном исследовании проведено моделирование методом молекулярной динамики процесса разрушения кристаллической структуры графена, графита и силицена. Показано, что в случае графена и графита разрушение кристаллической структуры связано с сублимацией образца. В то же время, когда образец силицена нагревается при постоянном объеме, он переходит в двухфазную область фазовой диаграммы жидкость–газ. Разница в разрушении кристаллической структуры графена и силицена вызвана различиями в давлении тройной точки жидкость–газ–кристалл.

Ключевые слова: метод молекулярной динамики, графен, силицен, сублимация, тройная точка жидкость–газ–кристалл

Для цитирования: Galiullin, A. A., Lunev, I. V., Gumarov, A. I., Yanilkin, I. V. (2024) Dielectric properties of thin-film metal/dielectric nanocomposites based on zirconium nitrides. *Physics of Complex Systems*, 5 (4), 172–176. https://www.doi.org/10.33910/2687-153X-2024-5-4-172-176 EDN PVLCLE

ДИЭЛЕКТРИЧЕСКИЕ СВОЙСТВА ТОНКОПЛЕНОЧНЫХ НАНОКОМПОЗИТОВ ТИПА МЕТАЛЛ/ДИЭЛЕКТРИК НА БАЗЕ НИТРИДОВ ЦИРКОНИЯ

Артур Альбертович Галиуллин, Иван Владимирович Лунев, Амир Илдусович Гумаров, Игорь Витальевич Янилкин

Аннотация. Синтезированы пленки оксинитрида циркония методом напыления нитрида циркония с последующим атмосферным отжигом до оксинитрида. Полученные пленки исследованы методом диэлектрической спектроскопии. Показано, что температура отжига влияет на диэлектрические свойства пленки. Атмосферный отжиг приводит к дисперсии диэлектрической проницаемости и релаксационным процессам. Нелинейный характер температурной зависимости времени релаксации и различие времен релаксации образцов являются проявлениями их гетерогенной структуры и размерного эффекта структуры металл/диэлектрик.

Ключевые слова: гетерогенные материалы, диэлектрическая спектроскопия, диэлектрическая релаксация, оксинитриды циркония, тонкие пленки

Для цитирования: Fomin, Yu. D., Tsiok, E. N., Ryzhov, V. N. (2024) Melting and sublimation of graphene and silicene. *Physics of Complex Systems*, 5 (4), 177–186. https://www.doi.org/10.33910/2687-153X-2024-5-4-177-186 EDN JFGSTK

ПОЛЕВАЯ ЗАВИСИМОСТЬ ВРЕМЕНИ ОБРАЗОВАНИЯ ЭЛЕКТРИЧЕСКИХ ДЕНДРИТОВ В ПОЛИМЕРНОЙ ИЗОЛЯЦИИ

Валентин Владимирович Киселевич

Аннотация. Проанализированы известные выражения для описания полевой зависимости времени зарождения электрических дендритов в полимерной изоляции и отмечена необходимость модификации этих выражений для возможности корректного определения пороговых параметров дендритообразования. В рамках представлений теории катастроф получено уравнение зависимости времени зарождения дендритов в полимерных диэлектриках от величины максимальной локальной напряжённости электрического поля. Определены параметры данного уравнения для эпоксидной и полиэтиленовой изоляции. Установлено хорошее согласие между литературными экспериментальными данными и полевыми зависимостями времени зарождения дендритов, построенными по предложенному уравнению. Рассмотрены геометрические свойства функции катастрофы складки, характеризующей закономерности изменения времени образования электрических дендритов в полиэтиленовой изоляции.

Ключевые слова: полимерная изоляция, электрические дендриты, время зарождения дендритов, максимальная локальная напряжённость электрического поля, пороговые параметры дендритообразования, теория катастроф, катастрофа складки

Для цитирования: Kiselevich, V. V. (2024) Field dependence of the initiation time of electrical trees in polymer insulation. *Physics of Complex Systems*, 5 (4), 187–194. https://www.doi.org/10.33910/2687-153X-2024-5-4-187-194 EDN HBQYTU

ЭЛЕКТРОФИЗИЧЕСКИЕ СВОЙСТВА СЕГНЕТОВОЙ СОЛИ, ДИСПЕРГИРОВАННОЙ В ПОРИСТОЙ ДИЭЛЕКТРИЧЕСКОЙ МАТРИЦЕ ЦЕОЛИТА ТИПА А

Тамара Геннадьевна Матвеева, Марина Семеновна Иванова, Владимир Гаевич Соловьев, Александр Иванович Ванин

Аннотация. В диапазоне частот от 100 Гц до 100 кГц были исследованы электропроводность, действительная часть диэлектрической проницаемости и диэлектрические потери нового нанокомпозиционного материала, полученного путем пропитки матрицы цеолита NaA сегнетовой солью.

Наблюдался низкотемпературный сдвиг точки Кюри T_C верхнего сегнетоэлектрического перехода вещества-«гостя» из-за влияния ограниченной геометрии. Показано, что вид температурной зависимости электропроводности сегнетовой соли, а также характер частотной зависимости диэлектрических потерь существенно изменяются при диспергировании этого сегнетоэлектрика в цеолите NaA.

Ключевые слова: сегнетоэлектрики, сегнетова соль, диэлектрическая проницаемость, диэлектрические потери, электропроводность, цеолит, нанокомпозит

Для цитирования: Matveeva, T. G., Ivanova, M. S., Solovyev, V. G., Vanin, A. I. (2024) Electrophysical properties of the Rochelle salt dispersed in a porous dielectric matrix of type A zeolite. *Physics of Complex Systems*, 5 (4), 195–201. https://www.doi.org/10.33910/2687-153X-2024-5-4-195-201 EDN JARMUT

ЭЛЕКТРЕТНОЕ СОСТОЯНИЕ И СМАЧИВАЕМОСТЬ ПОЛИМЕРНЫХ МАТЕРИАЛОВ, ОБРАБОТАННЫХ В ТЛЕЮЩЕМ РАЗРЯДЕ ПОСТОЯННОГО ТОКА

Михаил Юрьевич Яблоков, Александр Алексеевич Кузнецов

Аннотация. Было изучено влияние электретного заряда на гидрофильность пленок политетрафторэтилена (ПТФЭ), обработанных в тлеющем разряде постоянного тока. Обработка полимеров в разряде постоянного тока приводит к значительной гидрофилизации поверхности и появлению поверхностных зарядов на изначально гидрофобной поверхности полимеров. Было показано, что после плазменной обработки хранение пленок ПТФЭ на воздухе с различной относительной влажностью приводит к увеличению угла смачивания водой и одновременному снижению поверхностного потенциала. Процесс восстановления гидрофобности пленок ПТФЭ, обработанных плазмой, рассматривается как следствие релаксации заряда во влажной атмосфере. Было установлено, что зарядка поверхности в процессе плазменной обработки полимеров вносит существенный вклад в их гидрофильность.

Ключевые слова: тлеющий разряд постоянного тока, обработка в плазме, смачивание, полимерные электреты, восстановление гидрофобности

Для цитирования: Yablokov, M. Yu., Kuznetsov, A. A. (2024) Electret properties and wettability of polymer materials treated by DC glow discharge. *Physics of Complex Systems*, 5 (4), 202–204. https://www.doi.org/10.33910/2687-153X-2024-5-4-202-204 EDN WNDCIU

Физика полупроводников

ФОРМИРОВАНИЕ НАНОПЛЕНОК $MoTe_2$ НА МЕТАЛЛИЧЕСКИХ ПОДЛОЖКАХ

Павел Николаевич Якушев, Владимир Абрамович Берштейн, Александр Владимирович Колобов

Аннотация. Дихалькогениды переходных металлов являются одними из наиболее изучаемых двумерных полупроводников для использования в электронике, оптоэлектронике и спинтронике, а также в устройствах памяти. Одним из простых коммерчески привлекательных методов получения тонких кристаллических пленок является твердофазная кристаллизация из аморфной фазы.

В данной работе, используя измерения дифференциальной сканирующей калориметрии (DSC), мы продемонстрировали, что нанослои $MoTe_2$, осажденные на различные подложки (Ta, Al, W, Mo), демонстрируют заметно отличающееся поведение при кристаллизации. На основании полученных результатов в работе предполагается, что эти различия связаны с разным химическим сродством компонентов пленки к материалу подложки, и предлагается схема этого сложного процесса кристаллизации.

Ключевые слова: дихалькогениды переходных металлов, твердофазная кристаллизация, дифференциальная сканирующая калориметрия, нанопленки, двумерные полупроводники

Для цитирования: Yakushev, P. N., Bershtein, V. A., Kolobov, A. A. (2024) The formation of $MoTe_2$ nanofilms on metal substrates. *Physics of Complex Systems*, 5 (4), 205–214. https://www.doi.org/10.33910/2687-153X-2024-5-4-205-214 EDN THHPQB

РАСЧЕТ ЭНЕРГИИ ОБРАЗОВАНИЯ И ВЕРОЯТНОСТЕЙ ТРАНСФОРМАЦИИ НЕКОТОРЫХ СОБСТВЕННЫХ ДЕФЕКТОВ В ГЕКСАГОНАЛЬНОМ НИТРИДЕ БОРА

Искандер Ильдарович Янибеков, Юрий Владимирович Петров

Аннотация. Гексагональный нитрид бора (h-BN) интересен потенциалом применения в электронике и, в частности, в создании однофотонных источников. В данной работе изучаются некоторые свойства дефектов, а именно вакансии бора (VB) и вакансии азота с антиструктурным дефектом (NBVN) в различных зарядовых состояниях. Рассчитываются методом функционала плотности (DFT) энергии образования дефектов, оцениваются вероятности переходов между ними и вычисляются необходимые для трансформации температуры отжига h-BN.

Ключевые слова: дефекты в гексагональном нитриде бора, DFT, вакансия бора, вакансия бора с антиструктурным дефектом, трансформация дефектов

Для цитирования: Yanibekov, I. I., Petrov, Yu. V. (2024) Calculation of the formation energy and transformation probabilities of some intrinsic defects in hexagonal boron nitride. *Physics of Complex Systems*, 5 (4), 215–220. https://www.doi.org/10.33910/2687-153X-2024-5-4-215-220 EDN ZDGBEQ